UC-406

LBL-27694

Lawrence Berkeley Laboratory

UNIVERSITY OF CALIFORNIA

Materials & Chemical Sciences Division

Non-Linear Optical Studies of Adsorbates: Spectroscopy and Dynamics

X. Zhu
(Ph.D. Thesis)

August 1989

For Reference

Not to be taken from this room

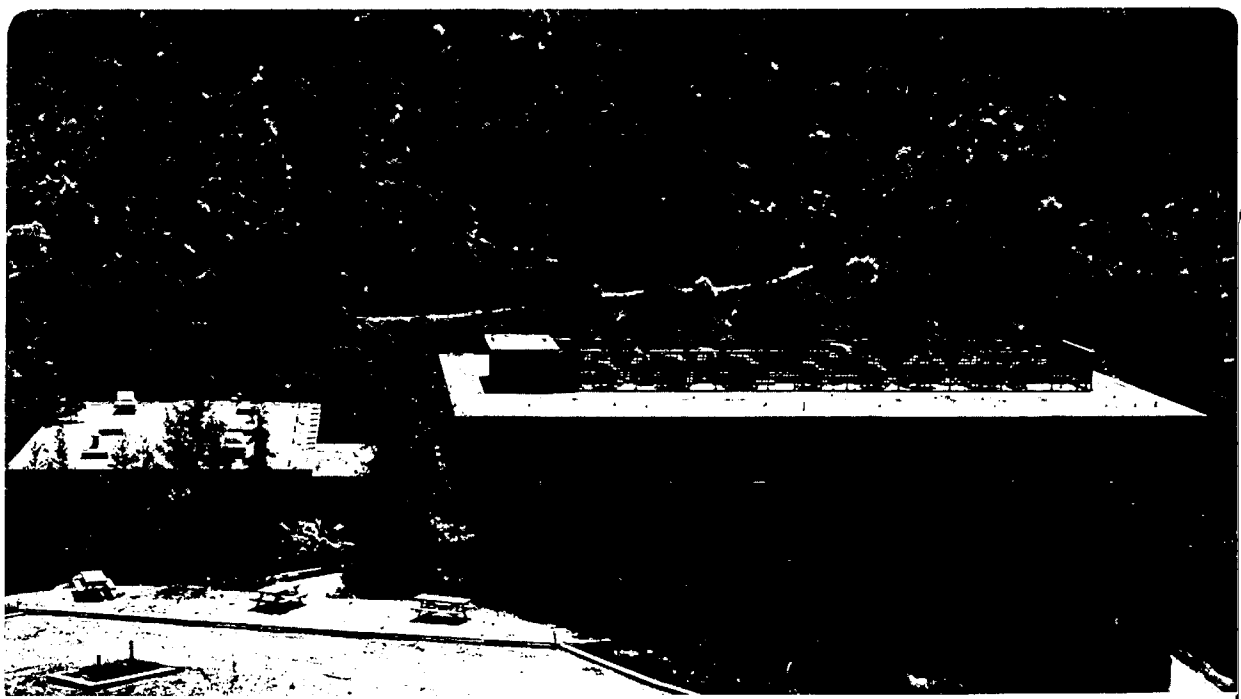

LBL-27694
Copy 1
Bldg. 50 Library.

Prepared for the U.S. Department of Energy under Contract Number DE-AC03-76SF00098.

DISCLAIMER

This document was prepared as an account of work sponsored by the United States Government. While this document is believed to contain correct information, neither the United States Government nor any agency thereof, nor the Regents of the University of California, nor any of their employees, makes any warranty, express or implied, or assumes any legal responsibility for the accuracy, completeness, or usefulness of any information, apparatus, product, or process disclosed, or represents that its use would not infringe privately owned rights. Reference herein to any specific commercial product, process, or service by its trade name, trademark, manufacturer, or otherwise, does not necessarily constitute or imply its endorsement, recommendation, or favoring by the United States Government or any agency thereof, or the Regents of the University of California. The views and opinions of authors expressed herein do not necessarily state or reflect those of the United States Government or any agency thereof or the Regents of the University of California.

LBL-27694

NON-LINEAR OPTICAL STUDIES OF ADSORBATES: SPECTROSCOPY AND DYNAMICS

by

Xiangdong Zhu

Ph.D. Thesis

Department of Physics
University of California

and

Materials and Chemical Sciences Division
Lawrence Berkeley Laboratory
1 Cyclotron Road
Berkeley, CA 94720

Nonlinear Optical Studies of Adsorbates: Dynamics and Spectroscopy

by

Xiangdong Zhu

Abstract

Because of the forbidden nature of coherent second-order nonlinear optical processes in centrosymmetric and isotropic media, optical second-harmonic generation (SHG) and sum-frequency generation (SFG) are effective probes to properties of interfaces adjoining two such media, where the inversion symmetry or isotropic order is no longer preserved. In the first part of this thesis, we have established a systematic procedure to apply the surface optical SHG technique to study surface dynamics of adsorbates. In particular, we have developed a novel technique for studies of molecular surface diffusions. In this technique, the laser-induced desorption with two interfering laser beams is used to produce a monolayer grating of adsorbates. The monolayer grating is detected with diffractions of optical SHG. By monitoring the first-order second-harmonic diffraction, we can follow the time evolution of the grating modulation from which we are able to deduce the diffusion constant of the adsorbates on the surface. We have successfully applied this technique to investigate the surface diffusion of CO on Ni(111). From the preliminary results, we have deduced the diffusion activation energy E_{diff} to be 6.9 kcal/mol and the preexponential factor D_0 to be 1.2×10^{-5} cm^2/sec. The results suggest that CO on Ni(111) is likely to move from one bridge site to another by hopping over an on-top site. The unique advantages of this novel technique will enable us to readily study anisotropy of a surface diffusion with variable grating orientation, and to investigate diffusion processes of a large dynamic range with variable grating spacings.

In the second part of this thesis work, we demonstrate that optical infrared-visible sum-frequency generation (SFG) from surfaces can used as a viable surface vibrational spectroscopic technique. We have successfully recorded the first vibrational spectrum of a monolayer of adsorbates using optical infrared-visible SFG. The qualitative and quantitative correlation of optical SFG with infrared absorption and Raman scattering spectroscopies are examined and experimentally demonstrated.

We have further investigated the possibility to use transient infrared-visible SFG to probe vibrational transients and ultrafast relaxations on surfaces.

To the memory of my father,

Lian Zhu

Acknowledgement

Almost fifteen years ago when my teen-age interest became more and more tilted towards a "career" of a "writer" to follow the footsteps of my father, he said to me in one of our last conversations that I should do well in my science classes so that my high school education would not be unwisely biased at so early a stage of my life. He passed away a few months later. Fifteen years later, I am writing this dissertation for my doctoral degree in physics. I would have been so much happier if my father and my mother could have stood by me together when I was presented with the blue-and-gold hood by Professor Buford Price, the chairman of the Department. Without the encouragement of my father and the support and love of my mother, whom I have not seen for eight years now, I would not be able to meet and acknowledge so many wonderful people who have been most helpful and special to me during my eight years at Berkeley.

I gratefully thank my thesis advisor, Professor Yuen Ron Shen. He introduced me into the field of experimental condensed matter physics seven years ago. He has given me invaluable encouragement, support, and guidance over the years. I have come to realized that he has set high professional and moral standards, which I will try to live up to throughout my career.

I would also like to give my special gratitude to Rita Jones, the group secretary. She has helped me to learn about America and its culture, and to learn to cope with the difficult times of life. I will always remember her kindness and many years of invaluable support and patient teaching.

My thanks is extended to Professor Gabor Somorjai and Professor Stephen Louie who have given me valuable professional advice.

I am always grateful to Steve Durbin, who was a senior graduate student when I first joined Professor Shen's group. He had taken much of his time to help me and his

unselfish support had made my early days in the laboratory a warm and memorable experience.

I had the most treasured opportunity to work with Harry W. K. Tom on the first second-harmonic generation experiment under ultrahigh vacuum condition. During the two eventful years, with many 36-hour days of trying to stay awake together, he had showed me so much, from laboratory skills to thinking and the level of concentration of an effective experimenter, from life in a physics laboratory in the first basement to the world outside of Birge Hall. We have established a professional and personal friendship which I will treasure for a long, long time to come. I cannot express my gratitude enough to him, as it has been built on years of hard work, many sleepless nights with loud wake-up music, tears, sweat, and laughter, not to mention those rare but long "full-course" dinners at 11 o'clock at night before going back to the laboratory again.

Later, I was most fortunate to work with Dr. Hajo Suhr from West Germany on the infrared-visible sum-frequency generation experiment. He had shared with me one of the most difficult periods of my years at Berkeley which I can never forget. We went through four half-broken CO_2 lasers in order to keep the experimental plan alive, and we succeeded at last together, with many months of hard work, mutual courage, and much joyful beer and laughter.

During the development of the second-harmonic generation technique for studies of surface molecular dynamics, I had the opportunity to work with Dr. Theo Rasing from the Netherlands. It was another most frustrating period when almost every piece of equipment for the experiment had gone wrong at least once, and the time had been extremely difficult for both of us in and out of the laboratory. I am very grateful, for the three years, he had been there, in more ways than just as a laboratory partner, we fought through all the trouble and finally accomplished what we had set out to do. His rare talent and quickness as an efficient experimental physicist and his most interesting view and taste for many fascinating aspects of life have and will continue to inspire me.

I should especially thank Jeff Hunt with whom I had shared the same laboratory, many ups and downs of life and a lasting friendship for six years. He had been very patient and kind with many of my problems, even at the time when he had enough trouble for his own to cope with.

For eight years, I have come to know so many people whom I cannot possibly name here to express my appreciation. Particularly, I gratefully acknowledge my fortunate association with Ms. Barbara Chan, Ralph Page, Marty Gifford, Hui Hsiung, Tony Heinz and members of Professor Shen's group for their professional and personal support. My appreciation also goes to C. M. Mate, Roger Carr and other colleagues with whom I had collaborated in some part of this thesis work.

I would also like to thank Department of Physics for many years of financial assistance, and thank the staff members of the department, particularly, Ken Miller, Ann Takizawa, and Ken Grove for their administrative help and technical support.

This work was supported by the Director, Office of Energy Research, Office of Basic Energy Research, Materials Sciences Division of the U. S. Department of Energy under Contract No. DE-AC03-76SF00098.

Finally, I give my heart-felt appreciation to my dear friend, Xiaowen Guo, who has been special to me for all these years.

Table of Contents

	Page
Dedication	ii
Ackowledgement	iii
I. General introduction	1
References	8
II. Surface Diffusion Studies by Second-harmonic Diffractions Off a Monolayer Grating	
A. Introduction	11
B. A overview of the current theoretical understanding of surface diffusion	17
C. Experimental procedures	28
D. Experimental set-up	29
E. Experimental results	32
1. Calibration of optical SHG as a function of CO coverage on Ni(111)	32
2. Determination of the laser-induced desorption yield vs. absorbed laser fluence	37
3. Generation of a monolayer CO grating on Ni(111) by LITD with two interfering beams	41
4. Characterization of the monolayer CO grating by optical second-harmonic diffraction	45
5. Surface diffusion of CO on Ni(111) studied by the optical second-harmonic diffraction off the monolayer CO grating	47

F. Discussion 52

1. Coverage dependence of surface diffusion kinetics 52

2. Influence of complex coverage dependence of SHG 54

3. Effect of surface defects on the experimentally determined diffusion constant 55

4. Studies of anisotropy of surface diffusion 55

5. Studies of diffusion kinetics with large dynamic range 57

6. Studies of diffusions with co-adsorbed species 58

G. Conclusion 59

H. Appendix: solutions of one dimensional Fick's equation for coverage-dependent surface diffusion 59

References 65

Figure Captions 70

Figures 73

III. Surface Vibrational Spectroscopy by Infrared-visible Sum-Frequency Generation 91

A. Introduction 91

B. Theoretical description 94

1. Molecular nonlinear susceptibility at sum-frequency 94

2. Infrared activity and Raman activity 96

3. Electronic resonance enhancement 99

4. The lineshape of SFG spectra 100

5. Intensity of sum-frequency generation 101

C. Experimental procedure 102

D. Results and data analysis 105

E. Discussion 108

F. Conclusion 115

References 117

Tables 121

Figure captions 123

Figures 124

IV. Transient Surface Vibrational Excitations and Their Detection

A. Introduction 132

B. Theoretical considerations 135

1. General description of surface vibrational excitations and surface infrared photon echoes 135

2. Surface vibrational excitations with no inhomogeneous broadening 140

3. Surface vibrational excitations with inhomogeneous broadening 142

4. Coherent infrared reemission from a monolayer of vibrationally excited adsorbates 145

C. Detection of Coherent Surface Vibrational Excitations 152

1. Direct measurement of the reemitted surface infrared photon echoes 153

2. Optical up-conversion of the reemitted surface infrared photon echoes in a nonlinear optical crystal 156

3. *In situ* up-conversion of the coherent vibrational excitations by surface visible-infrared sum-frequency generation 161

D. Conclusion 166

E. Appendix: local field corrections 167

References 173

I. General introduction

In recent years, surface science and interface science have become one of the most active research areas in condensed matter physics, material research and chemistry.[1] Atoms and molecules at surfaces form unique physical systems which are extremely interesting from both the fundamental physics point of view and the viewpoint of technology. Due to the abrupt change of the physical setting at a surface, atoms and molecules of a few layer thick near the surface normally have rather different structures and chemical bindings compared to their bulk counterparts. Partly as a result of reduced dimensionality, these overlayers can exhibit unique equilibrium thermodynamic properties and phase transitions, and in some cases strikingly different magnetic properties.[1 - 5] Since unique electronic and vibrational structures and interactions are expected in the surface region, dynamics of resonant excitations, energy exchange, relaxations of coherent phases, adsorbate mobilities and phase transitions on a surface are also expected to be interestingly different from those of bulk media.[1, 6 - 9] The physical properties of surfaces and interfaces in equilibrium and transient states play crucial roles in many important areas of technology such as crystal growth, catalytic reactions, corrosion, microelectronics fabrication and material processing.[1 - 8]

The rapid growth of surface science has been stimulated by both the needs and advances of technology. Research in this area have become increasingly controlled and sometimes quantitative with more sophisticated experimental techniques. Many surface sensitive probes have been developed.[1, 6, 9] A large number of them involve scattering or emission of low energy electrons or massive particles including ions and neutral particles. They are extremely surface specific due to the short penetration and escape depths of these particles (a few atomic layers for electrons, one atomic layer for massive particles) from

solid substrates.[1] Since atoms and electrons have short de Broglie wavelengths of a few angstroms or a few tens of angstroms and large interaction cross-sections in solids, they are sensitive probes to surface structures and morphologies, chemical bonding and surface vibrational and electronic resonances. On the other hand, the large interaction cross-sections of these massive particles with materials also limit their applications to only vacuum-solid interfaces.

Applications of lasers to surface science have also gained increasing attention over the last two decades.[6] Because of the extremely high spectral densities and highly achievable confinement in time and space of laser beams, studies of laser-induced or laser-assisted surface processes and development of highly selective surface spectroscopies in both the frequency and time domains have rightfully received enormous research attentions. Both the frequency resolutions (≤ 0.01 to 1 cm^{-1}) which are routinely required for mode identification and mode-selective studies and the time resolutions ($\leq 10^{-12}$ to 10^{-13} sec) which are required for studies of ultrafast relaxations on a surface with lasers are unmatched by any other techniques which we have mentioned earlier.[10] Another uniquely important advantage of optical probes is their capability to probe any interface accessible by light including solid-solid and solid-liquid interfaces. The relative low sensitivities of optical probes compared to those of massive particles are being improved rapidly with the recent progresses of high power laser technology and proliferation of sophisticated coherent and incoherent optical techniques. As to today, laser studies of surfaces and interfaces have become an integral and indispensable part in surface science.

Other than the monolayer sensitivity, one of the important criteria for an effective surface probe is its surface specificity. Because of the large penetration depth, an optical technique usually probes a region near a surface with a thickness of at least a few tens or hundreds of atomic layers. The optical signal from the true surface region of a few atomic layers is often accompanied by usually large contributions from the underlining bulk which can easily overwhelm the information from the surface. Elaborate and often laborious data

acquisition and analysis techniques have developed to cope with this problem, and with the help of fast computers and more stable laser sources, remarkable progresses have been made in application of both linear optical spectroscopy and Raman spectroscopy to study adsorbates on surfaces.[11] Resonance enhancement and electromagnetic enhancements have also been elegantly explored in a number of cases to increase the relative contributions from surface regions.[6, 12]

Almost a decade ago, second-order nonlinear optics was rediscovered and demonstrated as a promisingly effective probe to surfaces and interfaces.[13, 14] Unlike other optical processes, coherent second-order optical processes such as second-harmonic generation (SHG) and sum-frequency generation (SFG) are forbidden within electric-dipole approximation in isotropic media or media with inversion symmetry. In the interfacial region (of a few atomic layer thick) adjoining two such media, however, the isotropy or inversion symmetry is no longer preserved, and hence coherent second-order nonlinear optical processes are exclusively allowed from the interface region under electric-dipole approximation.[13] Consequently, second-order nonlinear optical wave generation is intrinsically surface-specific in addition to other features shared by other optical techniques. Over the last decade, optical SHG and SFG have been repeatedly demonstrated to have adequate sensitivities to adsorbates of submonolayer coverages.[14 - 16] The combination of the surface specificity and sensitivity of SHG and SFG have been explored in studies of many fundamental properties of intrinsic surfaces and adsorbates. For examples, second-harmonic generation technique has been applied to studies of surface molecular dynamic processes such as molecular and atomic adsorption, desorption and recently surface diffusion in both ambient and under ultrahigh vacuum conditions.[14, 17 - 20] Applications to investigation of surface layer structures including adsorbate orientations and structural phase transitions have also been demonstrated.[16, 21] Resonant second-harmonic generation and infrared-visible sum-frequency generation have been shown successfully to be viable electronic and vibrational spectroscopic probes to surface resonances.[12, 15, 16]

Surface optical microscopy with a resolution of the optical wavelength has also exhibited a promising potential.[22] More recently, in a series of femtosecond time-resolved pump-and-probe experiments, structural dependence of SHG were elegantly used to monitor the ultrafast disordering of electronic configurations ($\leq$ 150 fs) prior to the subsequent disordering or melting of the underlining ionic matrices through electron-phonon coupling (~ 330 fs) in the near surface region.[10]

This thesis work covering research work spanning seven years reflects some of the developments in this exciting area. The theoretical description of surface second-harmonic generation and possible mechanisms which are responsible for the large nonlinear dipole responses from surfaces of metals, semiconductors and monolayers of adsorbed molecules or even atoms have been reviewed and quite extensively discussed in numerous articles and publications.[14, 23, 24] In this thesis, We only include those theoretical backgrounds which are necessary for the presentation of this thesis work and those which were developed during the course of this work. The main ingredients of this thesis are divided into two parts. In the first part, the sensitivity of optical second-harmonic generation (SHG) are exploited in a systematic study of surface molecular dynamic processes including molecular adsorption, desorption and surface diffusion. We will focus our emphasis on the study of molecular surface diffusion with novel SHG and laser-induced desorption techniques. In the second part, infrared-visible sum-frequency generation (SFG) and difference-frequency generation (DFG) as surface vibrational spectroscopic techniques both in the frequency domain and time domain are explored and experimentally demonstrated.

In Chapter II, after a brief overview of current status of surface diffusion research, we present the experimental procedures and the results of a systematic investigation of molecular dynamics of CO on Ni(111), which eventually enable us to study the surface diffusion of the molecules on Ni(111). We first establish the general procedures to calibrate an optical SHG signal strength as a function of adsorbate coverage using for example, thermal desorption mass spectrometry (TDS) as a standard. The procedure is

applied to SHG from CO-covered Ni(111).[17] In a subsequent adsorption measurement, the calibrated SHG is used to determine the adsorption isotherm which is in turn used to determine the adsorption kinetics of CO on Ni(111).[17] We then study the molecular desorption of CO from Ni(111) by laser-induced desorption technique and conventional thermal desorption spectrometry. We use the calibrated SHG as an *in-situ* probe to monitor the local coverage change in the laser-induced desorption. On the one hand, we are able to use the results to separately determine the desorption activation energy and the preexponential factor.[18] On the other hand, by knowing the coverage change as a function of the absorbed laser fluence in the laser-induced desorption, we are able to choose the intensities of a pair of interfering laser beams with which we have successfully generated a monolayer grating of CO by laser-induced desorption.[25] The ultra-thin molecular grating is then detected and characterized by using novel diffractions of optical SHG up to fourth order. It is well-known that in studies of bulk samples with laser-induced dynamic gratings, such a periodic structure of adsorbate concentration can be used to study mass transport or surface diffusion of adsorbates.[26] At elevated temperatures, surface diffusion of CO normal to the grating troughs gradually deteriorates the modulation of the monolayer grating. By monitoring the decay of the first-order SHG diffraction signal at different sample temperatures, we have successfully investigated the surface diffusion of CO on Ni(111).[19] With the capability of monitoring diffusion in one dimension and capability of adjusting the grating orientation and the spacing, it is now possible to investigate a large variety of adsorbates and many interesting aspects of adsorbate mobilities such as anisotropy of motion and surface morphology. This may be one of the most exciting and important applications of lasers and second-order nonlinear optics to surface science.

It is well-known that vibrational spectroscopy plays an indispensable role in modern surface science.[6] Most important of all, vibrational spectra provide finger-prints of adsorbed species and other local as well as collective motions on a surface. Spectroscopic techniques enables us to selectively excite and probe vibrational resonances of specific

adsorbed species or other surface excitations. These investigations are the fundamental steps towards understanding of adlayer or overlayer properties. A number of elegant surface vibrational techniques have been developed using either massive particles or electrons or coherent as well as incoherent light.[6, 11, 27 - 30] However, most of these techniques are often limited to measurements in the frequency domain. They are hence not suitable for studies of ultrafast dynamics of vibrational transients and relaxations on surfaces. Even for the frequency domain measurements, many of these techniques are applicable only to vacuum-solid interfaces. Recently, we have developed a new vibrational spectroscopic technique using infrared-visible sum-frequency generation (SFG) and difference frequency generation (DFG) from surfaces or interfaces.[15] Besides the obvious capability to probe any interface accessible by the infrared and visible lights, SFG and DFG can be readily extended to become transient vibrational spectroscopic probes.[31] In Chapter III, we describe the principle of infrared-visible SFG from adsorbates as a surface vibrational spectroscopic technique. We then present the first successful recording of a vibrational spectrum of a monolayer of adsorbed molecules by SFG. The qualitative and quantitative correlations between the resonant SFG spectroscopy and conventional infrared absorption spectroscopy and Raman scattering spectroscopy are discussed and also experimentally confirmed. This first step has since been followed by a number of noteworthy studies of molecular orientation and preliminary investigation of vibrational energy relaxations in a monolayer Langmuir film or a Langmuir-Blodgett film using SFG by other groups.[16, 31] In Chapter IV, We explore possibility of extending SFG to study ultrafast vibrational transients on surfaces. Specifically, we will discuss some of the general considerations for generating and detecting transient surface vibrational excitations. The results indicate that we should be able to probe ultrafast vibrational transients and relaxations on surfaces by using coherent resonant excitations and detection with optical sum-frequency generation both as an optical gating technique and an up-conversion technique which can largely increase the overall detection quantum efficiency.

Together with the earlier pioneering works and some of the on-going research in this area, this thesis has in part helped to establish surface second-order nonlinear optics as unique and viable techniques for surface studies. As we can see from this thesis, by combining with other forms of laser excitation and detection methods and other complementary surface science probes, we have just started a full scale and more sophisticated investigations of many interesting surface and interface properties. We should expect much fruitful research activities with second-order nonlinear optics in the future.

References:

1. G. A. Somorjai, Chemistry in Two Dimensions: Surfaces (Cornell University Press, Ithaca, New York, 1981), p.360.
2. S. G. Mochrie, Phys. Rev. Lett. 59, 403 (1987);
   Marcel den Nijs, E. K. Riedel, E. H. Conrad, and T. Engel, Phys. Rev. Lett. 55, 1689 (1985).
3. J. W. M. Frenken and J. F. van der Veen, Phys. Rev. Lett. 54, 134 (1985);
   E. G. McRae and R. A. Malic, Phys. Rev. Lett. 58, 1437 (1987).
4. W. Daum, C. Stuhlmann, and H. Ibach, Phys. Rev. Lett. 60, 2741 (1988).
5. B. Heinrich, K. B. Urquhart, A. S. Arrott, J. F. Cochran, K. Myrtle, and S. T. Purcell, Phys. Rev. Lett. 59, 1756 (1987).
6. See, for example, *Vibrational Spectroscopy of Adsorbates*, edited by R. F. Willis, Springer Series in Chemical Physics, Vol. 15 (Springer, Berlin, 1980);
   Surface Studies with Lasers, edited by F. R. Auessenegg, A. Leitner, and M. E. Lippitsch. Springer Series in Chemical Physics, Vol. 33 (Springer, Berlin, 1983);
7. B. N. J. Persson and M. Persson, Solid State Commun. 36, 175 (1980);
   B. N. J. Persson and M. Persson, Surf. Sci. 97, 609 (1980);
   B. N. J. Persson and R. Ryberg, Phys. Rev. B 24, 6954 (1981);
   B. N. Persson and R. Ryberg, Phys. Rev. Lett. 48, 549 (1982);
   R. Ryberg, Surf. Sci. 114, 627 (1982);
   Hiromu Ueba and Shoji Ichimura, J. Phys. Soc. Japan 50, 3996 (1981);
   M. Persson, B. Hellsing, and B. I. Lundqvist, Journal of Electron Spectroscopy and Related phenomena, 29, 119 (1983);
   B. N. J. Persson and R. Ryberg, Phys. Rev. Lett. 54, 2119 (1985);
   B. N. J. Persson and R. Ryberg, Phys. Rev. B 32, 3586 (1985).
8. M. A. Morris, M. Bowker, and D.A.King, Chemical Kinetics, ed. C. H. Bamford,

Simple Processes at The Gas-Solid Interface, vol. 19, (Elsevier, 1984).

9. G. Ehlich, and Kaj Stolt, Ann. Rev. Phys. Chem. 31, 603 (1980);

10. J. Fujimoto, J. Liu, E. Ippen, and N. Bloembergen, Phys. Rev. Lett. 53, 1837 (1984);

H. W. K. Tom, G. D. Aumiller, C. H. Brito-Cruz, Phys. Rev. Lett. 60, 1438 (1988);

C. V. Shank, R. Yen, and C. Hirlimann, Phys. Rev. Lett. 51, 900 (1983).

11. Y. J. Chabal, Phys. Rev. Lett. 55, 845 (1985);

Y. J. Chabal, G. D. Higashi, and S. B. Christman, Phys. Rev. B 28, 4472 (1983);

J. E. Reutt-Robey, D. J. Doren, Y. J. Chabal, and S. B. Christman, Phys. Rev. Lett. 61, 2778 (1988);

J. P. Heritage and D. L. Allara, Chem. Phys. Lett. 74, 507 (1980).

12. T. F. Heinz, C. K. Chen, D. Ricard, and Y. R. Shen, Phys. Rev. Lett. 48, 478 (1982);

Surface Enhanced Raman Scattering, edited by R. K. Chang and T. E. Furtak (Plenum, New York, 1981);

M. Mosskovits, Rev. Mod. Phys. 57, 783 (1985).

13. Y. R. Shen, The Principle of Nonlinear Optics (J. Wiley, New York) Chapter 25, p.479-504.

14. H. W. K. Tom, C. M. Mate, X. D. Zhu, J. E. Crowell, T. F. Heinz, G. A. Somorjai, and Y. R. Shen, Phys. Rev. Lett. 52, 348 (1984);

Y. R. Shen, Ann. Rev. Mat. Sci. 16, 69 (1986);

Y. R. Shen, Nature, 337, 519 (1989);

S. G. Grubb, A. M. DeSantolo, and R. B. Hall, J. Phys. Chem. 92, 1419 (1988).

15. An initial attempt of such an experiment was reported by H. W. K. Tom, Ph. D. thesis, University of California, Berkeley, 1984 (unpublished);

X. D. Zhu, H.Suhr, and Y.R. Shen, Phys. Rev. B, *Rapid Commun.* 35, 3047 (1987).

16. J. H. Hunt, P. Guyot-Sionnest, and Y. R. Shen, Chem. Phys. Lett. 133, 189 (1987);

P. Guyot-Sionnest, J. H. Hunt, and Y. R. Shen, Phys. Rev. Lett. 59, 1597 (1987);

A. L. Harris, C. E. Chidsey, N. J. Levinos, and D. N. Loiacono, Chem. Phys. Lett. 141, 350 (1987)

17. X. D. Zhu, Y. R. Shen, and R. Carr, Surf. Sci. 163, 114 (1985).

18. X. D. Zhu, Th. Rasing, and Y. R. Shen, Chem. Phys. Lett. 155, 459 (1989).

19. X. D. Zhu, Th. Rasing, and Y. R. Shen, Phys. Rev. Lett. 61, 2883 (1988).

20. C. S. Mullin, P. Guyot-Sionnest, and Y. R. Shen, Phys. Rev. A 39, 3745 (1989).

21. Th. Rasing, Y. R. Shen, M. W. Kim, and S. Grubb, Phys. Rev. Lett. 55, 2903 (1985);

T. F. Heinz, M. M. T. Loy, and W. A. Thompson, Phys. Rev. Lett. 54, 63 (1985).

22. G. Boyd, Y. R. Shen, and T. W. Hänsch, Opt. Lett. 11, 97 (1986).

23. N. Bloembergen and P. S. Pershan, Phys. Rev. 128, 606 (1962).

24. T. F. Heinz, Ph. D. thesis, University of California, Berkeley, 1982 (unpublished).

25. X. D. Zhu and Y. R. Shen, Opt. Lett. 14, 503 (1989).

26. H. J. Eichler, P. Gunter, and D. W. Pohl, Laser-Induced Dynamic Gratings (Springer-Verlag, Berlin, Heidelberg, 1986).

27. H. Ibach and D. L. Mills, *Electron energy Loss Spectroscopy and Surface Vibrations* (Academic, New York, 1982).

28. F. Träger, H. Coufal, and T. J. Chuang, Phys. Rev. Lett. 49, 1720 (1982).

29. T. J. Chuang, J. Electron Spectrosc. Relat. Phenom. 29, 125 (1983).

30. S. Chiang, R. G. Tobin, P. L. Richards, and P. A. Thiel, Phys. Rev. Lett. 52, 648 (1984).

31. A. L. Harris and N. J. Levinos, J. Chem. Phys. 90, 3878 (1989).

II. Surface Diffusion Studies by Second-harmonic Diffractions Off a Monolayer Grating

A. Introduction

Diffusion or the lateral motion of atoms or molecules on a surface is one of the basic processes in the dynamics of gas-solid interaction.[1–4] It plays a crucial role in many technologically important processes such as catalytic reactions, crystal growths, material fabrication and processing. Fundamentally, it can be a convenient probe for us to study the lateral potential and morphology along a surface as seen by a moving particle. Furthermore, experimental studies of surface diffusion can be compared with theoretical models to yield information on the thermodynamic behaviors of these two-dimensional systems consisting of adsorbates on top of substrates.[1–21]

In the past two decades, there have been considerable progresses in both the experimental observations and the theoretical understanding of surface diffusion processes. Many elegant experimental techniques have been devised for such purpose.[5-15] As diffusion kinetics can be drastically different on different crystalline planes, most of these techniques are developed to make observations on well-defined single crystalline surfaces. They are generally categorized into two groups, one has been developed to make direct observations of single atoms and in some cases clusters on a single crystalline surface so that the microscopic feature of a surface diffusion is directly obtained; the other group has been developed to study macroscopic surface diffusion or the motions of many atoms or molecules on a surface by observing the averaged effects of these motions on macroscopic quantities such as electron emission currents, time-dependent changes of initially nonequilibrium concentration profiles of adsorbates, and surface optical or nuclear magnetic resonance spectra.

Field ion microscope (FIM) was invented to directly observe the microscopic hoppings of single atoms on single crystalline facets of a metal tip.[5] In this case, high voltages of a few thousand volts are applied between a metal tip and a viewing screen separated by a few centimeters in helium image gas. Due to the high field near the tips which is of the order of a few volts per angstrom, the helium atoms are ionized near the surface and the ions are then radially accelerated to the screen and form an image. Because the ionization rates are enhanced at the places where the overlayer atoms are, the surface morphology with atomic resolution is directly obtained on the screen with magnification of 10^6. FIM had been the only technique which allowed one to directly observe the microscopic features of atomic and even cluster diffusion on a surface before scanning tunneling microscope (STM) was invented recently.[6] However, due to the high electric field and field-induced stress near the surface which can easily alter the surface potential or even break chemical bonds between the adsorbates and the substrate atoms (field evaporation), the application of this technique has been limited mostly to strongly adsorbed metallic species or electro-negative atomic species on tips of refractory metals.

Recently developed scanning tunneling microscopes, being *in situ* probes to surface species, have also been used to observe the motions of adsorbates.[6] In a typical scanning tunneling microscopy measurement, a metal tip with as few as one atom at the end is held at a distance of a few Å from the surface, and is biased at a fraction of a volt referenced to that of the surface. The electric field (≤ 0.1 volt /Å) between the tip and the surface is large enough to cause electrons to tunnel through the potential barrier between the tip and the surface with a current in the range of nanoamperes. If the vertical distance is fixed, the tunneling current can experience an enhancement as the tip moves over a surface atom or an adsorbate due to a decrease of the local barrier width. In some cases, such an enhancement can also result from a surface species passing through the space between the tip and the surface. By monitoring the frequency at which the tunneling current spikes occur due to these "passing" events or by keeping tracking the location of the surface

species in a series of STM scans in a time sequence, it has been demonstrated that STM can be a more versatile microscopic probe for studies of the dynamics of surface motion of adsorbates. The versatility comes from the fact that the electron tunneling barriers or work functions for metals and semiconductors are substantially smaller than the ionization potentials of inert gases used in FIM for imaging, the substrate surface in a STM study needs not experience nearly as high an electric field as those in a typical FIM experiment. Hence, field evaporation, field-induced stress and bond-rapture near the surface in STM measurements are much less severe, and many surfaces can be examined by STM.

These two microscopic probes have common drawbacks. The electric fields even in STM measurements are still rather large so that they can still strongly influence the motions of the surface species near the tip where the observation is made. In addition, as it takes seconds or minutes to locate an adsorbate in a scanning mode, most molecular species would have migrated a few hundred or thousand angstroms during this time at room temperature. So far, such surface dynamics studies with STM have only been reported on atomic adsorbates or intrinsic surface atoms. These adsorbates are much strongly bonded to the surface both vertically and laterally so that their surface motions are less subject to the large electric field. In addition, they hop infrequently enough to be recorded at around room temperature.

Most of other techniques belong to the second group.[7-15] As macroscopic quantities are observed in these cases, these techniques in general perturb much less the adsorbate-substrate system and are relatively easy to be implemented. As the averaged effects of many (typically, 10^6 to 10^8) microscopic events are monitored, influences of adsorbate-adsorbate interactions, collective phenomena and thermodynamics aspects of the surface motions can be examined. At the same time, however, care must be taken to properly determine and separate contributions from events which can be microscopically completely different. Among this group, field emission microscope (FEM) is one of the viable macroscopic techniques for surface diffusion studies.[7] In arrangement, FEM is

similar to FIM in that the surface of a substrate tip is imaged onto a collection screen. In nature, it resembles STM in that the electrons in a field-induced emission from the surface of a metal tip are used monitored as the imaging gas. This requires a much milder electric field near the surface (typically, ≤ a faction of a volt / Å). The lateral resolutions are decreased to a few tens of angstroms compared to a few angstroms in FIM and STM mainly due to lateral thermal velocity spreads of the emitted electrons, which limits FEM to be a macroscopic technique. As adsorbates change the local work function, the emission current or the change of the emission current from a surface region can be used as a measure of the local adsorbate concentration. The fluctuation of the current from a well-defined region due to adsorbate motions on the surface has been successfully used to investigate the surface diffusion by a number of groups. Despite of the boundary effect and effects of the still rather large surface electric field and electron emission current on the distribution of the lateral surface potential, substantially large amount of the experimental data have been obtained with FEM. Some of the fundamental features of surface diffusion processes such as quantum tunneling for light atomic species, unusual coverage dependence of surface diffusion and the effects of many-body interactions were first revealed from FEM measurements.

More recently, in a high resolution Fourier-transform infrared reflection-absorption spectroscopy study (FTIR), Reutt-Robey et al were able to distinguish CO on different adsorption sites on Pt(111). By starting from an initially dilute but uniform distribution of CO prepared with a pulsed molecular beam source, they monitored the temporal evolution of the CO populations at terrace sites and step sites on a vicinal Pt(111).[8,9] Assuming that the hopping rates from a terrace site to a neighboring terrace site (T-T) and to a neighboring step site (T-S) are the same, they were able to determine the terrace-to-terrace diffusion constants. The technique has high time resolutions (10^{-3} s) and applicable to many molecular species as long as they have large enough infrared absorption cross sections and large chemical shifts of vibrational frequencies at different sites. A possible setback can

arise from the assumption that the T-T rate and the T-S rate are the same. This is often difficult to justify and the deduction of diffusion constants can be subject to this assumption.

Nuclear magnetic resonance (NMR) spectroscopy has also been shown to be a useful probe for investigations of molecular and atomic diffusion on surfaces of supported metal particles.[10] The thermally activated hopping rate of an adsorbate on the surface can be made large compared to the Larmer frequency of its nuclear spin in a magnetic field which is typically 10^6 to 10^7 Hz. At elevated temperatures, each nuclear spin senses different local fields during each Larmer cycle as the result of the molecular diffusion. Consequently, the averaged local field and the resultant inhomogeneous broadening have narrower distributions which is known as motional narrowing in NMR absorption spectroscopy. As the temperature dependence of the motional narrowing is closely related to the diffusion hopping rate, Wang and Shore et al have successfully used such an effect to study the diffusion of CO on the surfaces of Pt and Pd clusters. So far, due to the low sensitivities of NMR techniques, the NMR experiments have been limited only to adsorbates on metal clusters which can be packed into a high surface-to-volume ration sample at the expense of sample characterization. The technique has yet to be demonstrated for adsorbates on well-defined single crystalline planes. The scopes of the application of these techniques are in general somewhat limited by the methods of sample preparation or detection.

In the last few years, laser-induced thermal desorption (LITD) was repeatedly applied to studies of macroscopic surface diffusions.[14, 3] In this technique which is known as "hole-burning" LITD, adsorbed molecules from a small area on a surface is initially removed by LITD with a spatially confined laser pulse; at a delayed time, a second laser pulse is used to desorb the molecules which have diffused into this area from the surrounding regions during this time. The macroscopic diffusion kinetics can then be deduced from the temporal dependence of the desorption yield as a function of the delay

time. This technique has the advantage that a macroscopic concentration profile is prepared through LITD which can be applied to a large family of molecular adsorbate-substrate systems, therefore has drawn growing attentions in surface diffusion research. On the other hand, it has also been realized that the technique can be limited to probe those relatively fast diffusions as a result of the competition of simultaneous molecular thermal desorption. As molecules have to hop 10^{10} to 10^{11} times to traverse through the depleted area which is typically a few hundred microns in these experiments, the energetically less favoured thermal desorption which only take a single step can significantly affect the diffusion measurements at elevated temperatures.[14, 3] Furthermore, the measured diffusion constants are averaged over the molecular motion along different crystalline directions on the surface, important information contained in the anisotropy of diffusion constants are difficult to retrieve if not completely lost.

We have recently developed a new experimental technique in which, a monolayer adsorbate concentration grating is prepared by laser-induced desorption with two interfering laser pulses, and subsequently, optical second-harmonic diffractions are used to follow the evolution of the monolayer grating as the adsorbates diffuse across the troughs on the substrate surface.[15] This technique offers significant improvement over "hole-burning" laser-induced desorption technique. First of all, variable grating spacings from a fraction of a micron to a few hundred microns are easily obtained. Such a capability of this technique enables us to study relatively slow as well as fast diffusions without undesired effects of thermal desorption. Secondly, as only the diffusion along the direction normal to the grating trough is monitored, the anisotropy of a diffusion on a surface can be readily resolved by choosing proper grating orientations with respect to surface crystalline axes. Furthermore, the diffusion is reduced to one-dimensional, the data analysis is relatively simpler compared to a general two-dimensional analysis.

The basic principle of this new technique is as follows: a) a monolayer adsorbate grating is produced by laser-induced thermal desorption with two laser pulses interfering at

the substrate surface which is pre-covered with the molecular adsorbates; b) the subsequent diffusional motions of the remaining adsorbates perpendicular to the troughs gradually smooth out the spatial modulation of the coverage; c) optical second-harmonic diffractions are used to continuously follow the evolution of the coverage grating, and the temporal dependencies are fitted to one dimensional diffusion equation (Fick's law) to extract diffusion constants. We have applied this method to investigate the surface diffusion of CO on Ni(111) which is a typical adsorbate-substrate system consisting of diatomic molecules on a transition metal surface. Studies of such kind of systems by themselves are important for their roles in catalytic reactions. Assuming that the diffusion kinetics is weakly dependent on the coverage, we obtained the diffusion activation energy, E_{diff}, to be 6.9 ± 1.0 kcal/mol, and the preexponential factor, D_0, to be 1.2×10^{-5} cm^2/sec. The result suggests that CO is likely to move from one bridge-bonded site to the next one by hopping over an on-top site.

In this chapter, we will present the general consideration and experimental procedures of this technique. We will first briefly review some of the theoretical aspects of a surface diffusion process. We then describe our experimental procedures and present the experimental results. Finally, we discuss various aspects and extensions of this new technique for surface diffusion studies.

B. A overview of the current theoretical understanding of surface diffusion

Similar to diffusions in three dimensional bulk media, the random nature of motions of surface species arises from large fluctuating forces which substrate atoms apply to the adsorbed particles. These random forces stem from the thermal nature of the motions of the substrate atoms. On an otherwise rigid and microscopically corrugating surface, an

adsorbed particle moves along with its energy and direction of motion constantly altered under the influence of these random or thermal forces. The effect of the random forces can be characterized with a correlation time, τ_c, such that the motions of the particle which are τ_c apart bear no correlations. After an observation time t, the mean square of the distance traveled by the particle will be

$$< r^2 > = \alpha_D \left(\frac{t}{\tau_c} \right). \tag{1}$$

The proportionality constant α_D is proportional to the square of the mean distance which the particle travels over during the correlation time τ_c. Both α_D and τ_c are determined by the detailed characteristics of the static and the fluctuating forces. It is customary to define a diffusion constant as

$$D = \frac{\alpha_D}{\tau_c} , \tag{2}$$

within a factor of unity which is determined by the dimensionality of the motion. Eq. (1) is the well-known Einstein equation which Einstein derived to describe the Brownian motion of large particles suspending in solution as observed by Brown. On an atomically "flat" single crystalline surface, it has long been realized that the potential energy distribution seen by an adsorbed particle is not at all even but varies periodically along the surface with the atomic arrangement of the substrate. This concept is evidenced indirectly by the existence of activation energies for surface motions of adsorbates and directly by the images of surfaces obtained by the early field ion microscopes (FIM) and recently by scanning electron microscopes (STM). There are evidences, from the molecular dynamics calculations or stochastic trajectory simulations and the observations of thermal desorption experiments, which indicate that adsorbed particles may spend most of the time flying

between sites as a nonactivated two-dimensional gas at elevated temperatures.[21] At low enough temperature, however, those potential wells on a surface become trapping sites known as adsorption sites so that an adatom or molecule can be trapped at the bottom of one of these potential wells during most of the residence time.[4, 21] At thermal equilibrium, the adsorbed particle has a finite probability per unit time proportional to a Boltzmann factor, exp(- $\Delta E/RT$), to acquire an energy large compared to the energy barrier ΔE (in unit of kcal/mol) which separates two neighboring adsorption sites. As a result, the particle hops every once in a while to a neighboring site or even farther till it loses its energy and settles down again. By treating the problem as a unimolecular dissociation, the hopping frequency ν_d can be shown to be proportional to the Boltzmann factor with ΔE as the activation barrier,

$$\nu_d(T) = \nu_{d0}\, e^{-\frac{\Delta E}{RT}} , \tag{3}$$

here ν_{d0} is the preexponential factor of the hopping rate or often called the "trial frequency", and is determined by the densities of states before and after hopping. As the residence time between two successive jumps, which is the inverse of the hopping frequency, is normally much longer than typical times of energy relaxation and dephasing on a surface, any two successive hoppings are expected to be mostly uncorrelated. The correlation time τ_c in this case is then proportional to the inverse of ν_d. If the mean hopping length of the particle on the surface is **a**, the averaged distance traveled by the particle in any direction after a time t

$$S(t) = \sqrt{\frac{a^2\, \nu_d(T)\, t}{2}} , \tag{4}$$

and the surface diffusion constant D can be defined as

$$D = \frac{a^2 \nu_d(T)}{4} = D_0 e^{-\frac{\Delta E}{RT}} , \tag{5}$$

$$D_0 = \frac{a^2 \nu_{d0}}{4} . \tag{6}$$

This theoretical description has been widely used to analyze random hoppings of single atom or molecule on a surface at low coverage limit in which case the interactions between adsorbates are negligible and the diffusion kinetics are mostly determined by the interaction between the adsorbate and the substrate.

On the macroscopic level, such random hoppings of many adsorbed particles lead to fluctuations of local adsorbate concentrations in a small region on a surface even under equilibrium conditions.[7] If the initial adsorbate distribution is not at equilibrium, the random motions of these particles result in macroscopic mass transports which tend to smooth out the inhomogeneity of the distribution. Such a mass transport process is described by Fick's law and mass conservation law,

$$\mathbf{q} = -D^* \nabla\theta , \tag{7}$$

$$\nabla \cdot \mathbf{q} + \frac{\partial\theta}{\partial t} = 0 . \tag{8}$$

where $\mathbf{q}$ is the mass current across unit length (two-dimensional) perpendicular to $\mathbf{q}$; θ is the surface concentration of the particles; the proportionality constant D^* is often called the macroscopic or chemical diffusion constant which includes the effects of interactions among the diffusing particles. It is easily shown that in the limit of zero coverage, $\theta \rightarrow 0$, the chemical diffusion constant (D^*) equals to the uninhibited diffusion constant (D) for a single particle on an otherwise empty surface. Consider two adjoining rows on a surface with a square lattice. Their widths are taken to be the lattice constant which is assumed equal to the average hopping length **a**. They each have local equilibrium densities of θ_1 and

θ_2. In the limit of zero coverage, hoppings of any particle in these two strips can be considered completely uninhibited. The number of particles which move across unit length per unit time from the first row to the second is equal to the product of the single particle hopping rate in that direction $\nu_d(T)/4$ and the number of particles θ_1 **a**,

$$J_{1\to 2} = \frac{\nu_d(T)}{4} \mathbf{a}\, \theta_1 \; ; \tag{9}$$

similarly, from the second to the first,

$$J_{2\to 1} = \frac{\nu_d(T)}{4} \mathbf{a}\, \theta_2 \; . \tag{10}$$

The net current density pointing from the first row to the second row is defined as **q**, which is equal to

$$\mathbf{q} = J_{1\to 2} - J_{2\to 1} = -\frac{\nu_d(T)\, \mathbf{a}^2}{4} \frac{\theta_2 - \theta_1}{\mathbf{a}} = -D\, \nabla\theta \; . \tag{11}$$

In this case, $D = \nu_d(T)\mathbf{a}^2/4$ as in Eq. (5).

As the coverage increases, interactions among diffusing particles themselves can affect the macroscopic diffusion process in a number of ways which may lead to a complex coverage dependence of the chemical diffusion constant. In the limit of short-range interactions such that they do not alter the surface potential but only prohibit two surface species to occupy the same sites, the presence of many diffusing particles on the surface only reduces the probability for a particle to find unoccupied sites. The latter is proportional to $(1 - \theta/\theta_s)$ with θ_s equal to the saturation concentration. In these cases, the forward current from the first row to the second is now reduced and proportional to $\theta_1(1 -$

θ_2/θ_s), and the backward current from the second row to the first is proportional to $\theta_2(1 - \theta_1/\theta_s)$. One then finds that the net mass current density is still proportional to the difference of θ_1 and θ_2 and the difference is not affected by the blocking of sites. This indicates that in the limit of short-range interactions, the chemical diffusion constant is not dependent on coverage even at high coverages and is equal to the microscopic diffusion constant given by Eq. (5). This has been confirmed by Bowker et al in a Monte Carlo simulation study.[16]

In the cases of long-range interaction (nearest neighbor interaction, next-nearest neighbor interaction, etc.), the diffusion energy barriers can be altered by the presence of neighboring particles in addition to site-blocking, and hence the hopping rate of a particle may be critically subject to the occupations of neighboring sites of the initial and the final sites before the jump. As long as the interaction energies are small or comparable to the thermal energy kT, they will only weakly change the thermally activated hopping rate, we should expect a weak coverage-dependence of the chemical diffusion constant D^* which should only be mildly different from D. For interaction energies (in unit of kcal/mol) large compared to RT (R = k × Avagadro's constant), the diffusion barriers and the resultant Boltzmann factors in hopping rates change drastically with the increase of occupations of neighboring sites and can result in large variation of the macroscopic diffusion constant with coverage. Such strong, long-range interactions can also be mediated through the substrates which may even undergo structure phase transitions in the presence of large number of adsorbates and drastically change the surface potential seen by the adsorbates. Although it is difficult and for most cases impossible to find a tractable form for the macroscopic diffusion constant in general, we can use some physical arguments to at least obtain the trend of its change as the coverage increases. Consider adsorbates on a square lattice for an example. Assume that long-range interactions only affect the nearest neighboring particles, and for convenience, they are also assumed to be repulsive. Furthermore, we assume that the activation energy barrier is increased from that

of the bare surface by the product of the nearest neighbor interaction energy, ε, times the number of the nearest neighbors and ε is large compared to RT. With $\exp(\varepsilon/RT)\theta \geq 1$, we expect those hopping events initiated with all three neighboring sites occupied to dominate. The forward and backward current densities are then proportional to the probabilities to find all three neighboring sites around the particle occupied except the one it is about to hop into, $(\theta_1)^3(1 - \theta_2/\theta_s)$ and $(\theta_2)^3(1 - \theta_1/\theta_s)$, respectively. As a result, the net current density and the diffusion constant D^* are first expected to increase with the coverage as θ^3, and towards the saturation coverage, they drop as $(1 - \theta/\theta_s)$. Therefore generally speaking, the nearest-neighbor repulsive interactions between adsorbates lead to an chemical diffusion constant D^* to increase from D by a factor as large as $\exp(3\varepsilon/RT)$ and then slope down toward the saturation coverage. If one has to include the next nearest neighbor or use more general forms of adsorbate interaction instead of the simple pair-potential parameter ε, coverage dependence of surface diffusion dynamics are expected to be more complex. In addition, the mean hopping lengths for individual particles may also vary as the surface potential distribution and the fluctuating force change with coverage. Collective motions at high coverages can further increase the mean jump length if we insist on single-particle hopping picture. These effects all contribute to the apparent coverage dependence of diffusion constants D^*. In these general cases, Fick's law as given by Eq. (7) remains valid, but the proportionality constant D^* may be very different from that for the uninhibited motion of single particle on an open surface.

There are numerous review articles in which various aspects and current status of surface diffusion theories are discussed.[1-4] The challenging and difficult task for theorists in this area is to quantitatively or even qualitatively predict the diffusion constant of a given adsorbate on a surface and its change with adsorbate coverage. As the experimental data are still rather scarce for comparison while the volumes of theoretical calculations of even semi-quantitative or qualitative nature are formidably large as we will discuss shortly, currently existing theoretical calculations involve various types of bold simplifications,

mostly by using simple tractable pairwise potentials such as the Lennard-Jones potential or Morse potential whose parameters are determined sometimes by somewhat arbitrary choices of material constants and data from other related surface measurements. In general, the assumptions in these oversimplifications are difficult to justify and the results in most cases are not expected to be quantitatively or even qualitatively correct given the sensitivity of molecular motions to the details of interactions on the surface. However, these calculations do provide valuable physical pictures which help one to understand surface diffusion as it occurs and possible mechanisms which may be responsible for the observed experimental results. They also can help to establish the courses along which the experimental efforts should be directed. As a surface diffusion can be viewed as a special case of unimolecular reactions, theories of rate process or transition-state theories are widely used to estimate or even calculate the preexponential factor ν_{d0}.[4, 16, 17] From the rates of energy relaxation on surfaces which are estimated to be a few kT per 10^{-12} sec from molecular beam scattering measurements, the mean hopping distances for each jump are also expected to be a few Å which are of the order of surface lattice spacings. As to the determination of diffusion activation barriers or more generally, the lateral potential energy seen by an adsorbate, first-principle or *ab initio* calculations have only been performed on a handful of ad-atoms at high symmetry points on the surfaces of a few materials. This is mainly due to the complexities of many-body interactions involving many electrons and atoms in solids. Only recently theorists could carry out first-principle calculations or empirical pseudo-potential calculations of the ground-state bulk properties of a number of materials within local-density approximations (LDA). They often require formidable computation even with the most advanced computers.

In order to calculate surface properties, larger number of independent atoms and degrees of freedoms in a unit cell have to be included in the calculation. This adds to the already enormous complexity of the calculations and therefore further limits the progress and application of *ab initio* theoretical calculations. For example, the potential energies of

atomic species such as Si, Ge, S and H at high symmetry points on the surfaces of single crystalline silicon have been reported based on total energy calculations. These results are not easily generalized to other systems. However, there exist a number of theoretical approaches which can give approximate solutions to surface potential calculations. To avoid the complexity of *ab initio* many-body calculations and at the same time try to include the main ingredients of interactions on a surface, these methods start with simple and tractable pairwise-additive potentials whose parameters are determined mostly from known properties of the adsorbate-substrate systems. Lennard-Jones (12-6) potentials of $V(r) = 4U_0[(\sigma/r)^{12} - (\sigma/r)^6]$ and Morse potentials of $V(r) = U_0\{\exp[-2\alpha(r - r_0)] - 2\exp[\alpha(r - r_0)]\}$ are most frequently used forms for analytical calculations of surface potential distributions. The parameters are usually determined by bulk thermodynamic constants such as lattice constants, cohesive or sublimation energies and compressibilities for self-diffusion calculations and by adsorption bond-length, heat of desorption and adatom-surface vibrational frequencies for hetero-diffusion calculations. Once these parameters are determined, one can either map out the potential energy distribution by minimizing the empirical potential energy with respect to the vertical distance of the adsorbate above the surface and obtain the activation energy barrier, or perform molecular dynamics calculation to determine both the preexponential factor and activation energy barrier. The latter is more accurate as it more realistically includes the statistical average of the motions and fluctuations or dynamical aspects of the adatom-substrate interactions and even the dynamic relaxations of the substrate in response to the adatoms.

In typical molecular dynamics (MD) calculations, the classical trajectories of the adatoms and substrate atoms are directly evaluated from generalized Langevin equations which include the forces of the empirically determined pairwise potentials, frictions and the random white noise which provide the energy exchange between adatom and the substrate atoms and maintain the equilibrium temperature. Classical trajectories are adequate descriptions for most of adsorbates except for light atoms such as H or D which are

expected to exhibit quantum mechanical effects. Initially, the adatom and a small number of substrate atoms of two to three layers are placed at the adsorption site and equilibrium lattice points, respectively, with the substrate atoms in contact with the rest of the rigid substrate lattice. The trajectories of these selected atoms are then calculated at a time step typically of one-hundred of the classical vibrational periods (10^{-12} sec) which are determined by $(m\sigma^2/U_0)^{1/2}$ for Lennard-Jones potentials or $(m/\alpha^2U_0)^{1/2}$ for Morse potentials. The amplitudes of the random force and the friction coefficient are adjusted to give the desired sample temperatures. Usually as few as 500 to 1000 time steps are needed for complete thermalization. Afterward, the sample temperature can be monitored by evaluating the averaged velocities and the kinetic energies of the atoms involved after each step. For diffusion calculations, additional 50000 to 500000 time steps depending on the sample temperature are integrated to obtain one trajectory r(t). The diffusion constant D can be obtained using Eq. (1) and (2) by averaging $[\ r(t)\ ]^2$ over many runs as we just described. As we can see, these MD calculations are formidable even with simple empirical pairwise potentials. They have been mostly used to obtain diffusion constants for single adatom or a few adatoms on open surfaces at zero coverage. As the trajectories of the adatom and the substrate atoms are directly followed, many informative features of surface diffusions, such as adatom-substrate atom exchanges, correlation of successive hoppings, concerted motions of adatom-clusters and transitions from site-to-site hoppings to motions resembling a two-dimensional gas can be and have been investigated.[21] In some cases such as self-diffusion of W on W(110), the molecular dynamics calculations have yielded the diffusion constants which are in surprisingly good agreement with the experimental observation.[21]

For the effects of adsorbate-adsorbate interactions or the coverage dependence, most of the theoretical investigations have resorted to further simplifying the interactions among the adsorbates by progressively introducing additive energy correction terms which model the nearest neighbor, next nearest neighbor and even three-body interactions. It is

usually assumed that these energy corrections δE depend on the occupations of neighboring sites before and after the hopping and affect the Boltzmann factor for the microscopic hopping probability. By properly carrying out the thermodynamic average of these probabilities for given coverages, coverage-dependence of diffusion constants can be obtained. If one only considers two-body interaction terms, it is possible to obtain analytical expressions of diffusion constants as functions of coverage which are physically tractable.

Monte Carlo numerical simulations have also been used as alternative means of equilibrium thermodynamic average. These simulations are more straightforward and readily applicable even to cases involving three-body or even higher order many-body interaction terms.[20] The values for activation energy corrections are either determined by reproducing adsorbate overlayer structures at isolated coverages or treated as adjustable for qualitative analysis. In these simulation studies, small surface areas which hold a few hundred sites are initially covered with adsorbates of desired coverages. To reach thermal equilibrium, each adsorbate is allowed 10^2 to 10^3 times to randomly hop to neighboring sites with a probability equal to unity if the final state energy ε_f is smaller than that of the initial state ε_i, or equal to $\exp[-(\varepsilon_f - \varepsilon_i)/RT]$ if $\varepsilon_f > \varepsilon_i$. Afterward, each adsorbate is allowed to hop randomly in direction to an unoccupied nearest neighboring site with a rate proportional to $\exp(-\delta E/RT)$ where δE is the change of the activation energy from that at zero-coverage, ΔE_0, due to the presence of neighboring adsorbates around the adsorbate before jump. Usually, the time step Δt in the calculation is chosen as $\tau_0 \exp(-\delta E_{max}/RT)$ where $\tau_0 = \exp(\Delta E_0/RT)/\nu_{d0}$ and δE_{max} is the maximum of the energy change in all possible configurations. For attractive interactions, δE_{max} is equal to zero. For ΔE_{max} equal to 2 kcal/mol, Δt is expected to be $0.03\ \tau_0$. On average, it often takes large number of time steps to see appreciable displacement r(t) for the adsorbates. These displacements can then be analyzed using Eq. (1) and (2) to yield diffusion constants relative to that of zero-coverage value, $D(\theta) / D(0)$. This method has been used to qualitatively examine the

possible mechanisms which are responsible for the complex coverage dependence of diffusion of oxygen atoms on W(110) observed by Chen and Gomer.[7] The oversimplification of adsorbate-adsorbate interactions in the Monte Carlo simulations makes it difficult to yield quantitative results that can be directly compared with experiments.

In summary, interesting informations are contained in the dependence of a diffusion constant D on parameters such as coverage, temperature, surface morphology and the specific substrate. Theoretical calculations which could grossly predict the surface potential distribution and diffusion behaviors for a given adsorbate-substrate system are not generally available partly due to the lack of theoretical understandings of intrinsic surfaces for most materials and partly due to the complexity of these calculations. The kinematic as well as energetic aspects and collective motions make theoretical treatment even more difficult and expensive to handle. However, the existing theories have already provided many interesting physical pictures and in some cases quantitative descriptions of surface diffusions that can be compared with experimental data. They have also indicated possible directions along which the experimental efforts should be steered in the future. With increasingly available experimental data and improved theoretical models or approximations, one should expect to gain better and more comprehensive understanding of adsorbates on surfaces and various aspects of gas-solid interaction, and their roles in many surface dynamic processes.

C. Experimental procedures

In our experiment, optical second-harmonic diffractions off monolayer concentration gratings are used to study surface diffusions. To apply this technique, we

first need to determine the coverage dependence of optical SHG in order to analyze the SHG measurements. Secondly, in order to generate monolayer gratings through laser-induced desorption, we need to establish the experimental conditions which can give rise to desired grating structures or modulations. Therefore the experiment consists of five steps: 1) The first step is to determine the dependence of optical SHG on CO coverage on Ni(111) through a calibration against a thermal desorption mass spectrometry (TDS) measurement. This enables us to determine the strength and therefore detectability of second-harmonic diffractions; 2) the second step is to determine the dependence of the laser-induced desorption yield or the coverage change on the absorbed laser fluence (joules/cm^2) in a single pulse. This enables us to determine the energies of the two interfering laser beams in the next step to produce the desired monolayer grating; 3) we then generate a monolayer grating by desorption using two laser pulses whose energies are so chosen that the resultant grating profile has an optimum modulation; 4) the fourth step is to characterize the grating with optical second-harmonic diffractions; 5) we follow the evolution of the monolayer grating by monitoring the first-order second-harmonic diffraction signal at different sample temperatures as adsorbed molecules diffuse on the surface. The results enable us to deduce diffusion kinetics parameters by fitting to the one dimensional diffusion equation, or Fick's law.

D. Experimental set-up

The experiment was performed with the sample under ultrahigh vacuum (UHV) condition. The operating pressure was maintained at 0.8×10^{-10} torr. A 99.998% pure Ni(111) sample disc of 1 cm in diameter and 1.5 mm thick was oriented and cut to within 0.5° of (111). After mechanical polishing with 0.05 μm Al_2O_3 powder, it was annealed in

a hydrogen atmosphere at 1000K for a week to remove the bulk sulfur content before it was vertically mounted inside the UHV chamber. One of its (110) axes was oriented at an angle of 30° off the horizontal plane. The sample was cleaned by sputtering in 5×10^{-5} torr argon at a 500 volt beam voltage for 2 hours, followed by annealing during slow cooling down to room temperature. The cleaned Ni(111) surface showed little traces of C and O and less than 0.5% of a monolayer of S as examined with Auger electron spectroscopy (AES). Sharp and clean (1×1) low energy electron diffraction patterns (LEED) of Ni(111) indicated a well-ordered surface layer. A Chromel-Alumel thermal couple was welded to the edge of the sample to monitor the sample temperature. An electron beam heating assembly and liquid nitrogen cold finger were used to vary the sample temperature from 130K to 1400K within ± 0.2K. A UTI quadruple mass spectrometer was used to monitor the mass yields in the conventional thermal desorption mass spectrometry (TDS) measurement. The mass spectrometer was also used to detect the mass yields in the laser-induced desorption yield measurement as an independent, qualitative monitor of the desorption. CO was introduced into the chamber through a leak valve, and the dosage was determined by the partial pressure change which was monitored by B-A type ion gauge. The absolute surface coverage was determined from ordered C(4×2) LEED pattern at the coverage $\theta_s = 0.5$ and the flash thermal desorption spectrometry measurement.

For the optical excitation and detection, we used the output of a single-mode Q-switched Nd:YAG laser operating at 1.064 μm which has a Gaussian temporal profile with a pulsewidth (FWHM) of 16 ns and a nearly Gaussian spatial profile. The laser desorption experiment was performed directly with the 1.064 μm pulses with the polarization of the electric field in the plane of incidence. To probe the coverage of CO on Ni(111) with optical second-harmonic generation, we used the laser pulses at both 1.064 μm and 0.532 μm which was obtained by frequency-doubling the same 1.064 μm beam. The polarizations of the probe beams were also chosen in the plane of incidence to optimize the

overall SHG signal. Two different excitation and probe geometries were used. In Fig. 1(a), we show the optical set-up for the laser-induced desorption (LID) yield measurement. Both the desorption beam and the probe beam were brought onto the sample collinearly at 45° from the surface normal. The 45° incident angle was chosen to compromise the following two experimental considerations: a) the SHG from a metal surface is more effectively generated with parallel-polarized pump beams incident at more oblique incident angles; b) to ensure a uniform desorption over an probed area of one millimeter in diameter at the center of the sample, the desorption laser beam diameter is chosen to be 5.0 to 7.6 mm. It is then desirable to have the incident angle close to surface normal to contain the laser beam on the sample so that only the mass yield from the sample surface is monitored as an independent desorption indicator. In Fig. 1(b), we show the optical arrangement for the grating generation and surface diffusion measurement. In this case, the two desorption beams at 1.064 μm for creating an interference pattern at the surface were incident at ± 1.5° from the surface normal, respectively. The probe beam at 0.532 μm was brought to the sample at 71.4° to optimize the efficiency of second-harmonic diffractions. The SHG signals with parallel polarization were detected with a gated photon-counting system. The overall quantum efficiency of the detection was close to 2%. The adsorption and desorption of CO on the irradiated sample remained unaffected after the irradiation of one desorption pulse as checked by *in-situ* SHG and LID mass yield measurements. These served as indications of devoid of surface damage.

E. Experimental results

1. *Calibration of optical SHG as a function of CO coverage on Ni(111)*

In recent years, optical SHG has been developed into a versatile probe to surfaces and interfaces.[22] This stems mainly from the fact that in the electric dipole approximation, coherent radiation at second-harmonic frequency in a centrosymmetric or an isotropic medium is forbidden, but necessarily allowed in the surface region of a few atomic or molecular layer thick where the prevailing centrosymmetry is no longer preserved.[22] The intrinsic surface specificity and sensitivity of SHG to atomic structures and electronic configurations at surfaces have been recognized and applied to studies of a variety of surface and interface properties. It has been demonstrated that strong dependence of surface SHG on adsorbate coverages can be used to study atomic and molecular adsorption processes.[22, 23] Such a dependence is used in our experiment to study the evolution of the coverage profile due to molecular surface diffusions.

In general, adsorption of atoms or molecules changes the electronic configuration at the surface and therefore the optical susceptibilities. In the presence of a monochromatic optical field at ω, the effective surface nonlinear susceptibility at second-harmonic frequency 2ω, for a given adsorbate coverage θ, can always be written as [22]

$$\chi(2\omega) = A + B(\theta), \tag{10}$$

where $B(\theta)$ is a function of θ which vanishes at $\theta = 0$. $B(\theta)$ can be a complex function of θ. For most of materials including nickel, quantitative theoretical calculations of the optical nonlinear susceptibilities which involve properties of the excited states as well as the ground states of the surface and the bulk are not available. For the purpose of application in our case, $\chi(2\omega)$ vs θ must be determined experimentally. It is possible that adsorbates only locally affect the surface optical nonlinearity. $\chi(2\omega)$ can then be separated into

contributions from the unaffected surface, $A'(1-\theta)$, the affected surface, $B'\theta$, and the bulk, C', due to higher order multipolar responses such as electric quadruple contribution,

$$\chi(2\omega) = A'(1-\theta) + B'\theta + C' = A + B\theta , \tag{11}$$

which is linearly dependent on coverage. In this case, in order to determine the coverage dependence of $\chi(2\omega)$, one only has to determine the magnitudes of A, B and their relative phase.

To determine $\chi(2\omega)$ as a function of adsorbate coverage θ under ultrahigh vacuum condition, we have chosen to use standard thermal desorption mass spectrometry as the calibration.[24] Assume that the SHG signal has one-to-one correspondence to θ. For a given coverage θ and a fixed sample temperature T, one can measure a SHG signal. The absolute coverage θ relative to the saturation coverage θ_s can be determined by a subsequent flash desorption ,

$$\frac{\theta}{\theta_s} = \frac{\int_{-\infty}^{+\infty} \Delta p(\theta)\, dt}{\int_{-\infty}^{+\infty} \Delta p(\theta_s)\, dt} , \tag{12}$$

where $\Delta p(\theta)$ is the partial pressure rise during the thermal desorption, which is proportional to the rate of desorption, $d\theta/dt$. θ_s is the saturation coverage. By varying the initial θ, one can obtain an empirical function, SHG = constant $\times\, |\chi(2\omega)|^2 = f(\theta,T)$. One may have to measure the phase of the second-harmonic susceptibility $\chi(2\omega)$ in order to completely determine A and $B(\theta)$ in Eq. (10). Such a general calibration procedure involves a set of SHG and TDS measurements, which is similar to the procedures normally used to calibrate other coverage probes such as work functions with TDS.

There are special cases in which this general procedure can be simplified. For example, if both the SHG signal and the adsorption sites are independent on the sample temperature in the temperature range of adsorption and desorption, we can monitor the SHG signal and the partial pressure rise simultaneously in a single flash desorption starting from the saturation coverage θ_S. At a given sample temperature T(t) or time t(T) during the temperature-programmed thermal desorption, the SHG signal, SHG(t), corresponds to a surface coverage θ which is determined by an integration of the partial pressure rise to t,

$$\frac{\theta}{\theta_s} = \frac{\int_{-\infty}^{t(T)} \Delta p(\theta_s)\, dt}{\int_{-\infty}^{+\infty} \Delta p(\theta_s)\, dt} . \tag{13}$$

In this way, a continuous calibration curve between the SHG signal and the coverage can be obtained.

Other important cases which may be frequently encountered relies on the condition that the nonlinear susceptibility is linearly dependent on adsorbate coverage, $\chi(2\omega) = A + B\theta$. In these cases, only three parameters are to be determined, the magnitudes of both A and B, and their relative phase. One can use SHG to follow an adsorption isotherm (coverage θ as a function of exposure L) from which we should be able to determine these three parameters as well as the adsorption kinetic parameters.[22]

If the adsorption isotherm $\theta(L)$ is known, SHG vs θ can also be conveniently determined by monitoring SHG as a function of the exposure L in an adsorption measurement.

For Ni(111), the SHG signal is found unchanged in the temperature range from 140K up to 700K over which the adsorption and the conventional thermal desorption are performed; furthermore, it has been established in the literature that CO adsorbs only on the

bridge-bonded sites for $\theta < \theta_s = 0.5$.[25, 26] The SHG signal is expected to depend only on the CO coverage. Therefore, we choose to use a single flash TDS to calibrate the SHG.

The set-up is shown in Fig. 1(a). The probe beam wavelength is at 1.064 μm. The cleaned Ni(111) is initially dosed with CO to the saturation coverage $\theta_s = 0.5$ at 273K. The absolute coverage is confirmed by the appearance of good C(4 × 2) LEED pattern at this coverage.[25] The CO-covered Ni(111) is subsequently heated up at a rate of 2K/sec, we simultaneously monitor both the pressure rise and the SHG signal from the surface with time. The results are shown in Fig. 2. The CO coverage at a given temperature T is obtained by integration of the pressure rise up to T on panel (a) in Fig. 2 using Eq.(13). The SHG signal versus CO coverage can then be plotted as shown in Fig. 3(a). The large change of SHG with coverage demonstrates again the dominance of the surface contribution to the overall SHG signal from this type of metal surfaces. The curve in Fig. 3(a) can be used as a calibration curve to probe CO coverage on Ni(111) in other circumstances. We can actually fit the experimental result in Fig. 3(a) quantitatively by using Eq. (11). This model is stimulated by the fact that on a metal surface such as nickel, there is usually a large electron density gradient which is presumably responsible for the large surface optical nonlinearity. If we assume that adsorption of electro-negative molecules such as CO on Ni(111) alters the density of surface electrons and in turn the effective density of induced surface nonlinear optical dipoles, we expect the surface susceptibility $\chi(2\omega)$ to be linearly dependent on coverage. Using A and B as adjustable parameters, we obtain a theoretical fit as shown in solid curve in Fig. 3(a). From the fit, we find

$$\frac{B}{A} = 0.9\, e^{i\,165^\circ} \; .$$

The calibrated SHG can be used to determine the adsorption isotherm of CO on Ni(111) in Fig. 3(c) from the measurement of SHG versus the CO exposure L (in unit of Langmuir, 1 Langmuir = 10^{-6} torr × second) shown in Fig. 3(b). We find that the measured adsorption isotherm can be well fitted with the relation

$$\theta(L) = \theta_0 \{ 1 - \exp [- (s_0 \Gamma L) / (N_s p \theta_s)] \}, \tag{14}$$

indicating that the adsorption obeys a simple Langmuir kinetics. Here s_0 is the initial sticking probability; Γ is the incoming flux of molecules; N_s is the surface density of the substrate atom; p is the CO partial pressure. In the fitting, s_0 is chosen as an adjustable parameter, and we obtain $s_0 = 0.8$, very close to unity.

As a double check, we also measured SHG versus the CO exposure L with the pump laser at 0.532 μm, as shown in Fig. 4(a). It is known that surface SHG should depend on laser frequency. However, the simple Langmuir kinetics for adsorption of CO on Ni(111) and the linear dependence of $\chi(2\omega)$ on θ still hold. We therefore expect that the experimental result of SHG versus exposure L at 0.532 μm can again be fitted using Eqs. (11) and (14) with A and B as adjustable parameters. This is seen in Fig. 4(b), and we find

$$\frac{B}{A} = -0.6 . \tag{15}$$

$$\text{SHG} = \text{constant} \times (1 - 0.6\theta)^2 \tag{16}$$

The SHG signal strength with the excitation wavelength at 0.532 μm is found over 4 to 6 times as strong as that excited with 1.064 μm beam for the same input power density. This is mainly due to relatively small Fresnel coefficients or relatively large electromagnetic screening (larger dielectric constants) for SHG excitation and radiation at 1.064 μm. In

the later laser-induced desorption measurement, we use SHG from the 0.532 μm excitation to probe the coverage change.

We have also calibrated the SHG signal as a function of coverage with the 0.532 μm pump beam incident at 71.4° as shown in Fig. 1(b). This geometry further increases the overall SHG radiation efficiency by another factor of 2. This geometry is used later to detect weak SHG diffractions from monolayer gratings. The measurement is necessary for a quantitative characterization of monolayer gratings of CO and the surface diffusion measurement. With this geometry, we obtain SHG versus CO coverage shown in Fig.4(c). The result is fitted well using Eqs. (11) and (14) with

$$\frac{B}{A} = -\ 0.68, \tag{17}$$

$$\text{SHG} = \text{constant} \times (\ 1 - 0.68\theta\ )^2. \tag{18}$$

Eq. (18) will be used in the analysis of the second-harmonic diffractions. As we will see, the magnitude of the coefficient for the coverage dependent term, B, determines the absolute signal strengths of the SHG diffractions in the later measurements.

2. *Determination of the laser-induced desorption yield vs. absorbed laser fluence*

In order to control the generation of a molecular concentration grating of CO on Ni(111) by laser-induced desorption (LID) with two interfering beams, we need to know the CO coverage change $\Delta\theta$ ($= \theta_s - \theta$) as a function of the absorbed laser fluence, $\int I dt$, which could be measured experimentally. From this relation, we can then determine the ranges of the intensity modulation that can give rise to desired grating profiles. Experimentally, we have chosen the calibrated SHG over mass spectrometry as the in-situ probe to monitor the coverage change induced by LID. Mass yield measurements with

quadruple mass spectrometers are often used as the standard methods in conventional thermal desorption experiments and have also been applied to laser-induced desorption.[27,28] In the latter case however, the intensity variation across the laser beam results in the variation of the surface temperature rise across the irradiated area. Hence the desorption yield as a function of the absorbed laser fluence from a normal mass yield measurement requires difficult deconvolution and can lead to large experimental uncertainty.[28] With SHG, we can probe just the center of the depleted region where the absorbed laser fluence is uniform and easily determined experimentally.

The experimental set-up is shown in Fig. 1(a) or Fig. 5. The sample is held at 273 K. Before laser desorption measurement, it is dosed with CO to a saturation coverage, $\theta_s = 0.5$. We use the probe beam at 0.532 μm to monitor the coverage change. The probe and the desorption beams are centered with each other and collinearly incident on the sample. The size of the probe beam is reduced to a cross-section 30 times smaller than that of the desorption beam. In this way, we only probe the central area where desorption is uniform within a few percent. The laser fluence for desorption at the center of the desorption beam is measured within ± 4%. We measure SHG versus laser fluence. Using the curve in Fig. 4(b), we deduce the remaining CO coverage after the laser desorption. In Fig. 5, we plot the measured coverage change (open circles) as a function of the absorbed laser fluence. The coverage varies substantially from less than 10% to over 90% in the fluence range from 0.16 to 0.36 J/cm^2. From this result, we can already determine the range of the laser intensity modulation which will yield desired coverage modulations without knowing details of desorption mechanism.

Quantitatively, if we assume that the laser-induced desorption is due to the rapid heating-up of the substrate by the laser pulse, we can use the theory of thermal desorption to analyze our experimental result.[28] Such an analysis can actually help to determine the thermal desorption energy and the preexponential factor separately. It is known that in a metal such as nickel, the absorbed light energy through electronic excitations is thermalized

within a few picoseconds or a fraction of a picosecond via ultrafast electron-electron and electron-phonon couplings.[29] For a nanosecond laser heating process, instantaneous local equilibrium is then expected. The thermal energy heats up a surface layer of a thickness of the thermal diffusion length, $\xi \sim (\kappa\, \tau_p)^{1/2}$, κ is the thermal diffusivity of nickel. Knowing the characteristics of the laser pulse and the optical constants and thermal constants of single crystalline nickel,[30] the surface temperature rise as a function of time and laser fluence can be calculated using the classical heat conservation equation and Fourier's law

$$\nabla \cdot \mathbf{J}(\mathbf{r},t) + \rho C_p[\partial T(\mathbf{r},t)/\partial t] = A(\mathbf{r},t), \tag{19}$$

$$\mathbf{J}(\mathbf{r},t) = -\, K\nabla T(\mathbf{r},t), \tag{20}$$

where $\mathbf{J}(\mathbf{r},t)$ is the thermal energy flux crossing unit area, ρC_p is the volume heat capacity, $T(\mathbf{r},t)$ is the temperature, $A(\mathbf{r},t)$ is the rate of the deposited energy per unit volume in the substrate. Usually, the thermal radiation loss from the surface (proportional to the fourth power of the temperature at the surface) is equal to the thermal energy flux across the surface, which gives rise to one of the boundary conditions. However, the energy deposition rate is normally five to seven order of magnitude larger than the thermal radiation loss from the surface during a nanosecond pulsed laser heating. Therefore, the boundary conditions can be simplified as

$$dT(\mathbf{r},t)/dz = 0, \quad \text{for } z = 0, \tag{21}$$

$$T(\mathbf{r},t) = T_0, \quad \text{for } z = +\infty,$$

where T_0 is the initial temperature of the substrate.

The general solutions were derived in an early paper by Bechtel.[31] In our case, the laser pulse used has a Gaussian temporal profile, $I(\mathbf{r},t) = I(\mathbf{r})\exp(-t^2/\tau_p^2)$ with $\tau_p = 10$ ns

and the beam diameter (4 ~ 5 mm) is much larger than both the penetration depth and the thermal diffusion length so that the lateral heat conduction can be neglected. The laser-induced surface temperature rise at the center of the desorption beam is given by

$$\Delta T(x,y,z=0,t) = \frac{\Delta E}{\Delta A}(1-R)\cos(\theta_{inc})\frac{1}{\sqrt{\pi}\,\tau_p}\int_{-\infty}^{t}\frac{dt'}{\sqrt{\pi\rho C_p K}}\frac{e^{-t^2/\tau_p^2}}{\sqrt{t-t'}}, \tag{22}$$

where most importantly, $(\Delta E/\Delta A)(1-R)\cos(\theta_{inc})$ is the absorbed laser fluence by the substrate, θ_{inc} is the incident angle, R is the reflectivity at 1.064 μm at the incident angle, $\Delta E/\Delta A$ is the incident energy fluence at the center of the beam, ρ, C_p, K are the density, heat capacity and thermal conductivity, respectively.[30] With an initial temperature at 300 K and the peak temperature rise, ΔT_{max}, at 730 K (melting point of nickel is 1726 K), the surface temperature of nickel as a function of time during a 10 ns laser beam irradiation is shown in Fig. 6.

Such a rapid temperature rise at the Ni(111) surface causes CO molecules to desorb, the rate of desorption is described by Polanyi-Wigner equation [27]

$$\frac{d\theta}{dt} = -\nu\,\theta\,e^{-E_d/RT}, \tag{23}$$

where ν and E_d are known as the desorption preexponential factor and activation energy, respectively and $T = T_0 + \Delta T(x,y,z=0,t)$ is the total surface temperature. By integrating the rate equation, we find that after the pulsed laser heating, the remaining CO coverage $\theta(t\rightarrow+\infty)$ is given by

$$\theta(t\rightarrow+\infty) = \theta_s \exp\left[-\int_{-\infty}^{+\infty}\nu\,dt' e^{-E_d/RT(t')}\right], \tag{24}$$

which can be calculated given the surface temperature as a function of time, T(t), and the desorption kinetics constants, ν and E_d. In Fig. 7, we also show the calculated desorption rate, $d\theta/dt$, as a function of time together with the surface temperature assuming $\nu = 10^{13}$/sec and $E_d = 26$ kcal/mol. As we can see, most of the desorption occurs within a time duration of τ_p with a maximum at roughly $\tau_p/2$ after the peak of the 10 ns laser pulse. During this time, the surface temperature only varies a few percent from the maximum. From this observation, one immediately finds that Eq.(24) can be approximated

$$\theta(t \rightarrow +\infty) \approx \theta_s \exp\left\{ -\nu\, \tau_p \exp\left[-\frac{E_d}{R\,(T_0 + \Delta T_{max})} \right] \right\} . \tag{25}$$

where ΔT_{max} is proportional to the absorbed laser fluence according to Eq.(22). For a given set of desorption kinetic constants, ν and E_d, the remaining coverage $\theta(t \rightarrow +\infty)$ after desorption as a function of the absorbed laser fluence can be calculated from Eqs. (22) and (24) and compared with experimental results. Or alternatively, the experimentally measured dependence of the coverage change on the laser fluence can be used to determine the desorption kinetic parameters.[32] In Fig. 6, we show the theoretical calculation (solid line) assuming $\nu = kT\theta/h \sim 10^{13}$/sec, and E_d varies from 21 kcal/mol to 29 kcal/mol from the measurement of Christmann et al.[25] The results agreed well with our experimental measurements.

These results can now be used to determine the spatially modulated laser intensity needed for grating generation.

3. *Generation of a monolayer CO grating on Ni(111) by LITD with two interfering beams*

The experimental set-up for the grating generation is shown in Fig. 1(b). The sample is held at 140 K and initially dosed with CO to coverage $\theta = \theta_s = 0.5$ which

corresponds to the saturation coverage at room temperature. The two excitation beams have nearly Gaussian spatial profiles, $I_{1,2}(x,y) = I_{1,2}(0,0)\exp[-(x^2+y^2)/r_0^2)]$, with r_0 = 3.8mm. Based on the results of the laser-induced desorption measurement as discussed in the previous section, we choose the intensities of the two beams to yield a spatial modulation of the absorbed fluence across the irradiated surface as

$$I(x,y) = I_0 \left[1 + 0.55 \cos\left(\frac{\pi x}{a} \right) \right] \exp\left[- \frac{x^2 + y^2}{r_0^2} \right], \tag{26}$$

where I_0 is the averaged total absorbed fluence which is chosen to be 0.26 J/cm^2 at the center of the desorption beams. With $\phi_{exc} = \pm 1.5°$ and $\lambda = 1.064$ μm, the periodicity of the interference pattern and therefore the grating spacing is

$$2a = \frac{2\pi}{\Delta k_{\parallel}(\mathrm{LITD})} = \frac{\lambda}{2\sin(\phi_{exc})} = 20\ \mu\mathrm{m}. \tag{27}$$

From the results of the desorption yield measurement as shown in Fig. 6, we should expect a CO concentration grating to vary from less than 10% to over 99% of the initial coverage near the center of the desorption region. From the center toward the edge, the overall laser intensity decreases as $\exp[-(x^2+y^2)/r_0^2)]$, and we should also expect slow decreases ($r_0 >> a$) in both the depth and the width of the grating troughs.

We have assumed no lateral heat conduction in generating the temperature grating, $\Delta T(x,t)$. For the laser-induce surface heating by a single beam, since the time of desorption is on the order of τ_p, we could neglect the effect of lateral heat transfer as the laser beam diameter (r_0 = 3.8mm) is much larger than the thermal diffusion length for nickel ,

$$\xi = \frac{\sqrt{\pi\kappa\tau_p}}{2}, \tag{28}$$

which is estimated to be 0.5 μm for τ_p = 10 ns in our case (κ is the thermal diffusivity). In the case of surface heating by two interfering laser beams, since the periodicity of the optical interference pattern is in the micron range, and the thermal diffusion lengths are in the same range, it is important to examine its effect on the resultant temperature grating. If ξ is on the order of or larger than the grating spacing 2a, the profile of the surface temperature rise may not follow that of the laser intensity modulation and may even be completely smeared out by the lateral heat conduction. In this case, we will not be able to use the results shown in Fig. 6 to determine the profile of the coverage grating. We find that for an intensity profile given by Eq.(26), the resulting temperature modulation during the time of desorption is roughly given by [31]

$$\Delta T(x,T) = \Delta T_0 \left[1 + \frac{\Delta I}{I_0} \cos(\pi x/a)\, e^{-\xi^2/a^2} \right]. \tag{29}$$

In our case, since ξ = 0.5 μm, a = 10 μm, the effect of the lateral heat conduction can be completely neglected, and the temperature rise during laser desorption was still only determined by the local absorbed fluence. We have also examined the effect of CO surface diffusion on the grating profile during the laser heating. Similar to laser-induced thermal desorption, most of the diffusion occurs during a time duration of the order of τ_p as a result of the nature of activated reaction processes. Even near the peaks of laser intensity interference pattern, the CO molecules migrate only less than 1000Å [estimated from $(D\tau_p)^{1/2}$] which can be neglected (2a = 20 μm).

Quantitatively, we have calculated the grating profile with the distribution of the laser intensity interference pattern on the surface. Since the intensity envelope function $\exp[-(x^2+y^2)/r_0^2)]$ varies little over the grating spacing, at each point of the irradiated area, the local intensity modulation is essentially sinusoidal as given by Eq.(26). Using the

theoretical calculation in Fig. 6 as an approximation, we can calculate the local CO coverage profile after the desorption. In Fig. 8, we plot the calculated CO grating profile within one spatial period at various distances away from the center of the irradiated region. Here the coverage is normalized to the initial saturation coverage θ_s. The coverage near the center of the irradiated area changes from less than 10% to almost unchanged (more than 99%) with troughs and ridges having comparable widths. As we move to the edge, both the width and the depth of the depleted region decrease which are expected from the result of the LITD yield measurement.

In order to examine the calculated grating profile with the measurement of second-harmonic diffractions later, we have expressed the profile in Fig. 8 in a spatial Fourier series. Since the diameters of the desorption beams (therefore the grating size) is much larger than the grating spacing, $r_0 >> a$, we can express the local grating profile by well-defined Fourier components. From the symmetry of the excitation, we find,

$$\theta(x,y) = \theta_0 + \sum_{n=1} \theta_n(x,y) \cos(n\pi x/a) , \tag{30}$$

where $\theta_n(x,y)$ vary slowly across the beam diameter. This is done by dividing the entire grating area ($r < 0.6\, r_0$) into six coaxial sections with boundaries at $r = 0.1\, r_0$, $0.2\, r_0$, $0.3\, r_0$, $0.4\, r_0$, $0.5\, r_0$, $0.6\, r_0$ around the co-center of the two desorption beams. In each section, the grating profile does not change appreciably and we could perform numerical Fourier transformation. For $r > 0.6\, r_0$, the grating modulation is vanishingly small and therefore neglected. In Fig. 9, we depict the θ_0, θ_1, θ_2, θ_3, θ_4 as a function of distance, r, away from the beam center. We notice that the average coverage within the grating is roughly $\theta_0 \sim 0.6$ relative to the saturation coverage, and the first Fourier component which determines the light diffraction efficiency is close to the optimum, $\theta_1 \sim 0.4$ to 0.5. These results will

be used to calculate the signals of the optical second-harmonic diffractions and compared with the diffraction measurement.

4. *Characterization of the monolayer CO grating by optical second-harmonic diffraction:*

Linear and nonlinear light diffractions have been extensively used to characterize periodic structures of the dimensions of optical wavelengths and to study various physical properties associated with the structures such as real time holography, phase conjugation, laser actions and various material relaxations and diffusions in bulk media. In principle, we should be able to apply the same methods to monolayer atomic or molecular gratings to study physical phenomena on surfaces.[34] However, linear scattering off a grating as thin as one molecular layer suffer from the interference from diffusive bulk scattering which can easily overwhelm the surface contributions. Such an interference from the bulk is greatly suppressed in optical second-harmonic diffractions from a monolayer grating due to the forbidden nature of the electric dipole radiation from the underlying centrosymmetric bulk. Therefore, we chose to use second-harmonic diffractions to characterize the monolayer CO grating. This enabled us to measure the diffraction signals from the CO monolayer grating up to fourth order.

From the previous calibration as given by Eq. (15) and (16), we know that for Ni(111), the surface nonlinear susceptibility changes linearly with the CO coverage. Hence, we expect that the n-th order second-harmonic diffraction is only contributed from the n-th spatial Fourier component of the monolayer grating as in an ordinary linear grating diffraction. The diffraction angles are determined by phase-matching conditions

$$k_{x,n}(2\omega) = 2k_x(\omega) + \frac{n\pi}{a}, \tag{31}$$

where $k_{x,n}(2\omega)$ is the wave vector of the n-th second-harmonic diffraction in x-direction along the surface, $n = 0, \pm 1, \pm 2, \pm 3$, etc.

The second-harmonic diffraction experiment was performed with the same set-up as shown in Fig. 1(b). The sample was held at 140 K before and after the grating generation so that the effect of the surface diffusion on the characteristics of the grating is negligible even at times many hours after the grating is formed. The probe beam intensity at wavelength of 0.532 μm has a nearly Gaussian profile, $I_p(x,y)=I_p(0,0)\exp[-(x^2+y^2)/b^2)]$ with b = 1.16mm. At 71.4° incidence, the probe beam spreads along x-direction and covers the grating. We are able to observe SHG diffractions up to 4th order. They correspond to $n = +1, -1, -2, -3, -4$ and are at + 2.52°, − 2.22°, − 4.24°, − 6.1°, and − 7.84°, respectively off the specular reflection direction as we have expected from the phase matching conditions. We also measure the specular second-harmonic reflection to determine the average CO coverage, θ_0. The square roots of the measured second-harmonic diffractions vs. diffraction order are plotted in Fig. 11 (open columns). The signals are normalized to that of the specular SHG which has a signal strength of 160 photons per pulse.

To deduce the information about the grating profile from the second-harmonic diffractions, we can compare the signals with the predictions from the desorption yield measurement which led to the Fourier expansion given by Eq. (30). For a grating profile $\theta(x,y)$, we have

$$\chi_0(2\omega; x,y) = \left[A + B\theta_0(x,y) \right] e^{i2k_x(x)x - i2\omega t}, \tag{32}$$

$$\chi_n(2\omega; x,y) = \left[\frac{B\theta_n(x,y)}{2} \right] e^{i[2k_x(\omega)+\frac{n\pi}{a}]x - i2\omega t}, \tag{33}$$

where $n = \pm 1, \pm 2, \pm 3$, etc. The second-harmonic diffraction signals can then be obtained from

$$SHG_0 = C \iint \left| A + B\theta_0(x,y) \right|^2 I_{p'}^2(x,y)\, dx\, dy \ , \tag{34}$$

$$SHG_n = C \iint \left| \frac{B\theta_n(x,y)}{2} \right|^2 I_{p'}^2(x,y)\, dx\, dy \ , \tag{35}$$

where C is a constant which includes the time integration, $I_{p'}(x, y)$ is the probe beam intensity profile at the surface. From our previous calibration given by Eq. (17), B/A = – 0.68 and the numerical values of $\theta_n(x,y)$ shown in Fig. 9, we calculate the diffracted SHG signals of various order. The calculated signals normalized to the specular reflection are also plotted in Fig. 10 (shaded columns).

The agreement between the measurement and the prediction from the LITD experiment is remarkably well. This shows that the actual grating profile on the surface is quite well predicted from the result of LITD yield measurement. Furthermore, It demonstrates our ability to quantitatively control the generation and characterization of a monolayer grating of small molecules. Now we have paved the way for surface diffusion study which is our final goal.

5. *Surface diffusion of CO on Ni(111) studied by the optical second-harmonic diffraction off the monolayer CO grating*

After a monolayer grating is formed, the lateral motion of the remaining adsorbates in the direction normal to the troughs gradually smears out the the grating modulation until the spatial inhomogeneity of the coverage distribution disappears. At high enough temperatures, such a smearing-out effect is sufficient and can be observed through the change in the diffraction of SHG. The temperature dependence of the decay rate of the diffracted SHG can be used to deduce the diffusion constant from which we obtain the kinetics parameters governing the surface motion of CO on Ni(111).

The experiment is performed at four different sample temperatures, 219K, 247K, 261K, 273K. With operating pressure at 8×10^{-11} torr, the effect of readsorption from ambient during the course of the measurements was found negligible from the measurement of the specular SHG. Before each measurement, the cleaned sample is held at the desired temperature and dosed with CO to $\theta = \theta_s = 0.5$. Subsequently, we apply the interfering pulse pair to create the monolayer grating. Care has been taken to properly reduce the desorption beam intensities with the elevated surface temperature in order to maintain the same initial grating profiles for all measurements. The average coverage is monitored with specularly reflected SHG and kept essentially the same in all the measurements. We monitor the first-order diffraction signal corresponding to $n = -1$ to study the diffusion of CO. The measurement starts a few minutes after the grating is formed. In Fig. 11, we plot the measured SH diffraction signal as a function of time at the four selected sample temperatures. The diffracted SHG signal decays with time and the decay rate is strongly temperature-dependent as we would expect for an activated diffusion of CO.

To extract the kinetics parameters governing the lateral motion of CO molecules, we need to relate the evolution of the grating profile to the diffusion kinetics models. Since only the lateral motion perpendicular to the grating troughs contributes to the change of the monolayer grating, this relation is given by the one-dimensional diffusion equation, or Fick's law

$$\frac{\partial \theta}{\partial t} = \frac{\partial}{\partial x}\left(D \frac{\partial \theta}{\partial x} \right). \tag{36}$$

From the symmetries of the initial and the boundary conditions, at any time t after the grating formation, we can express $\theta(x, y, t)$ as

$$\theta(x,y,t) = \theta_0(x,y) + \sum_{n=1} \theta_n(x,y,t) \cos(n\pi x/a) . \tag{37}$$

If we assume that the diffusion coefficient D is weakly dependent on the coverage so that

$$D(\theta) \approx D(\theta_0) , \tag{38}$$

it is then easy to see that different Fourier components are not coupled to one another through the diffusion equation, and the time dependencies of these components are described by single-exponential functions. In particular, we have

$$\theta_1(x,y,t) = \theta_1(x,y,0)\, e^{-\pi^2 D(\theta_0)\, t/a^2} , \tag{39}$$

and

$$SHG_1(t) = SHG_1(0)\, e^{-2\pi^2 D(\theta_0)\, t/a^2} . \tag{40}$$

In Fig. 11, we show the fit using single exponential functions to the measured SHG signals (solid curves). The quality of the fit is fairly good within the experimental error. This indicates that our assumption as given by Eq. (38) is a fairly good approximation.

From the exponents, $2\pi^2 D(\theta_0)/a^2$, we deduce the diffusion coefficient $D(\theta_0)$ as a function of temperature. In Fig. 12, we depict the Arrehnius plot of the diffusion coefficient D(T) as a function of the sample temperature. From a least-square fit assuming $D(T) = D_0 \exp(-E_{diff}/RT)$, we find that for CO on Ni(111),

$$E_{diff} = 6.9 \pm 1.0 \text{ kcal/mol} ;$$

$$D_0(\theta_0) = 1.2 \times 10^{-5} \text{ cm}^2/\text{sec}, [\text{ or } \ln\{D_0(\theta_0)\} = -11.4 \pm 2.0] , \tag{41}$$

where θ_0 is the averaged coverage, $\theta_0/\theta_s = 0.6$.

The measured value of the preexponential factor, $D_0 \sim 1.2 \times 10^{-5}$ cm^2/sec, is small compared to an estimate of 2×10^{-4} cm^2/sec from a random walk model $D_0 = a^2\nu_{d0}/4$ if we take the mean jump length **a** ~ 1.25Å (the spacing between the nearest neighboring bridge sites on Ni(111)) and the mean jump frequency $\nu = kT/h \sim 5 \times 10^{12}$/sec. It is also small compared to that for CO on Rh(111). However, it is comparable to those found on Pt(111) and W(110) which were reported to be $\leq 10^{-4}$ cm^2/sec and 1.3×10^{-5} cm^2/sec, respectively.[3, 7]

From this preliminary measurement, the measured diffusion activation energy for CO on Ni(111), 6.9 kcal/mol, compares well with that found for CO on Rh(111), 7.1 kcal/mol (the diffusion constant was found only weakly dependent on the CO coverage) and on Pt(111), 7.0 kcal/mol, reported by other groups.[3] This suggests the similarity of the surface lateral potentials seen by CO on these close-packed fcc transition metal surfaces. As pointed out in a recent paper by Seebauer et al,[3] this energy is close to the experimentally measured activation energies of a number of Langmuir-Hinshelwood reactions on many close-packed transition metal surfaces which involve CO as one of the reactants. Therefore, the diffusion of CO is most likely to be the limiting factor in these important catalytic reactions.

One of the most important issues in a surface diffusion study is to determine the pathway of the molecular motion. At low enough temperatures, the diffusion pathway is the one which has lowest energy barrier as the preexponential factors D_0 are not expected to be much different for different paths. Generally, it is conceivable that such paths are along symmetry lines of the surface. Since bridge sites are the energetically favored for CO on Ni(111) at coverages below $\theta = 0.5$, we should expect the diffusion to occur mostly between two bridge-bonded sites. However, without knowing the surface potential distribution, there are more than one routes which can connect one bridge site to another. Furthermore, as we will show in the discussion section, for (111) and (100) surfaces, it is not possible to determine the diffusion pathways by a measurement of anisotropy of the

diffusion constant simply because the average over a large number of hoppings in a macroscopic measurement always leads to an isotropic diffusion constant no matter which microscopic pathway operates. The theoretical calculation of the surface energy distribution for CO on Ni(111) was attempted in an early paper by G. Doyen and G. Ertl using an atomic and molecular orbital calculation.[35] They predicted that the lowest energy site should be bridge-bonded which is consistent with the experimental observations. However, their calculation also suggested that there was essentially no energy barrier between the next nearest neighboring bridge sites which would lead to the conclusion that CO should slide on the surface with no energy barrier. This is clearly in contradiction with our observation of an activated diffusion for CO on Ni(111). To the best of our knowledge, there are no other refined theoretical calculations with which our measurement can be compared.

Nonetheless, there are some evidences which seem to suggest that CO may in fact diffuse between two bridge sites by crossing the on-top site. It is instructive to note that the on-top (linearly bonded) sites have been found to be energetically favored only second to bridge-bonded sites. At low temperatures (below 270 K) and coverages above $\theta = 0.5$, they become occupied even at the expense of rearranging some of bridge-bonded CO into on-top-bonded CO.[25] From the thermal desorption measurements,[33] it has been established that those CO at on-top sites desorb prior to those at the bridge sites, with an activation energy of 18 kcal/mol. It is about 4 to 6 kcal/mol smaller than that for bridge-bonded CO at the same coverage. Furthermore, we notice that in low temperature (~ 80K) adsorption studies by vibrational spectroscopy, only bridge-bonded CO have been reportedly observed.[26] Since the on-top sites have equal probability to be struck by the incoming molecules and the spectroscopy measurements usually take at least seconds, we come to the conclusion that within seconds, those CO landed onto on-top sites must have already moved to bridge-bonded sites through single-step hoppings over the barrier between an on-top site and a bridge site. Since the preexponential factor, ν_{d0}, of the

hopping rate ranges from 10^{10}/sec [CO on Pt(111) [8]] to 10^{12}/sec (estimated from kT/h with $T \sim 80$ K), the barrier from a on-top site to a neighboring bridge site can then be estimated to be less than 3 to 4 kcal/mol. This leads to an energy barrier between two bridge sites over an on-top site to be around 7 to 10 kcal/mol as shown in Fig. 13. This is very close to our measured diffusion activation energy barrier, 6.9 kcal/mol which suggest that diffusion between bridge sites through hopping over on-top sites is a highly likely pathway for CO on Ni(111). In fact, the similar correlation has also been reported for CO on Rh(111).[3]

F. Discussion

We now discuss some of the general features of this new technique. We first examine some important aspects of data analysis which are essential in some of the future applications of this technique. We address the unique advantages of this novel technique that are specially attractive for diffusion studies and point out its important applications in the future.

1. *Coverage dependence of surface diffusion kinetics*

The coverage dependence of diffusion constants bear much information on the nature of adsorbate-adsorbate interaction and adsorbate-substrate interaction. One of the objectives in an experimental study of surface diffusion is to investigate such a dependence. With this monolayer grating diffraction technique, we note that a coverage dependent $D(\theta)$ causes different Fourier spatial components to couple with one another through the diffusion equation. Such couplings in turn cause $\theta_1(t)$ or all $\theta_n(t)$ to deviate from single exponential functional forms. In the Appendix, we have analyzed more explicitly the effect of these couplings on the temporal behaviors of $\theta_n(t)$. In principle, measurements of other

Fourier components besides $\theta_1(t)$ as functions of time should yield more information which can be used to extract the diffusion constant as a function of coverage. As we have shown in the Appendix, it may be more practical and simpler to perform the measurement with a reduced initial grating modulation about an average coverage. In this way, at least for many strong coverage-dependent diffusion processes, the first order Fourier component still decays exponentially and the exponent is directly proportional to the diffusion coefficient at the average coverage. By varying the average coverage, one can obtain the coverage dependence of the diffusion kinetics parameters. This method requires only a simple analysis of the data.

In our case, the measured first-order diffraction signal is found fairly well fitted with a single exponential decay function. From the measurement of the first and second-order diffraction signals, we know that initially, $|\theta_1(0) / \theta_s| = 0.5$, and $|\theta_2(0) / \theta_s| = 0.15$. From the discussion in the Appendix, we can conclude that the diffusion constant D of CO can only have a weak dependence of the coverage on Ni(111) so that,

$$\left| \frac{d(\ln D)}{d\theta_0} \right| \leq 2 \ , \tag{42}$$

and the temporal dependence of the diffraction signal could be well approximated with a single-exponential function, and the exponent could be simply related to the diffusion constant at the average coverage, $\theta_0/\theta_s = 0.6$. If we assume that $E_{diff} = \Delta E = \Delta E_0 + \varepsilon\theta$, Eq. (42) means that the diffusion energy barrier should not change more than 2 kcal/mole in the entire coverage range. Similar observation for CO diffusion on Rh(111) have also been reported.[3]

2. *Influence of complex coverage dependence of SHG*

In the case of CO on Ni(111), the surface nonlinear susceptibility is found to be linearly dependent on the coverage to a good approximation. This leads to the conclusion that the n-th order second-harmonic diffraction is contributed only from the n-th Fourier component of the monolayer grating. In general, the nonlinear susceptibility of a surface can have a complex dependence on the adsorbate coverage. In the process of second-harmonic diffraction, this leads to apparent coupling among different Fourier components.

We can write, for $B(\theta)$ in $\chi(2\omega)$ in Eq. (10),

$$B(\theta) = B(\theta_0) + \left(\frac{dB}{d\theta_0}\right)(\theta - \theta_0) + \frac{1}{2}\left(\frac{d^2B}{d\theta_0^{\,2}}\right)(\theta - \theta_0)^2 + 0(\theta - \theta_0)^3 , \tag{43}$$

$$\theta - \theta_0 = \sum_{n=1} \theta_n(x,y,t)\cos(n\pi x/a) . \tag{44}$$

The higher order terms in Eq. (43) contribute to the couplings among different Fourier components in the diffraction process. The effect is the same as with a coverage dependent $D(\theta)$ which we have discussed in the Appendix. By using reduced modulations of monolayer gratings, the contributions to the first order diffraction from other Fourier components can be made negligible, and we should still expect

$$SHG_1(t) = C' \left| \frac{dB}{d\theta_0} \right|^2 \theta_1^{\,2}(t) = C'' e^{-2\pi^2 D(\theta_0)\, t / a^2} . \tag{45}$$

In cases where the electronic configuration changes drastically at some discrete coverages, we expect large changes in diffusion kinetics. Such cases can be studied by comparing the measurements on both sides of these coverages.

3. *Effect of surface defects on the experimental determined diffusion constant*

Surface defect sites are normally 10^{-3} to 10^{-4} as dense as the " healthy" sites on many of low index single crystalline planes.[8] They can play active roles in surface reactions. Surface diffusions involving these sites are particularly important. The defect sites can significantly change the diffusion coefficients at low coverages ($\theta \sim 10^{-3}$ to 10^{-4}) in an often unspecified way. They may trap adsorbates for so long that on the average, the diffusion time may be predominantly determined by the escape times or the lifetimes of the adsorbates at these sites.

However, at coverages as high as 0.1 to 0.5 which is the case in our experiment, majority of the diffusing molecules hop between "healthy" sites with the defect sites playing a minor role. Therefore, the experimentally measured diffusion coefficients are hardly affected by the defect unless they are in the form of long lines or steps. In the latter case, even at low densities, they may block the diffusion paths along a given direction such that the particles must take on much longer alternative paths. This can lead to reduced preexponential factors even though the activation energy is still that for diffusion between two perfect sites. We note that this may play a role in the measured preexponential factor D_0 for CO on Ni(111) and Pt(111) which were found small compared to those reported on other close-packed fcc transition metal surfaces. Such an effect may be resolved in a measurement of anisotropy of surface diffusion as we will discuss next.

4. *Studies of anisotropy in surface diffusion*

One of the most important features of this technique is that it enables us to readily study the anisotropy of diffusion processes on a surface.[36] By varying the orientation of the monolayer grating with respect to a given surface crystalline direction, we can obtain the azimuthal angle-resolved distributions of diffusion kinetics parameters.

For surfaces such as (111) and (100) planes, the macroscopic diffusion constants are isotropic as a result of averaging over large number of microscopic hoppings. This can be shown by a simple argument. In a typical measurement of a macroscopic diffusion over a distance of microns or more, each diffusing particle moves on the average 10^8 to 10^{10} steps on the surface. On a (111) surface for example, there are three equivalent directions ($\mathbf{e}_1$, $\mathbf{e}_2$, $\mathbf{e}_3$) along each of which the diffusing particle can move randomly back and forth. Since an overwhelmingly large number of steps are involved in a macroscopic observation, one can evenly distribute these steps over the three directions, and treat a two-dimensional diffusion as a vector sum of three one-dimensional diffusions along the three equivalent directions. In a given direction **n**, the distance traveled by a diffusing particle after a time t is given by

$$r_{\mathbf{n}}(t) = r_1(t)\,(\mathbf{n}\cdot \mathbf{e}_1)\,\mathbf{e}_1 + r_2(t)\,(\mathbf{n}\cdot \mathbf{e}_2)\,\mathbf{e}_2 + r_3(t)\,(\mathbf{n}\cdot \mathbf{e}_3)\,\mathbf{e}_3 \ . \tag{46}$$

As the result of random nature of the microscopic hoppings, after a macroscopic observation time t, the square of the averaged distance traveled by the particle is then determined by

$$< r_{\mathbf{n}}^2 > = \frac{N(t)}{3}\,[\,(\mathbf{n}\cdot \mathbf{e}_1)^2 + (\mathbf{n}\cdot \mathbf{e}_2)^2 + (\mathbf{n}\cdot \mathbf{e}_3)^2\,]\,\mathbf{a}^2 = \frac{\mathbf{a}^2\,\nu_d(T)\,t}{2} \ . \tag{47}$$

The result is independent of the selection of **n**! The same analysis for a square lattice leads to the same conclusion as given by Eq. (47). Therefore, we conclude that no matter what and how many diffusion routes operate, macroscopic diffusion constants on (111) or (100) surfaces are always isotropic and hence it is not possible to determine diffusion pathways by a measurement and analysis of anisotropy of the diffusion.

In the presence of steps or line defects which are preferentially oriented or can be so created, the contributions from the "perfect" part of the surface and the line defects can be separated through an anisotropy measurement, which are otherwise rather difficult to handle.[8]

On an anisotropic surface, such anisotropy study directly gives us information about anisotropic distribution of the surface potential. These information are often most interesting and crucial to our understanding of surface molecular dynamics.[21] We are currently investigating the diffusion of CO on Ni(110). On this surface, molecules and atoms have also been found to be chemically more reactive than on low index planes of nickel.

5. *Studies of surface diffusion with large Dynamic range*

Another important feature of this technique lies in the fact that grating spacings can be easily varied experimentally from a few hundred microns to about one micron. This allows us to study slow as well as fast diffusion at low enough temperatures to avoid undesired effects of thermal desorption.[3] This can be understood from the following analysis. In a measurement of a macroscopic diffusion across a characteristic distance, **a**, one finds that the macroscopic coverage change (no matter how it is monitored) evolves roughly as $\exp(-\pi^2 Dt/\mathbf{a}^2)$. The characteristic diffusion time can be defined at the 1/e point as

$$t_{diff} = \frac{\mathbf{a}^2}{\pi^2 D} = \frac{\mathbf{a}^2}{\pi^2 D_0} \exp\left(\frac{E_{diff}}{RT}\right), \tag{48}$$

which is proportional to $\mathbf{a}^2$. In order to follow a surface diffusion under UHV condition with base pressures typically in the range of 10^{-10} torr, one needs to operate at such

sample temperatures that the diffusion times, $t_{diff} \leq 1$ to 2 hours to avoid the effect of readsorption. This sets a *lower* limit of the sample temperature for the surface diffusion measurement. Secondly, thermal desorption of the same system is governed by a preexponential factor ν and desorption energy E_d. From Eq. (23), we can define the desorption time as

$$t_d = \frac{1}{\nu} \exp\left(\frac{E_d}{RT} \right). \tag{49}$$

To avoid the effect of thermal desorption on the surface diffusion measurement, we must require $t_{diff} \leq t_d$, which sets the *upper* limit for the sample temperature for diffusion measurement. This implies that the slowest diffusion which can be measured is proportional to the square of the macroscopic diffusion distance, **a**, involved in the experiment. Given the upper limit of the sample temperature, the monolayer grating diffraction technique with adjustable grating spacings enables us to investigate diffusion processes which are 10^{-4} to 10^{-5} as slow as those measurable with the "hole-burning" LITD method. CO diffusion on Ni(111) represents one of the examples of slow molecular diffusions.

For generation of monolayer gratings with spacings of microns or a fraction of a micron by laser-induced desorption, one should be more careful to properly avoid the effects of the thermal diffusion and the transient surface diffusion during laser heating.

6. *Extension to investigation of diffusions with co-adsorbed species*

One of the most interesting and also less investigated subjects in the surface diffusion studies is lateral molecular motions in the presence of other species.[37] For such studies, one needs to probe the molecules with selectivity. This should be achieved by

diffractions of resonant optical second-harmonic generation so that only one type of the coadsorbed species is under observation at a time even in the presence of others.[38]

G. Conclusion

To summarize, we have developed a novel technique to study molecular surface diffusions by diffractions of optical second-harmonic generation off a monolayer grating. Such a grating can be prepared in a controlled fashion by laser-induced desorption with two interfering laser pulses. We have applied this technique to study the diffusion of CO on Ni(111). The preliminary results allow us to deduce the diffusion activation energy to be 6.9 ± 1.0 kcal/mol, and preexponential factor D_0 to be 1.2×10^{-5} cm^2/sec. Further analysis suggests that CO is likely to diffuse across on-top sites which joint two neighboring bridge sites. This new technique has a number of important features over existing techniques. It should significantly enhance our ability in the future studies of surface diffusion dynamics and surface morphology and other related subjects.

H. Appendix: solutions of one dimensional Fick's for coverage dependent surface diffusion

A strong coverage-dependent surface diffusion constant will result in coupling among different Fourier spatial components of a monolayer grating through the diffusion equation, and cause the deviation of their time-dependence away from single-exponential functions. In this section, we examine explicitly such an effect on the temporal evolution

of an initially symmetric grating-like concentration profile. We will derive a more detailed form of the diffusion equation for each Fourier component using a perturbation expansion. Then we will determine the conditions under which we can simply and reliably extract diffusion kinetic parameters from a light diffraction measurement.

Generally speaking, if the adsorbate-adsorbate interaction energies are small compared to kT and the substrate structure does not significantly change in the presence of adsorbates, we should expect a weak coverage dependence in the adsorbate diffusion kinetics. However, if the interaction energies are comparable or more large compared to kT, or the surface structure undergoes phase changes such as relaxations or reconstructions in the presence of adsorbates, we should then expect large dependence of diffusion kinetics on the adsorbate coverage.

It is helpful to examine the expected ranges of coverage dependence of diffusion constants D_0 from the existing experimental results obtained on many adsorbate-substrate systems. Although each system can be very different from others in detail, the informations obtained from these known systems are useful and often enough (except for special cases) for us to anticipate the coverage dependence for many systems. There have been a number of experimental studies of the coverage dependence of both atomic and molecular adsorbates on metal and semiconductor surfaces. One of the systems which has shown the strongest coverage-dependence of the diffusion kinetics is oxygen on W(110). In this case, the overall diffusion constant was found changing by two to three orders of magnitude over the entire coverage range, namely,

$$\frac{d[\ln(D)]}{d\theta} = 4 \text{ to } 8 . \qquad (1)$$

Most other systems studied so far show much more modest coverage dependence, except for special situations, we can use this case as an example of upper limits.

We start by noting that for small enough modulations of a grating profile, we can expand the diffusion constant $D(\theta)$ around the average coverage θ_0,

$$D(\theta) = D(\theta_0) + \left(\frac{dD}{d\theta_0}\right)(\theta - \theta_0) + \left(\frac{d^2D}{d\theta_0^{\,2}}\right)\frac{(\theta - \theta_0)^2}{2} + \cdots \tag{2}$$

$$\theta - \theta_0 \equiv \Delta\theta = \sum_{n=1}^{\infty} \theta_n(t)\cos(n\pi x/a)\,. \tag{3}$$

From the one-dimensional diffusion equation given in Eq.(36), it is easily found that

$$\sum_{n=1} \frac{d\theta_n}{dt}\cos\left(\frac{n\pi x}{a}\right) = \frac{d}{dx}\left[D(\theta_0)\frac{d(\Delta\theta)}{dx}\right] + \frac{d}{dx}\left[\frac{dD}{d\theta_0}(\Delta\theta)\frac{d(\Delta\theta)}{dx}\right], \tag{4}$$

here we have omitted terms of the order of $0(\theta - \theta_0)^3$ on the right hand side. The first few Fourier components are usually dominant and therefore are monitored in the experiments, we will focus our discussion on their temporal dependence. By multiplying $\cos(n\pi x/a)$ and integrating on both sides of the equation, we have

$$\frac{d\theta_1}{dt} = -D(\theta_0)(\pi/a)^2\left[1 + \frac{d(\ln D)}{d\theta_0}(\theta_2/2)\right]\theta_1 - \frac{dD}{d\theta_0}(\pi/a)^2\sum_{n=2}\frac{\theta_n\,\theta_{n+1}}{2}\,, \tag{5}$$

$$\frac{d\theta_2}{dt} = -D(\theta_0)(2\pi/a)^2\left[1 + \frac{d(\ln D)}{d\theta_0}(\theta_4/2)\right]\theta_2 - \frac{dD}{d\theta_0}(2\pi/a)^2\sum_{n\neq 2}\frac{\theta_n\,\theta_{n+2}}{2} - \frac{dD}{d\theta_0}(\pi/a)^2\,\theta_1^{\,2}\,. \tag{6}$$

The equations for the third and the fourth Fourier components and so on are similar to Eq. (6). In general, these nonlinear equations are still difficult to solve for an arbitrary initial

condition, and therefore one may have to seek often involved numerical calculations. However, if the various components $\theta_n(t)$ can be experimentally determined, one can use Eq. (5) and (6) to determine $D(\theta_0)$ and $d\{\ln(D)\}/d\theta_0$ or even other higher order expansion derivatives.

On the other hand, if we can start with a grating with a small modulation so that $1 >> \theta_1 > \theta_2, \theta_3, \theta_4$ and so on (for example, a grating with a shallow but nearly sinusoidal or even square-wave profile), the above equations can be approximated as

$$\frac{d\theta_1}{dt} = -\alpha\left(1 + \frac{\theta_2\,\beta}{2}\right)\theta_1, \tag{7}$$

$$\frac{d\theta_2}{dt} = -4\,\alpha\,\theta_2 - \alpha\,\beta\,\theta_1^2\,. \tag{8}$$

for the convenience of algebra, we have defined $\alpha = D(\theta_0)(\pi/a)^2$ and $\beta = d(\ln D)/d\theta_0$. As we can see, as long as $(\theta_2\beta)/2$ is small compared to unity, the time dependence of θ_1 is well approximated with a single-exponential function, and the exponent α is simply related to the diffusion constant $D(\theta_0)$ at the average coverage. Since θ_2 is coupled to θ_1 through Eq. (8), it is not sufficient only to reduce the initial value of θ_2. We also need to properly limit the initial value of θ_1. By explicitly integrating the second equation using the zeroth-order solution of Eq. (7), we find that this approximation holds well provided that

$$\frac{\theta_2(0)\cdot\beta}{2} << 1, \text{ and } \frac{\theta_1^2(0)\cdot\beta}{16} << 1. \tag{9}$$

Consider, for example a diffusion coefficient $D(\theta)$ with a coverage dependence which leads to

$$\beta = \left| \frac{d(\ln D)}{d\theta_0} \right| = 6 . \tag{10}$$

In order to have the first order Fourier component decay exponentially with the measured exponent $\alpha(\theta, T)$ directly related to the diffusion constant $D(\theta,T)$, we only need to control the modulations of the created monolayer gratings so that

$$\left| \frac{\theta_1(0)}{\theta_s} \right| \leq 0.2 ,$$

$$\left| \frac{\theta_2(0)}{\theta_s} \right| \leq 0.03 ,$$

$$\left| \frac{\theta_{n \geq 3}(0)}{\theta_s} \right| \leq 0.03 . \tag{11}$$

Such a control is possible as has been demonstrated in our experiment. Since the diffracted light signal strength is proportional to the square of the corresponding spatial Fourier component, compared to the experimental condition which we used for CO on Ni(111), $\theta_1 \sim 0.5$, we expect a signal drop by a factor of 4 ~ 6 which is still tolerable. With improvements on the grating preparation and detection, the overall signal strength can be increased substantially.

Hence we can conclude that in many cases, with modestly reduced grating modulations and properly controlled initial conditions, the temporal evolution of the first order spatial Fourier component $\theta_1(t)$ can be fairly well approximated with a single exponential function. The exponent is simply related to the diffusion constant at the selected average coverage. Experimentally, the time dependent $\theta_1(t)$ can be conveniently measured with optical second-harmonic diffractions. In cases when other Fourier components are significantly large and can be monitored with higher order diffractions of second-harmonic generation in addition to the first component, the temporal changes of

these components should also give us the information which can equally well lead to the determination of the diffusion constant and its coverage dependence.

For a preliminary analysis of the coverage dependence of the diffusion constant for CO, the initial grating modulation is essentially characterized by that at the center of the irradiated Ni(111) surface,

$$\theta_1(0) = -0.5,$$
$$\theta_2(0) = -0.16,$$
$$|\theta_{3,4}(0)| < |\theta_2(0)|. \tag{12}$$

Since the time dependence of θ_1 is found to be fitted well with a single exponential function within the experimental error which is 10%, we should expect that

$$\beta(\theta_0) = \left| \frac{d(\ln D)}{d\theta_0} \right| \leq 2 . \tag{13}$$

In terms of the upper limit of the activation energy barrier, if we assume $E_{diff} = \Delta E_0 + \varepsilon\theta$, this means that E_{diff} will not change by more than 2 kcal/mol over the entire coverage range for CO on Ni(111).

References:

1. G. Ehlich, and Kaj Stolt, Ann. Rev. Phys. Chem. 31, 603 (1980);
   A. G. Naumovets, and Yu. S. Vedula, Surf. Sci. Rep. 4, 365 (1985).
2. G. A.Somorjai, Chemistry in Two Dimensions: Surfaces (Cornell University Press, Ithaca, 1981).
3. B. Lewis, Surf. Sci. 21, 273, 283 (1970);
   A. Kobayashi, Sun-Mok paik, K. E. Khor, and S.Das Sarma, Surf. Sci. 174, 48 (1986);
   E. G. Seebauer, A. C. F. Kong, and L. D. Schmidt, J. Chem. Phys. 88, 6597 (1988), and references therein;
   A. G. Naumovets, V. V. Poplavsky, and Yu. S. Vedula, Surf. Sci. 200, 321 (1988).
4. J. D. Doll and A. F. Voter, Ann. Rev. Phys. Chem. 38, 413 (1987).
5. G. Ehrlich, Surf. Sci. 63, 422 (1977);
   G. L. Kellogg, T. T. Tsong, and P. Cowan, Surf. Sci. 70, 485 (1978).
6. G. Binnig, H. Fuchs, and E. Stoll, Surf. Sci. 169, L295 (1986);
   R. C. Jaklevic and L. Elie, Phys. Rev. Lett. 60, 120 (1988).
7. R. Gomer, Surf. Sci. 38, 373 (1973);
   J. R. Chen, and R. Gomer, Surf. Sci. 81, 589 (1979);
   R. Gomer, Vacuum 33, 537 (1983).
8. J. E. Reutt-Robey, D. J. Doren, Y. J. Chabal, and S. B. Christman, Phys. Rev. Lett. 61, 2778 (1988).
9. S. S. Iyer, T. F. Heinz, and M. M. T. Loy, J. Vac. Sci. & Technol. B 5, 709 (1987).
10. Po-Kang Wang, Jean-Phillipe Ansermet, C. P. Slichter, and J. H. Sinfelt, Phys. Rev. Lett. 55, 2731 (1985);
    Po-Kang Wang, Jean-Phillipe Ansermet, S. L. Rudaz, Z. Wang, S. E. Shore, C. P. Slichter, and J. H. Sinfelt, Science 234, 35 (1986);

S. E. Shore, Jean-Phillipe Ansermet, C. P. Slichter, and J. H. Sinfelt, Phys. Rev. Lett. 58, 953 (1987).

11. H. P. Bonzel, and E. E. Latta, Surf. Sci. 76, 275 (1978);
P. Meakin, J. Chem. Phys. 88, 2036 (1988).
12. A. P. Janssen, Surf. Sci. 52, 230 (1975).
13. R. Butz, and H. Wagner, Surf. Sci. 63, 448 (1977).
14. R. Viswanathan, D. R. Burgess,Jr., P. C. Stair, and E. Weitz, J. Vac. Sci. Technol. 20, 605 (1982);
S. M. George, A. M. DeSantolo, and R. B. Hall, Surf. Sci. 159, L425 (1985);
A. A. Deckert, J. L. Brand, M. V. Arena, and S. M. George, Surf. Sci. 208, 441 (1989), and references therein.
15. X. D. Zhu, and Y. R. Shen, Opt. Lett. 14, 503 (1989).
X. D. Zhu, Th. Rasing, and Y. R. Shen, Phys. Rev. Lett. 61, 2883 (1988).
16. M. Bowker, and D. A. King, Surf. Sci. 71, 583 (1978).
17. H. Asada, and M. Masuda, Surf. Sci. 99, L429 (1980);
R. Morin, and M. Drechsler, Surf. Sci. 111, 140 (1981);
D. R. Bowman, Surf. Sci. 130, 348 (1983);
M. D. Miller, Surf. Sci. 127, 383 (1983);
V. P. Zhdanov, Surf. Sci. 149, L13 (1985);
V. P. Zhdanov, Surf. Sci. 187, L642 (1987).
18. A. M. Stoneham and J. H. Harding, Ann. Rev. Phys. Chem. 37, 53 (1986).
19. R. C. Baetzold, Surf. Sci. 150, 193 (1985);
P. G. Flahive and W. R. Graham, Surf. Sci. 91, 449 (1980);
J. R. Banavar, M. H. Cohen, and R. Gomer, Surf. Sci. 107, 113 (1981);
C. H. Mak and S. M. George, Chem. Phys. Lett. 135, 381 (1987).
20. M. Tringides, and R. Gomer, Surf. Sci. 145, 121 (1984);
D. A. Reed and G. Ehrlich, Surf. Sci. 120, 179 (1982);

D. A. Reed and G. Ehrlich, Surf. Sci. 105, 603 (1981);

T. T. Tsong, Surf. Sci. 122, 99 (1982).

21. J. C. Tully, G. H. Gilmer, and M. Shugard, J. Chem. Phys. 71, 1630 (1979);

G. De Lorenzi and G. Jacucci, Surf. Sci. 116, 391 (1982);

H. K. McDowell and J. D. Doll, Surf. Sci. 121, L537 (1982);

J. D. Doll and H. K. McDowell, Surf. Sci. 123, 99 (1982);

J. D. Doll and D. L. Freeman, Surf. Sci. 134, 769 (1983).

22. Y. R. Shen, The Principle of Nonlinear Optics (J. Wiley, New York) Chapter 25, p.479 - 504;

Y. R. Shen, Ann. Rev. Mat. Sci. 16, 69 (1986);

H. W. K.Tom, C. M. Mate, X. D. Zhu, J. E. Crowell, T. F. Heinz, G. A. Somorjai, and Y. R. Shen, Phys. Rev. Lett. 52, 348 (1984);

H. W. K. Tom, X. D. Zhu, Y. R. Shen, and G. A. Somorjai, Surf. Sci. 167, 167 (1986);

S. G. Grubb, A. M. DeSantolo, and R. B. Hall, J. Phys. Chem. 92, 1419 (1988).

23. Y. R. Shen, Nature 337, 519 (1989);

Y. R. Shen, "Optical Second-Harmonic Generation at surfaces", submitted to Ann. Rev. Phys. Chem..

24. X. D. Zhu, Y. R. Shen, and R. Carr, Surf. Sci. 163, 114 (1985).

25. K. Christmann, O. Schober, and G. Ertl, J. Chem. Phys. 60, 4719 (1974);

H. Conrad, G. Ertl, J. Kuppers, and E. E. Latta, Surf. Sci. 57, 475 (1976);

W. Erley, K. Besocke, and H. Wagner, J. Chem. Phys. 66, 5269 (1977);

F. P. Netzer and T. E. Madey, J. Chem. Phys. 76, 710 (1982), and references therein.

26. M. Trenary, K. J. Uram, and J. T. Yates, Jr., Surf. Sci. 157, 512 (1985);

W. Erley, H. Wagner, and H. Ibach, Surf. Sci. 80, 612 (9179).

27. P. A. Redhead, Vacuum 12, 203 (1962); D. A. King, Surf. Sci. 47, 384 (1975).

28. R. B. Hall, J. Phys. Chem. 91, 1007 (1987), and references therein.

29. J. Fujimoto, J. Liu, E. Ippen, and N. Bloenmbergen, Phys. Rev. Lett. 53, 1837 (1984);
H. W. K. Tom, G. D. Aumiller, C. H. Brito-Cruz, Phys. Rev. Lett. 60, 1438 (1988);
C. V. Shank, R. Yen, and C. Hirlimann, Phys. Rev. Lett. 51, 900 (1983);
J. Kash and J. C. Tsang, Phys. Rev. Lett. 54, 2151 (1985).

30. For optical properties of a Ni single crystal, we have used the updated results, n (λ = 1.064 μm) = 2.91 + i 5.24, published in Physics Data, Nr. 18-1. Optical Properties of Metals (Fach-informations-Zeutrum, Energie Physik Mathermatik GmbH, Karlsruhe, 1981) pp.95-108, eds. J. H. Weaver, C. Krafka, D. W. Lynch and E. E. Koch. We measured the reflectivity of the Ni and found it the same in the temperature range from room temperature to 1100 K over which the substantial desorption of CO takes place. For thermal properties of a Ni single crystal, we have adopted the values of heat capacity and thermal conductivity of Ni published in American Institute of Physics Handbook , 3rd ed., ed. D. Gray (McGraw-Hill, New York, 1972) pp.4-106, 4-154, and references therein.

31. J. H. Bechtel, J. Appl. Phys. 46, 1585 (1975).

32. X. D. Zhu, Th. Rasing, and Y. R. Shen, Chem. Phys. Lett. 155, 459 (1989).

33. J. B. Miller, H. R. Siddiqui, S. M. Gates, J. N. Russell, Jr., J. T. Yates, Jr., J. C. Tully, and M. J. Cardillo, J. Chem. Phys. 87, 6725 (1987).

34. H. J. Eichler, P. Gunter, and D. W. Pohl, Laser-Induced Dynamic Gratings (Springer-Verlag, Berlin, Heidelberg, 1986);
G. A. Reider, M. Huemer, and A. J. Schmidt, Opt. Commun. 68, 149 (1988);
T. F. Heinz and T. Suzuki, Bull. Am. Phys. Soc. 33, 387 (1988).

35. G. Doyen and G. Ertl, Surf. Sci. 43, 197 (1974).

36. M. Tringides and R. Gomer, Surf. Sci. 155, 254 (1985);
S. C. Wang and G. Ehrlich, Surf. Sci. 206, 451 (1988), and references therein;

D. Ghaleb and B. Perraillon, Surf. Sci. 162 (1985).

37. M. Blaszczyszyn, Surf. Sci. 136, 103 (1984);

J. C. Brand, A. A. Deckert, and S. M. George, Surf. Sci. 194, 457 (1988);

C. H. Mak, B. G. Koehler, J. C. Brand, and S. M. George, J. Chem. Phys. 87, 2340 (1987).

38. T. F. Heinz, C. K. Chen, D. Ricard, and Y. R. Shen, Phys. Rev. Lett. 48, 478 (1982);

X. D. Zhu, H. Suhr, and Y. R. Shen, Phys. Rev. B, Rapid Commun. 35, 3047 (1987);

J. H. Hunt, P. Guyot-Sionnest, and Y. R. Shen, Chem. Phys. Lett. 133, 189 (1987);

P. Guyot-Sionnest, J. H. Hunt, and Y. R. Shen, Phys. Rev. Lett. 59, 1597 (1987).

Figure Captions

Fig. 1(a) Schematic diagram of the experimental set-up for calibration of optical SHG with thermal desorption mass spectrometry. A Ni(111) sample is placed in the ultrahigh vacuum chamber which is equipped with usual surface analysis tools. The incident angles of the probe beams are at 45° off surface normal.

Fig. 1(b) Optical arrangement for probing of monolayer gratings of carbon monoxide (CO). The incident angle of the probe beam is at 71.4° off the surface normal to optimize the efficiency of SHG. The two interfering excitation beams for generating monolayer gratings are incident onto the sample situated in the ultrahigh vacuum chamber at $\phi_{inc} = \pm 1.50°$, respectively.

Fig. 2 Measured CO partial pressure change [panel (a)] and optical SHG signal strength panel (b)] as functions of the sample temperature in a thermal desorption of CO from Ni(111) at a heating rate of 2K/sec. Initially, coverage of CO θ is at θ_s = 0.5 and the sample is at 300 K. The probe beam is at wavelength λ_{exc} = 1.064 μm and an incident angle $\theta_{inc} = 45°$.

Fig. 3(a) Normalized SHG signal intensity vs. normalized coverage of CO on Ni(111), θ / θ_s. The solid line is a least-square fit to the experimental result assuming SHG = constant $\times$ $| A + B\theta |^2$. The fitting yields B/A = 0.9 exp(i165°).

Fig. 3(b) Normalized SHG signal intensity vs. the CO exposure, L, to Ni(111) in an adsorption isotherm measurement.

Fig. 3(c) Adsorption isotherm of CO on Ni(111) (coverage θ vs. exposure L), deduced from the results shown in Fig. 3(a) and Fig. 3(b). The solid line is a theoretical least-square fit to the experimental result assuming that CO adsorption follows simple Langmuir kinetics, $\theta(L) = \theta_s[1 - \exp(- s_0\Gamma L / N_s\theta_s p)]$. The fitting yields an initial sticking probability $s_0 = 0.81$.

Fig. 4(a) Normalized SHG signal intensity vs. the CO exposure. The probe beam is at

wavelength $\lambda_{exc} = 0.532$ μm and an incident angle of 45°.

Fig. 4(b) Normalized SHG signal intensity vs. the normalized coverage of CO, deduced from the results shown in Fig. 3(c) and Fig. 4(a). The solid line is a least-square fit assuming that SHG = constant × $|A + B\theta|^2$. The fitting yields B/A = − 0.6.

Fig. 4(c) Normalized SHG signal intensity vs. the normalized coverage of CO. The probe beam is at 0.532 μm and an incident angle of 71.4°. The solid line is a least-square fit assuming that SHG = constant × $|A + B\theta|^2$. The fitting yields B/A = − 0.68.

Fig. 5 Schematic diagram of the optical arrangement for laser-induced desorption yield measurement. The excitation beam at 1.064 μm and the probe beam at 0.532 μm are collinearly aligned and the centers of the two beams are overlapped on the sample. The ratio of the cross-sections of the two beams is 30.

Fig. 6 CO coverage change vs. absorbed laser fluence in the laser-induced desorption measurement. $\Delta\theta$ is deduced from the change of the *in situ* SHG signal from the center of the desorption area. The solid line is calculated using a thermal desorption model assuming a preexponential factor $\nu = 0.91(k_BT/h)\theta$ and a desorption activation energy $E_d = E_d(\theta) - 3RT/2$ taken from Ref. [25].

Fig. 7 The surface temperature rise and the rate of a molecular thermal desorption with time during the irradiation of a metal surface by a nanosecond laser pulse (τ_p). The molecular desorption energy E_d is chosen 26 kcal/mol and the preexponential factor $\nu = 10^{13}$ /sec. Due to the nature of an activated reaction, the yield of the laser-induced desorption is most significant in a time window with a width close to τ_p.

Fig. 8 Calculated groove structure in one spatial period (2a) of the monolayer grating at various distances from the co-center of the desorption beams on the surface: (a) $r/r_0 = 0$; (b) $r/r_0 = 0.1$; (c) $r/r_0 = 0.2$; (d) $r/r_0 = 0.3$; (e) $r/r_0 = 0.4$; (f) $r/r_0 = 0.5$. Here, r_0 is the e^{-1} radius of the Gaussian desorption beam.

Fig. 9 Numerically calculated spatial Fourier components (n = 0, 1, 2, 3, 4) of the monolayer grating as shown in Fig. 8 at various distances r from the co-center of the desorption beams.

Fig. 10 Measured (unshaded) and calculated (shaded) square roots of second-harmonic diffraction signals of various orders from the monolayer grating of CO on Ni(111). The signals are normalized to that of the specularly reflected (i. e., zero-th order) SHG.

Fig. 11 Normalized first-order second-harmonic diffraction signal as a function of time at various sample temperatures after the generation of the monolayer grating of CO on Ni(111) by laser desorption. Solid circles: T = 219 K; open triangles: T = 247 K; solid squares: T = 261 K; open circles: T = 273 K. The solid curves are least-square fits using single-exponential functions with the exponent $\alpha(T) = 2\pi^2 D(T)/ a^2$ as the adjustable parameter.

Fig. 12 The Arrhenius plot (open circles) of the diffusion constant $D(T)$ obtained from the results of Fig. 11. Least-square fitting to a linear function (solid line) of $1/T$ yields a diffusion activation energy $E_{diff} = 6.9 \pm 1.0$ kcal/mol, and a preexponential factor $D_0 = 1.2 \times 10^{-5}$ cm^2/sec [or $\ln(D_0) = -11.4 \pm 2.0$].

Fig. 13 Possible hopping route for CO on Ni(111). The surface potential energy diagram joining a bridge-site and an on-top site is constructed from the previous measurements of adsorption, desorption and vibrational spectroscopy of CO on Ni(111). The measured diffusion activation energy Ediff = 6.9 ± 1.0 kcal/mol is found close to the energy barrier for a bridge-bonded CO to a neighboring on-top site, indicating hopping from a bridge site to another bridge site through an intermediate on-top site is a likely route of the diffusion.

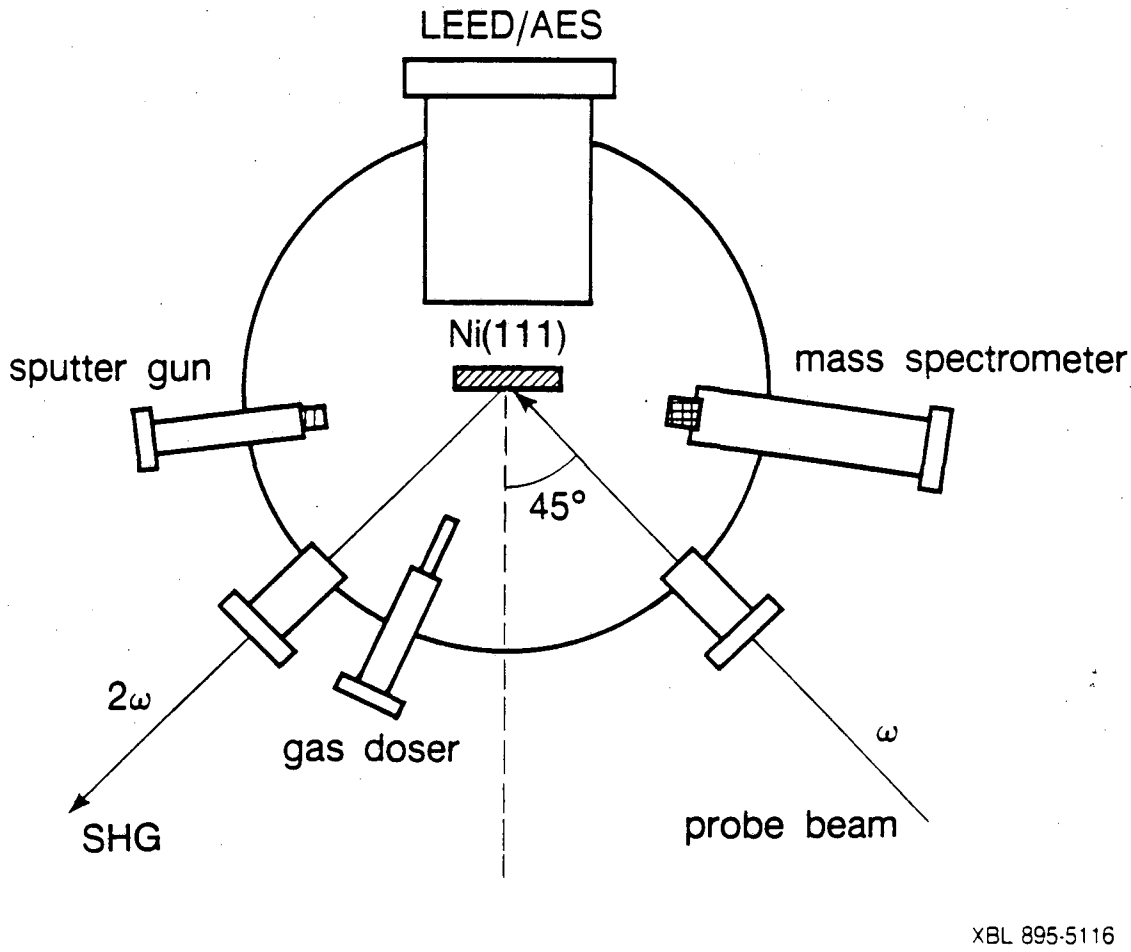
LEED/AES
Ni(111)
sputter gun
mass spectrometer
45°
2ω
gas doser
ω
SHG
probe beam
XBL 895-5116

Fig. 1(a)

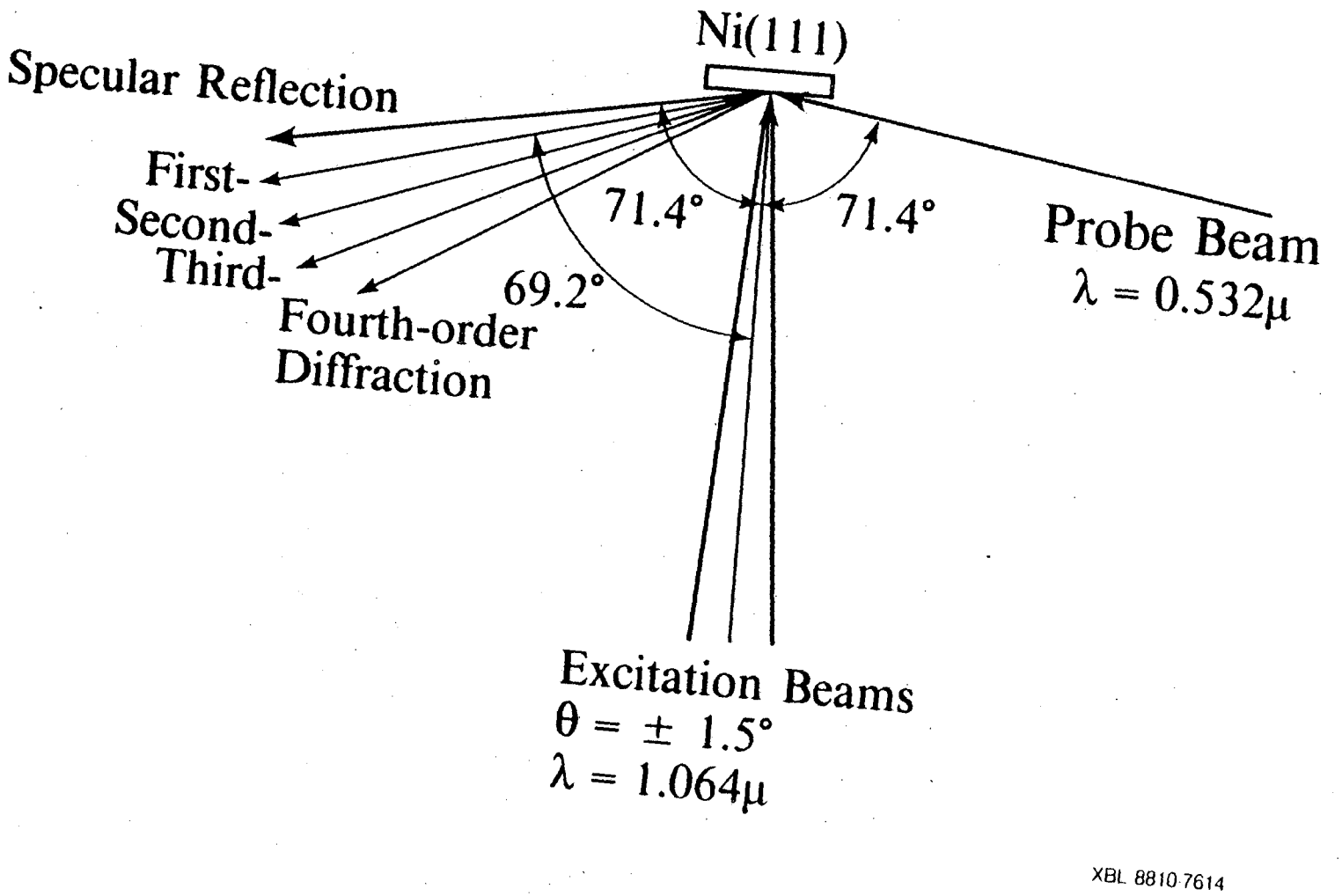
Ni(111)
Specular Reflection
First-
Second-
Third-
Fourth-order
Diffraction
69.2°
71.4°
71.4°
Probe Beam
λ = 0.532μ
Excitation Beams
θ = ± 1.5°
λ = 1.064μ
XBL 8810-7614

Fig. 1(b)

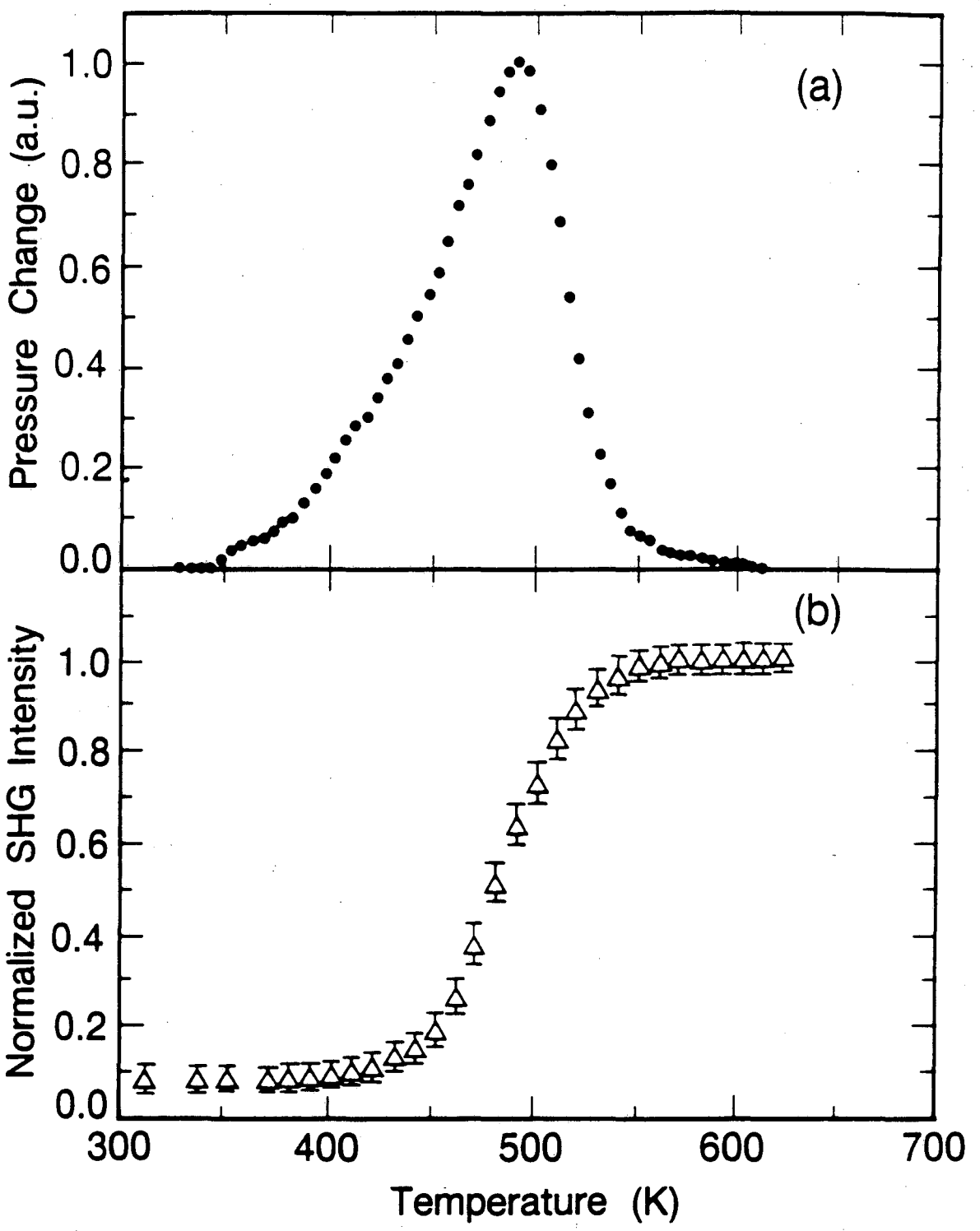

XBL 895-5119A

Fig. 2

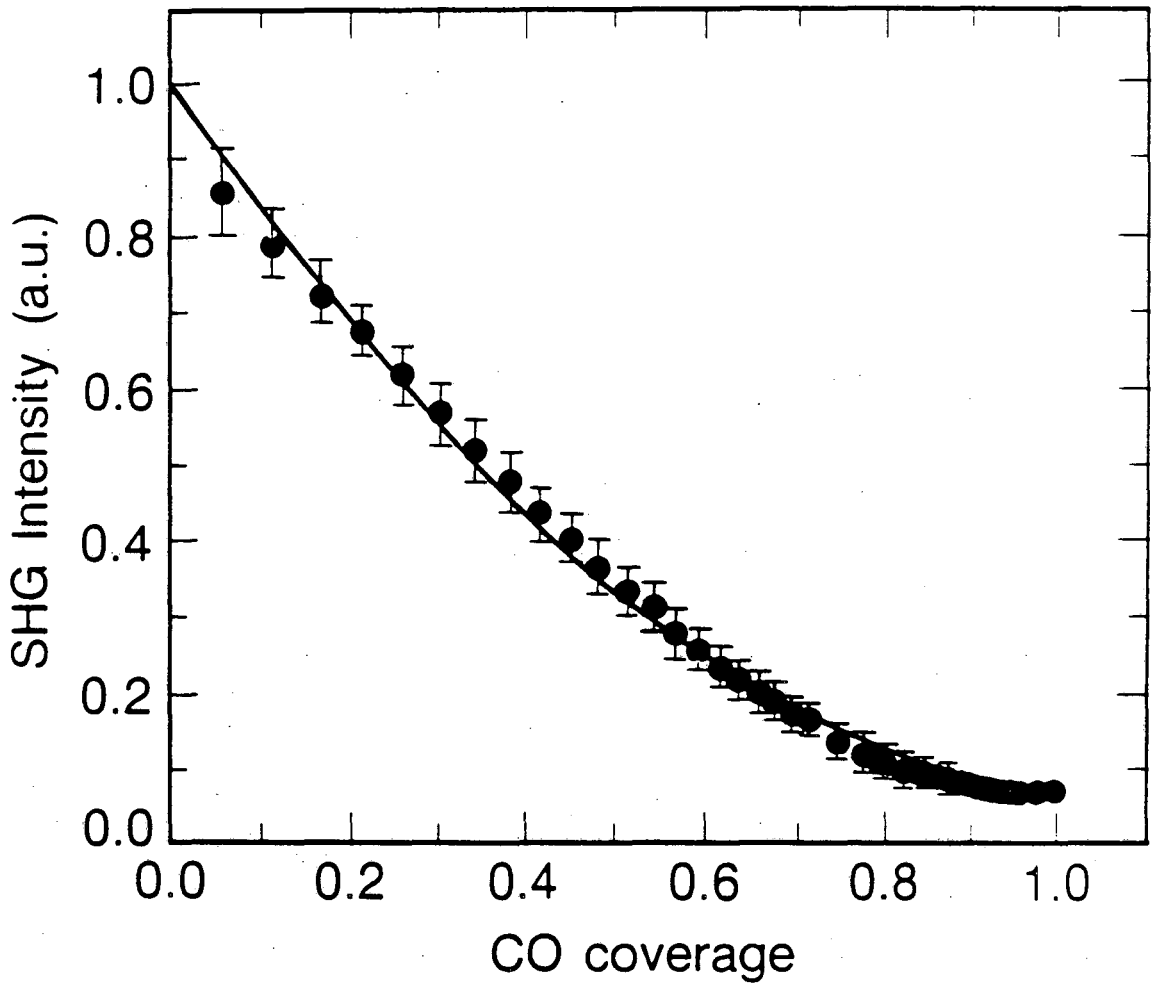

XBL 893-5049

Fig. 3(a)

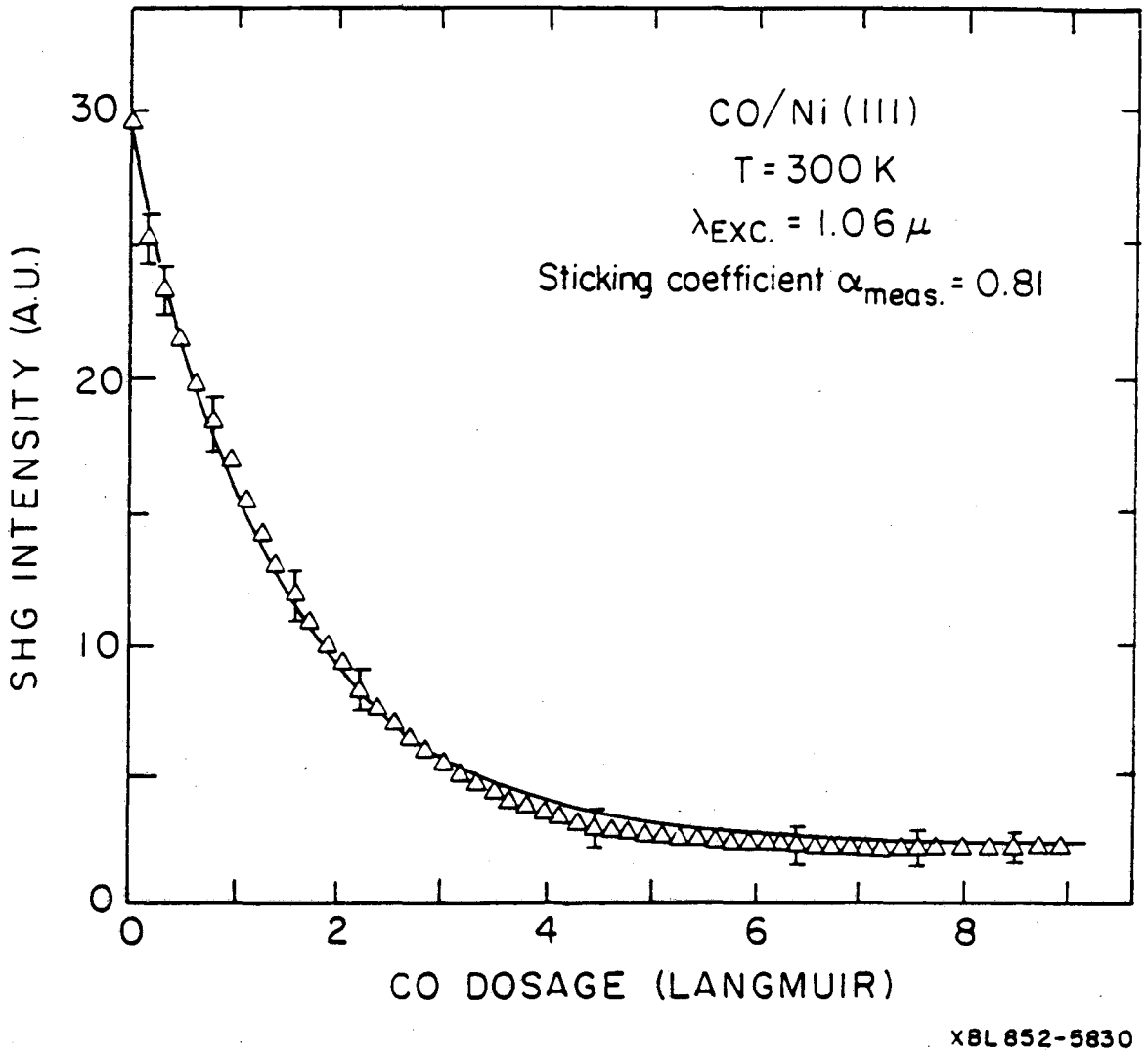
CO/Ni (111)
T = 300 K
λEXC. = 1.06 μ
Sticking coefficient αmeas. = 0.81
SHG INTENSITY (A.U.)
30
20
10
0
0
2
4
6
8
CO DOSAGE (LANGMUIR)
XBL 852-5830

Fig. 3(b)

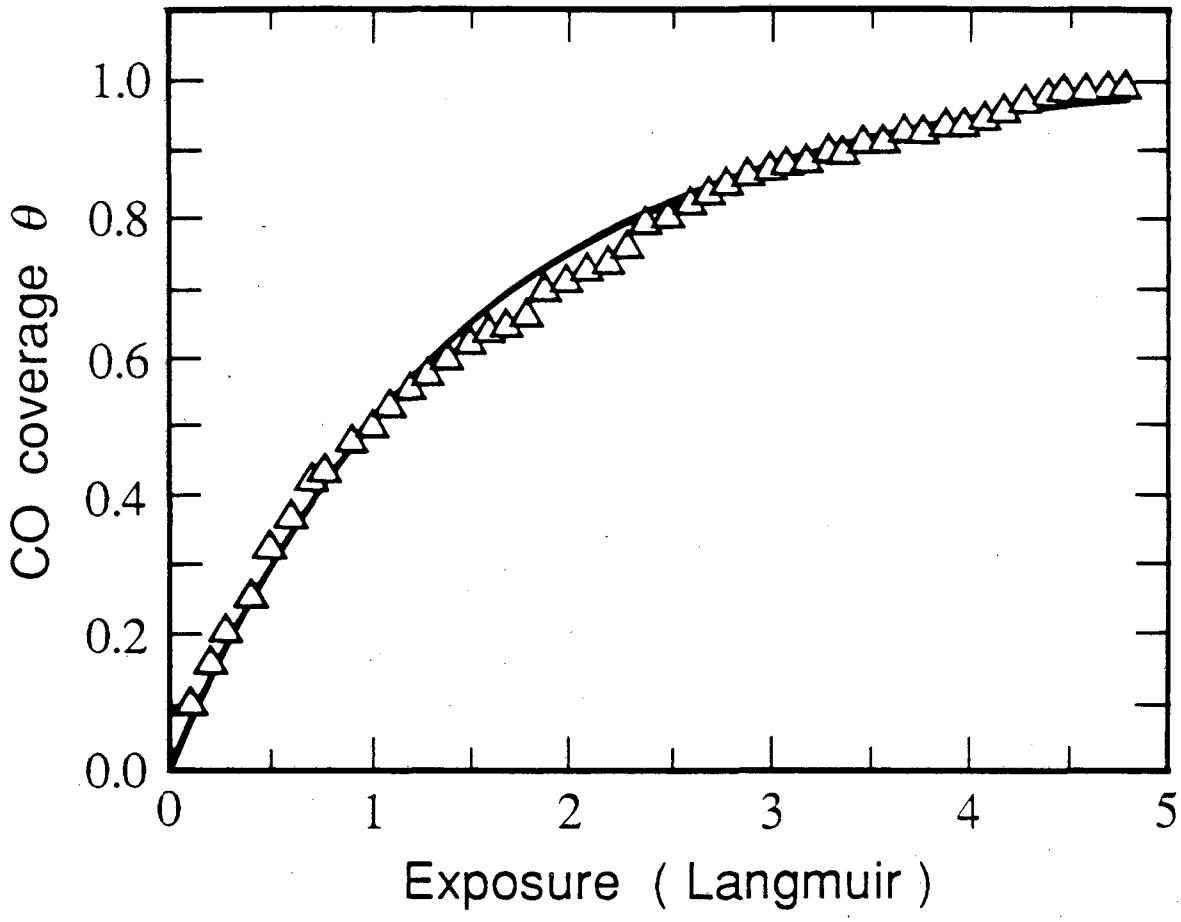

XBL 897-5156

Fig. 3(c)

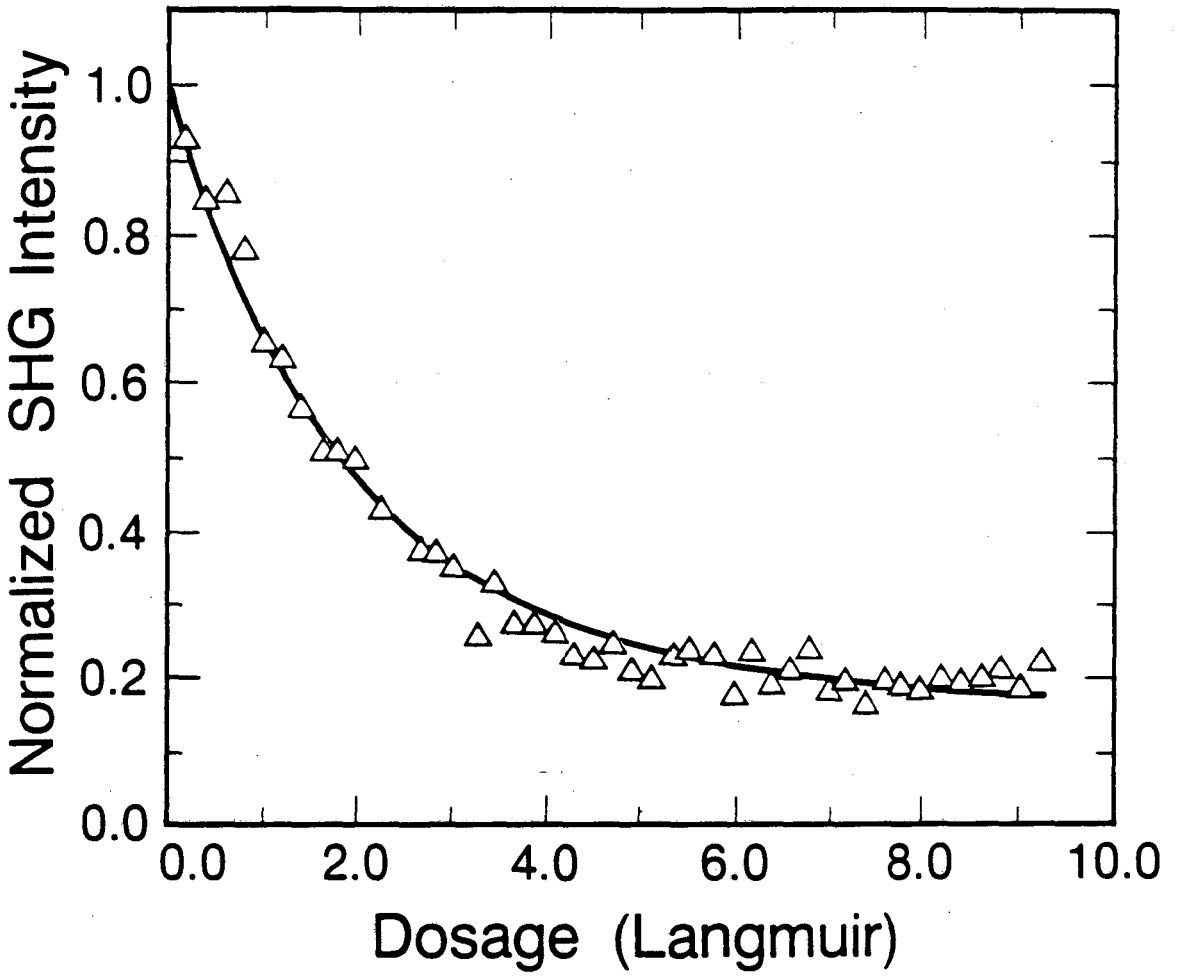

XBL 895-5114

Fig. 4(a)

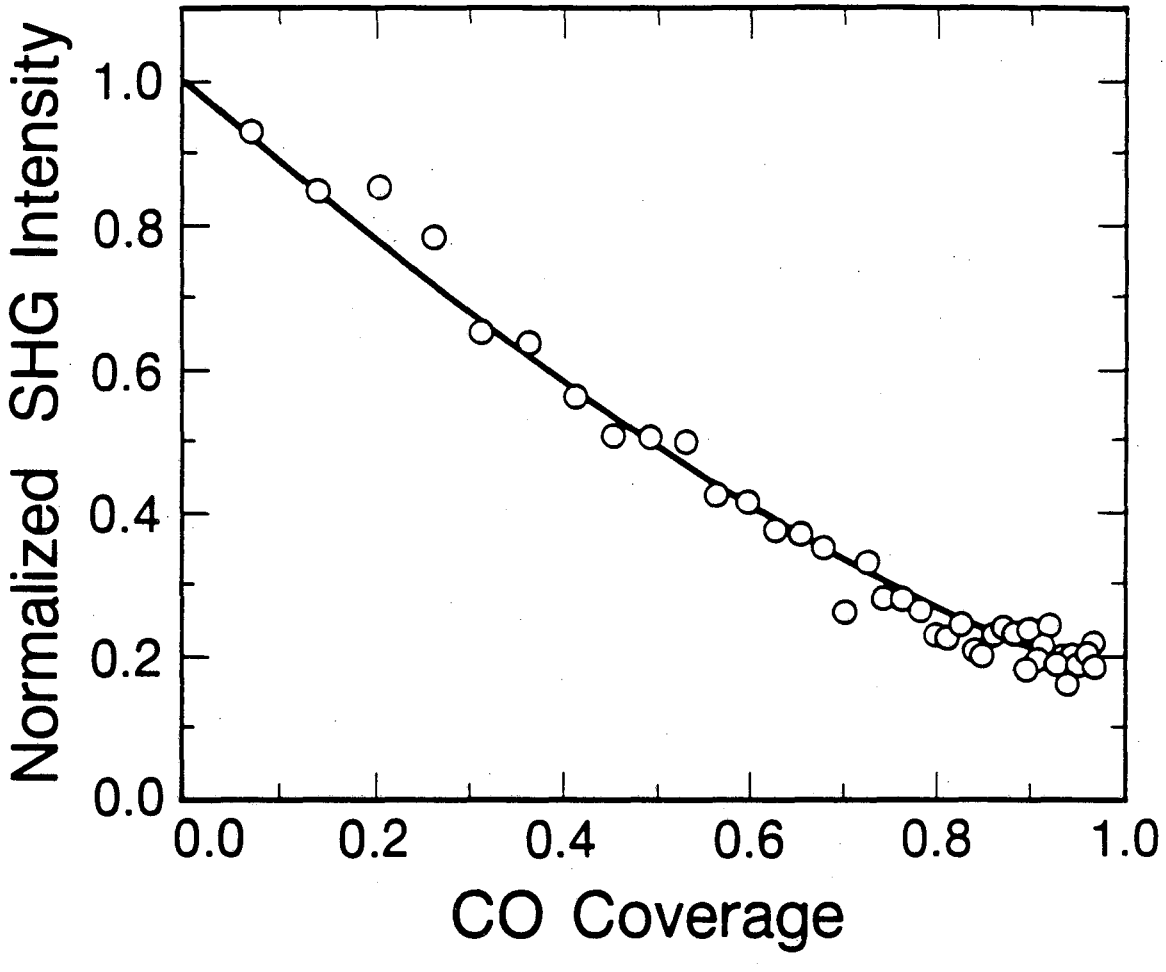

XBL 895-5115

Fig. 4(b)

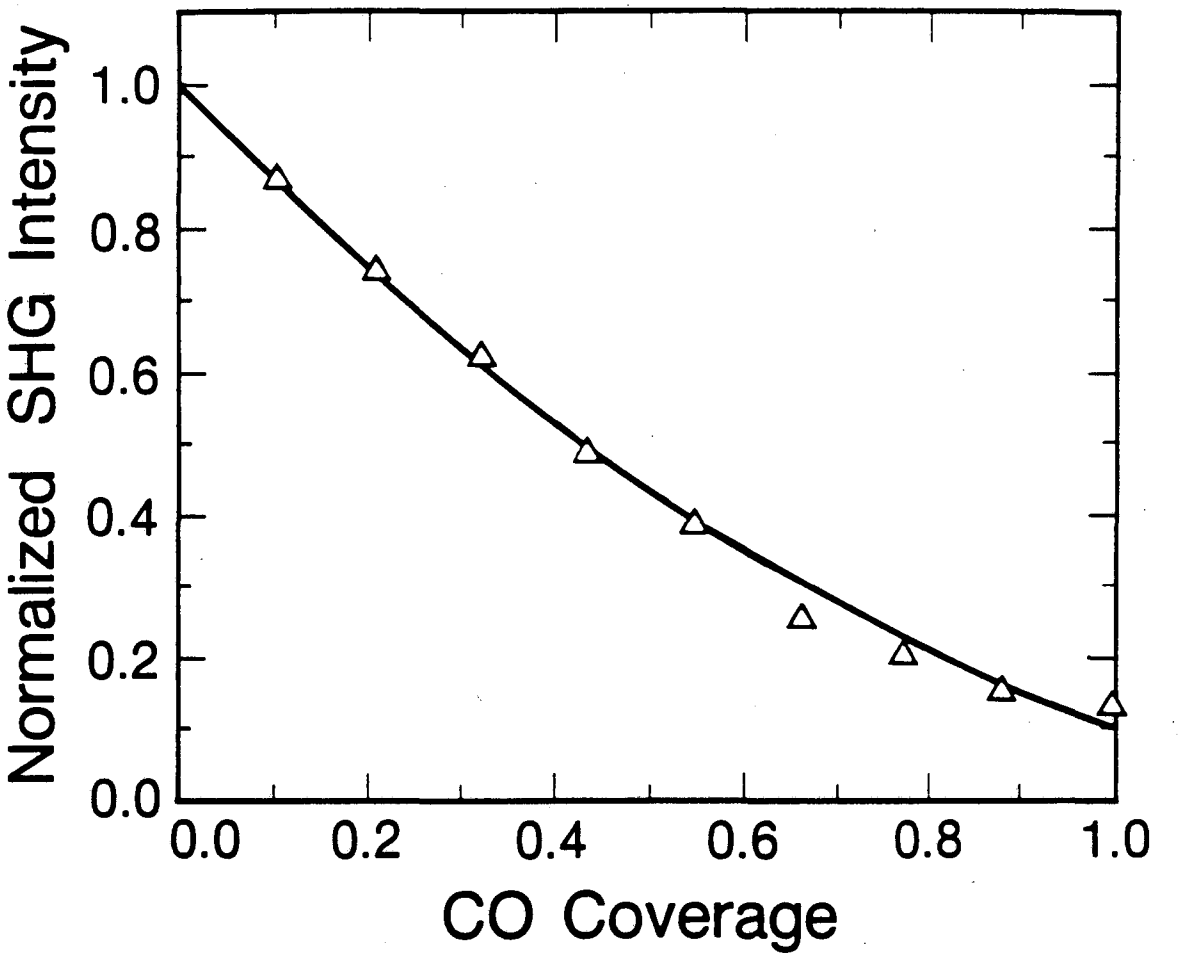

XBL 895-5115A

Fig. 4(c)

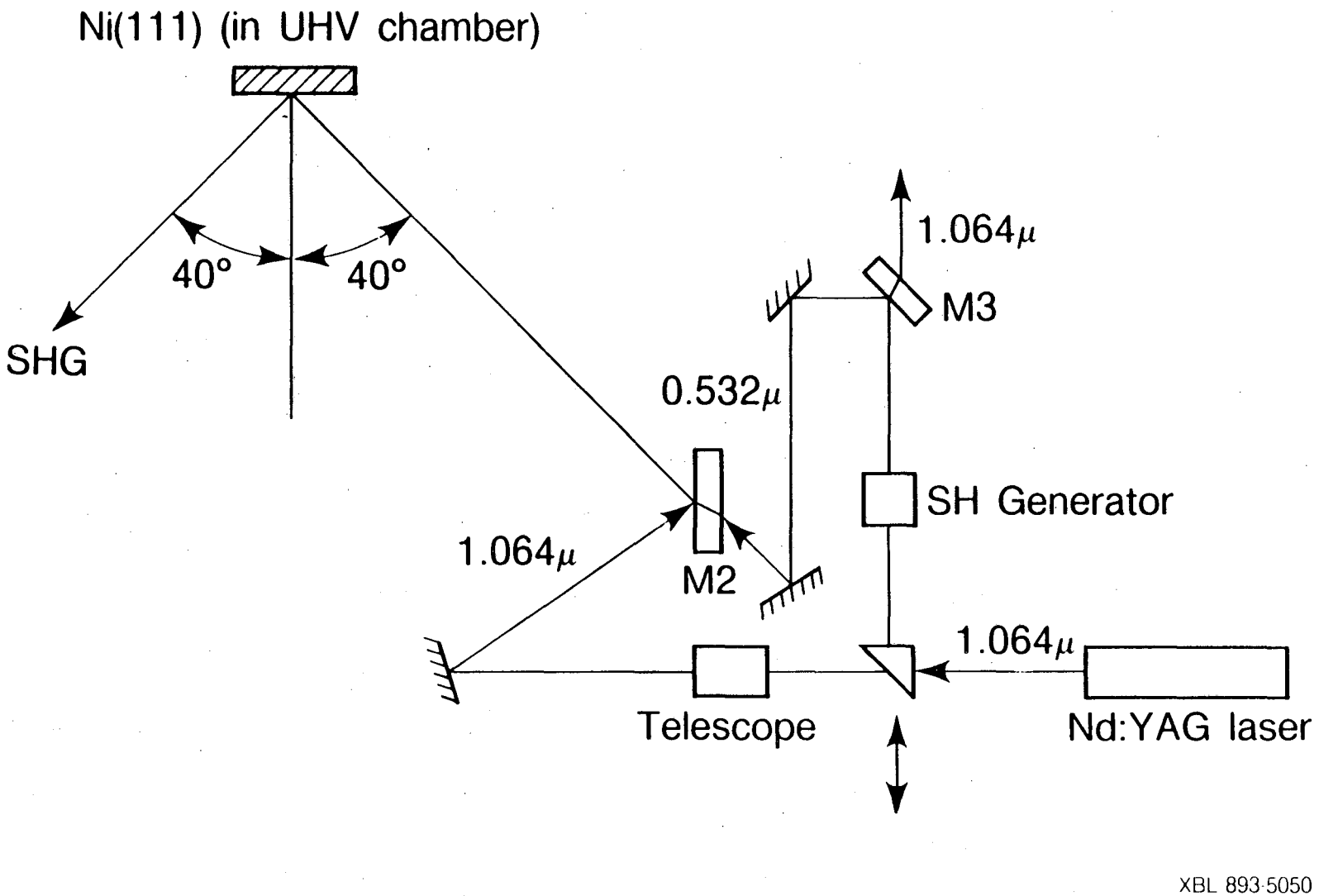
Ni(111) (in UHV chamber)
40°
40°
SHG
1.064μ
M3
0.532μ
SH Generator
1.064μ
M2
1.064μ
Telescope
Nd:YAG laser
XBL 893-5050

Fig. 5

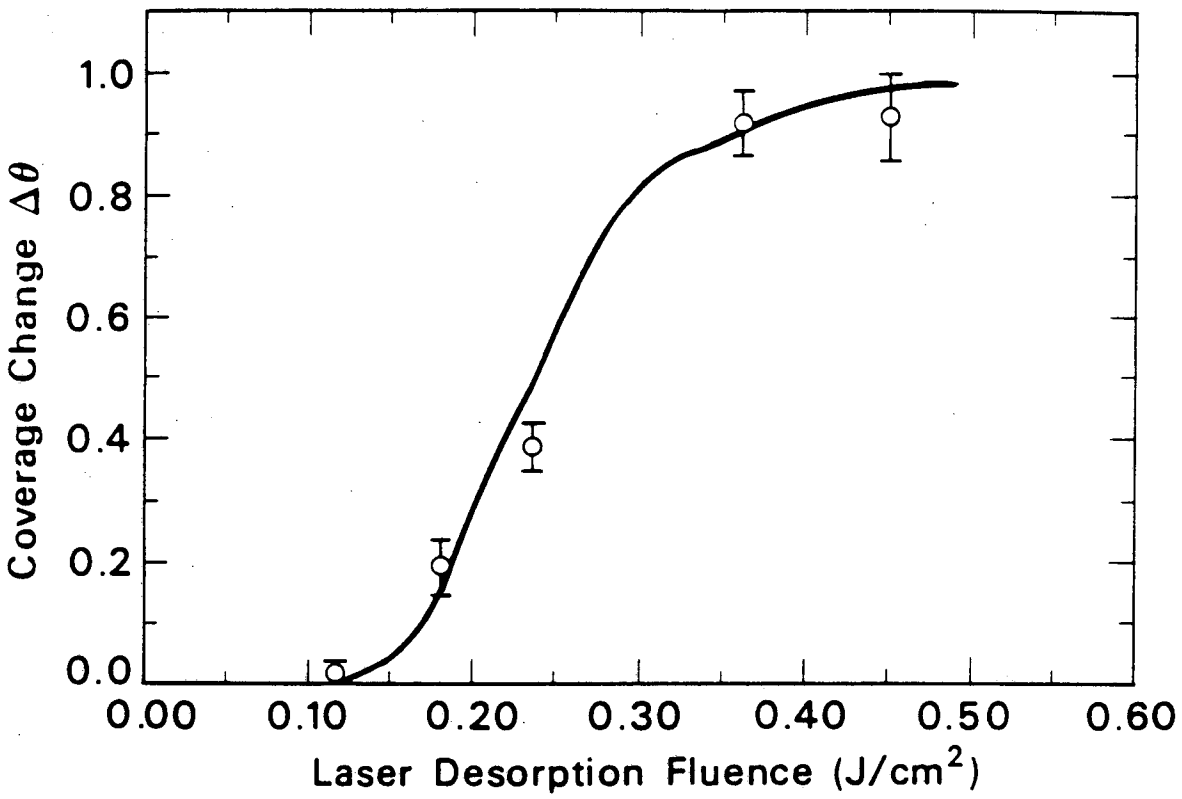

XBL 883-7319A

Fig. 6

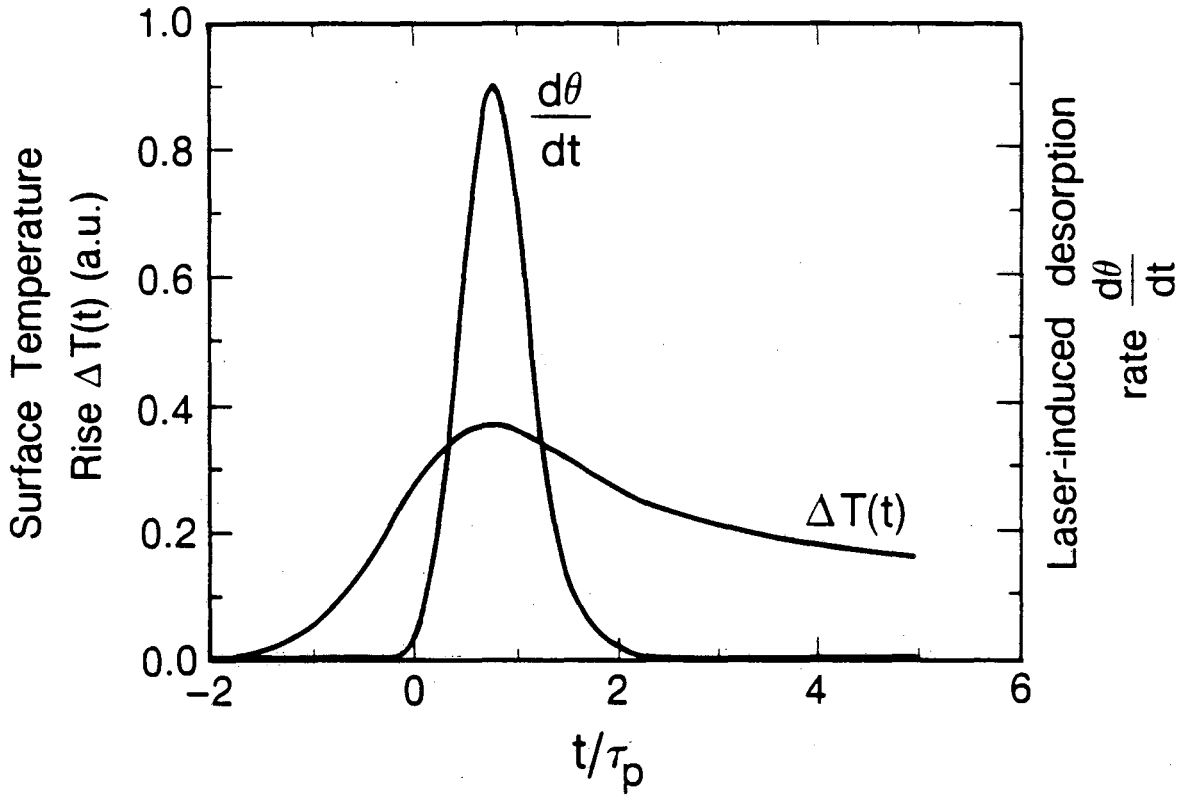

XBL 895-5112

Fig. 7

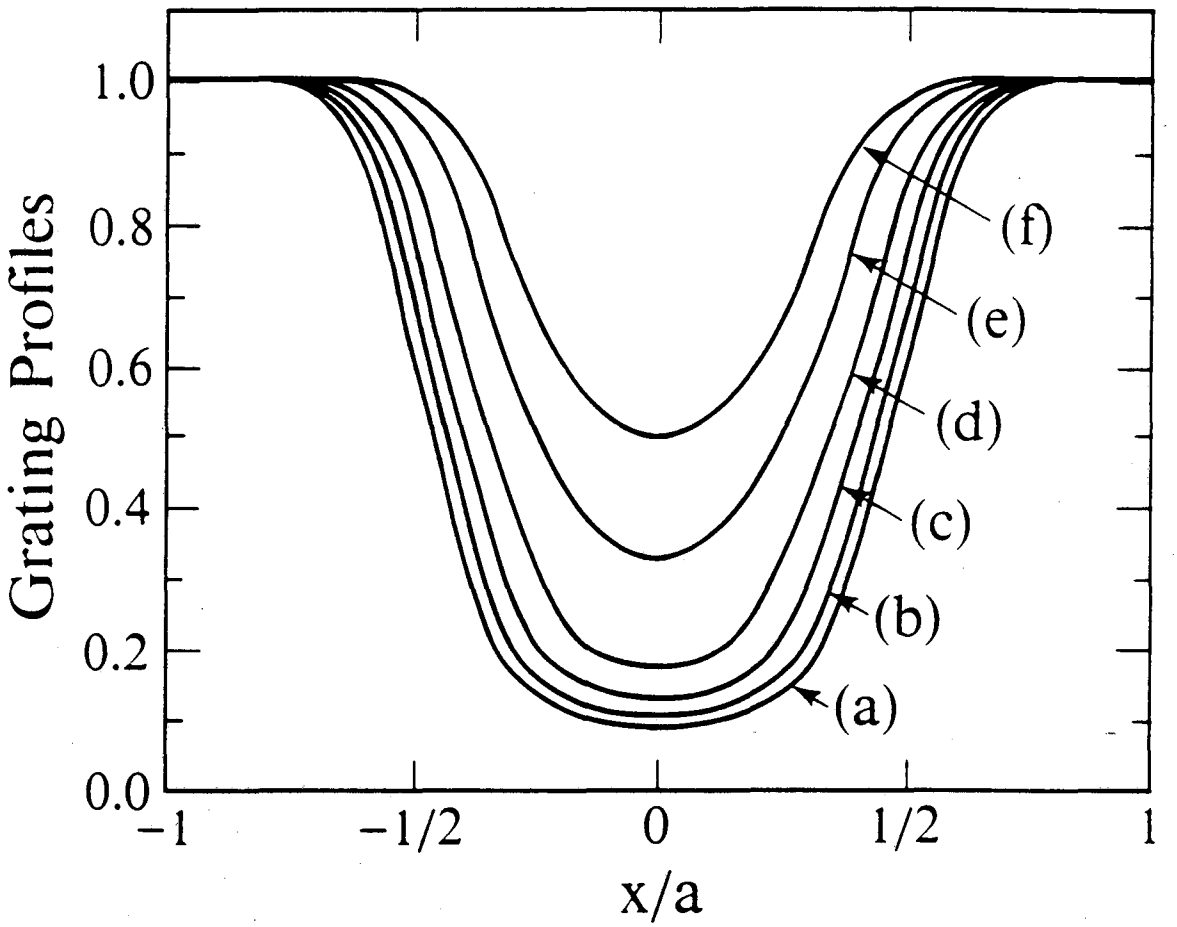

XBL 8810-7613

Fig. 8

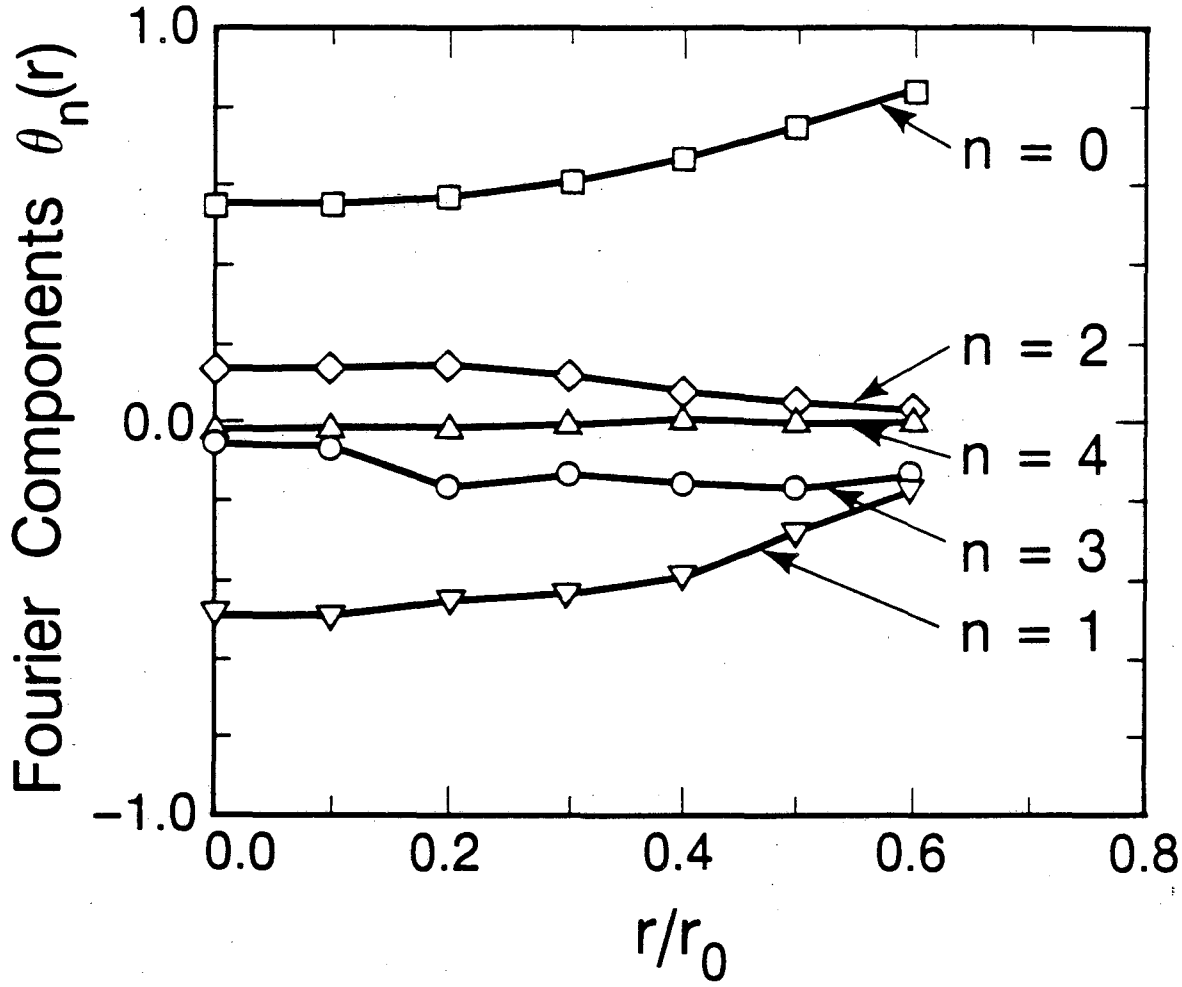

XBL 895-5113

Fig. 9

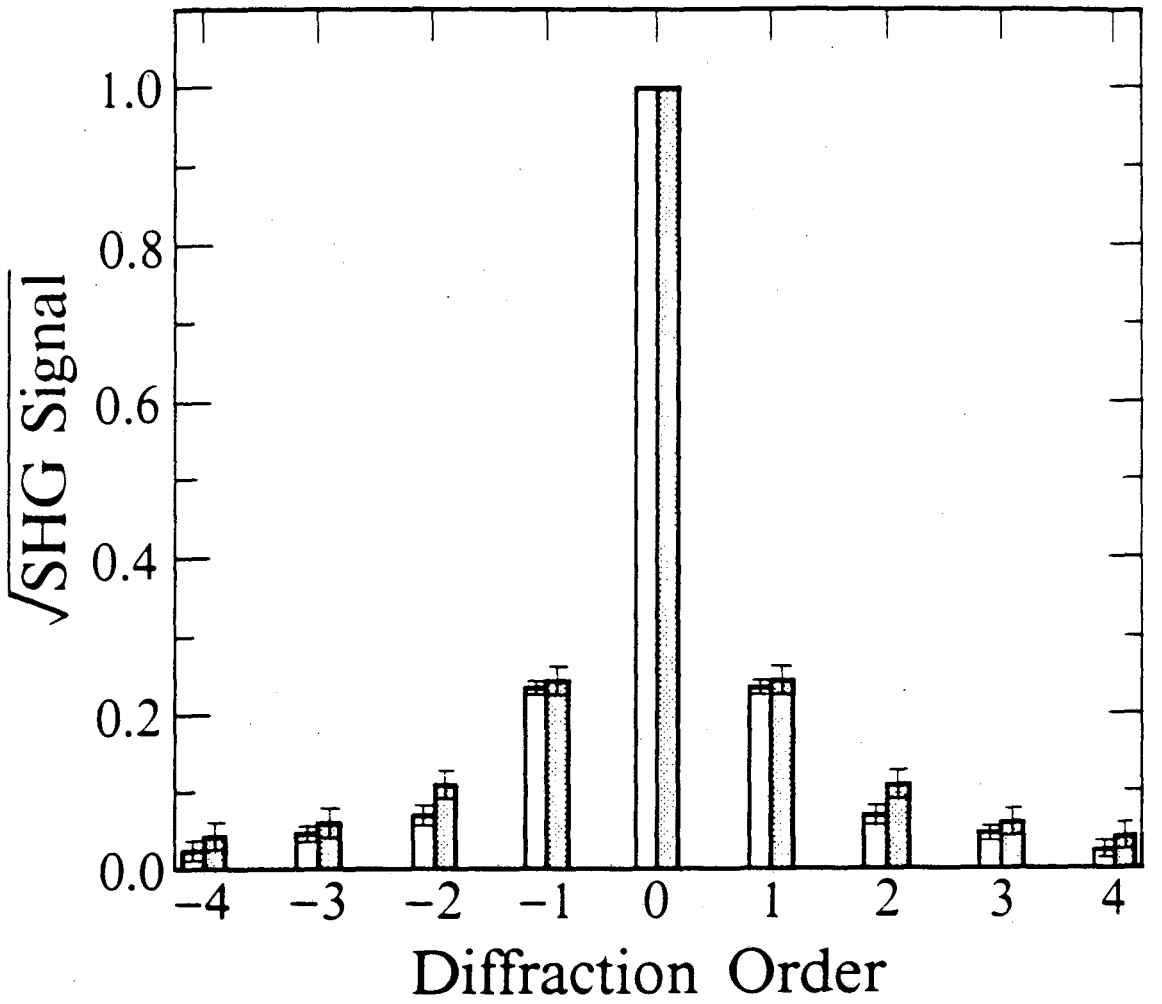

XBL 8810-7615

Fig. 10

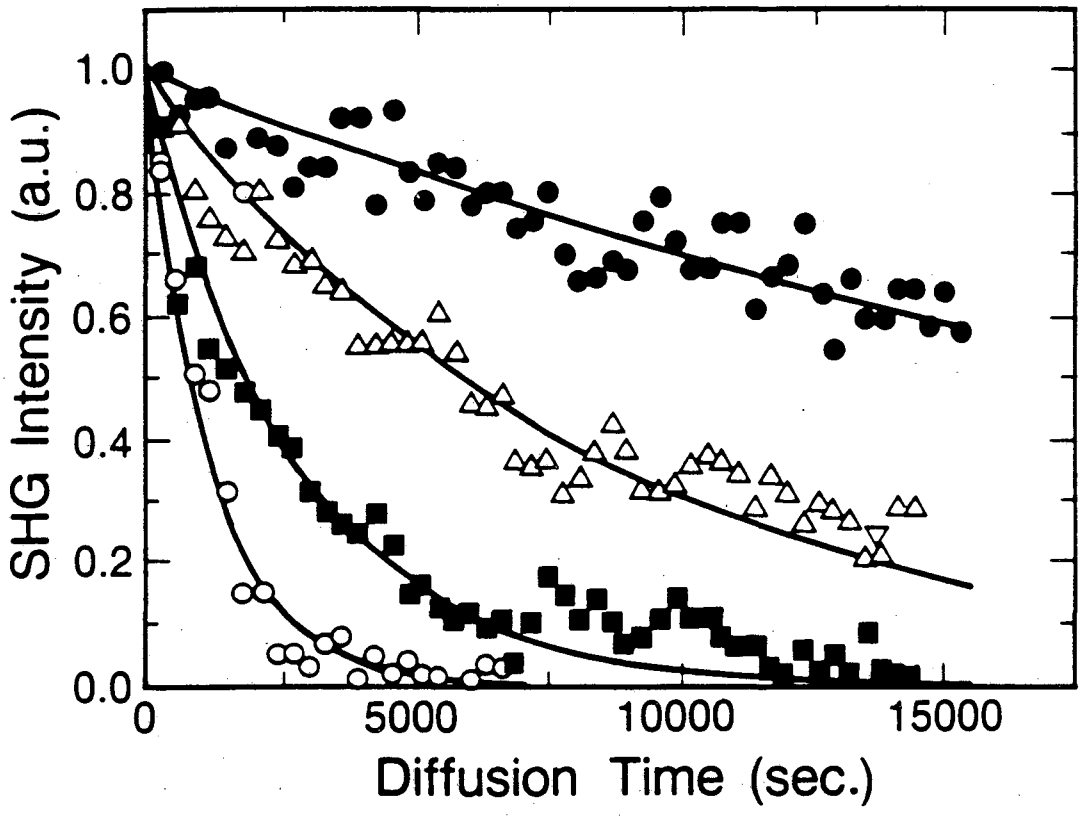

XBL 887-7488

Fig. 11

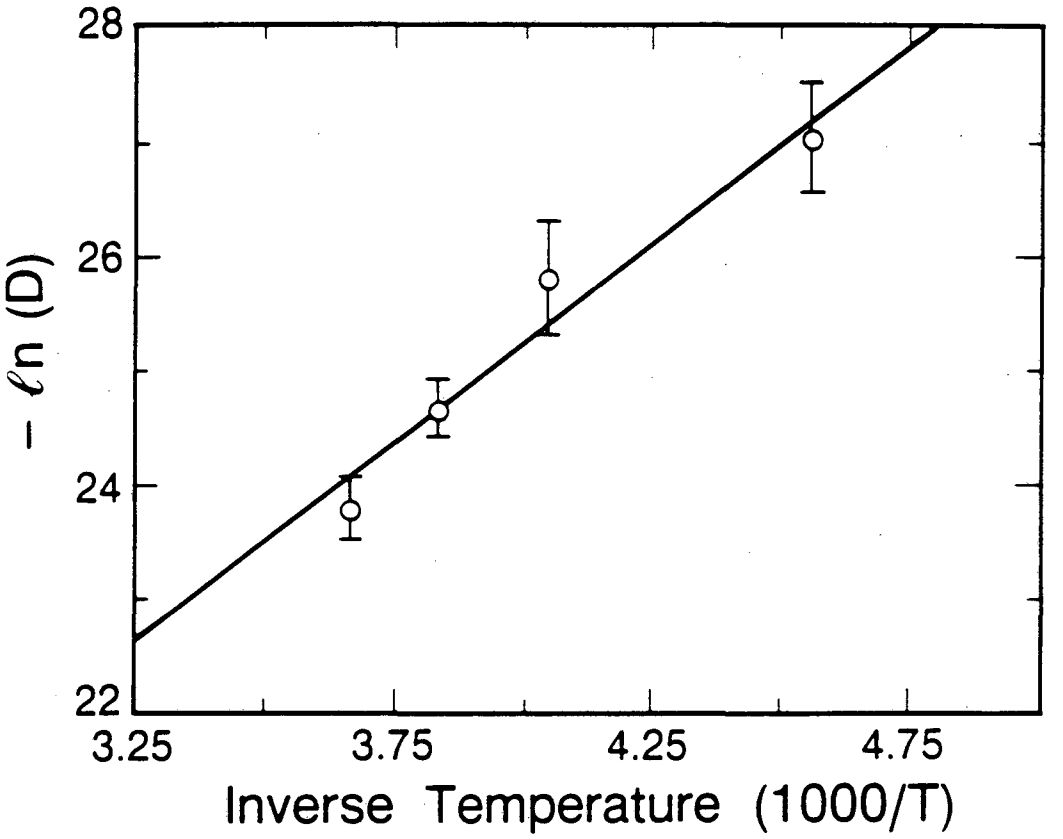

XBL 887-7487

Fig. 12

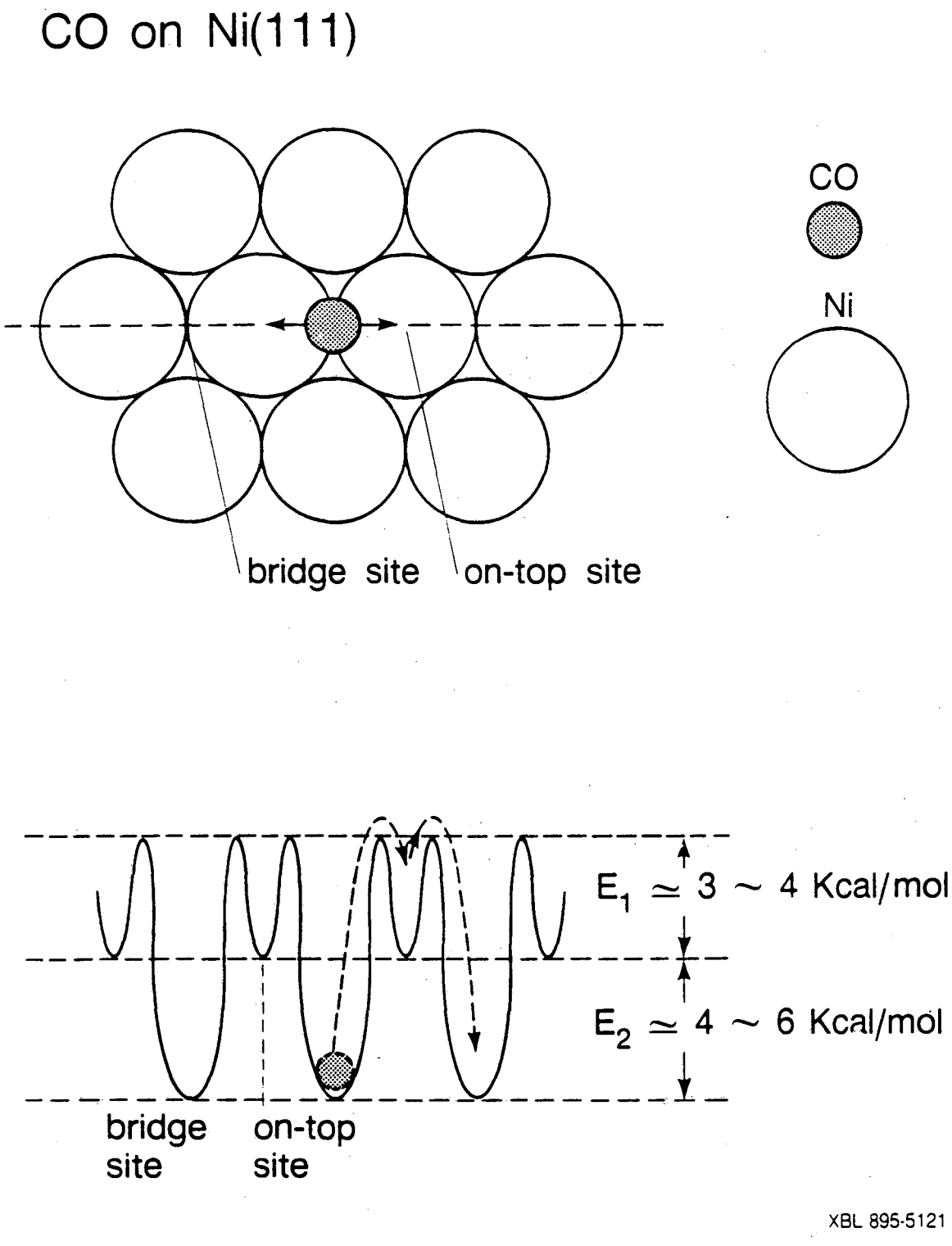
CO on Ni(111)
CO
Ni
bridge site
on-top site
$E_1 \simeq 3 \sim 4$ Kcal/mol
$E_2 \simeq 4 \sim 6$ Kcal/mol
bridge site
on-top site
XBL 895-5121

Fig. 13

III. Surface Vibrational Spectroscopy by Infrared-visible Sum-Frequency Generation

A. Introduction

Surface vibrational spectroscopy plays an indispensable role in modern surface science and material science research.[1] Apart from the fundamentally interesting applications to studies of forces and structural properties within surfaces, it is routinely used to identify adsorbed species and their structural configurations on surfaces.[1 - 4] As the spectral lineshape and spectral frequency shift of a vibrational mode change with the adsorbate-adsorbate and adsorbate-substrate interactions, these spectroscopic studies help us to understand the fundamentals of gas-solid interactions which have wide applications in a number of important areas of technology such as catalytic reactions, growths of amorphous and crystalline materials and material processing.[5] The rates and pathways of vibrational energy and phase relaxations on surfaces are closely related to the detail characteristics of the forces exercised on an adsorbate and they play crucial roles in the dynamics of surface reactions, surface diffusions and many other processes which occur on a surface.

Quite a number of vibrational spectroscopic techniques for probing surfaces have been developed.[1, 2, 6 - 9] Most of these techniques such as high resolution electron energy loss spectroscopy (HREELS), inelastic electron tunneling spectroscopy (IETS), low energy helium scattering, infrared reflection-absorption spectroscopy (IRAS), Fourier transform infrared spectroscopy (FTIR),[6] photoacoustic spectroscopy (PAS)[7, 8] and infrared emission spectroscopy [9] are often limited to measurements in the frequency domain. They are most suitable for studies of the equilibrium properties such as

identification of adsorbed species, binding geometry, bond-weakening or strengthening, and collective motions and force fields in overlayer superlattices. Generally speaking, these techniques are not adequate for studies of ultrafast vibrational transients and relaxations. This is derived from the fact that many competing transient processes and inhomogeneous spectral broadening can all contribute to the experimentally measured vibrational spectral lineshape, and their relative importance and the mechanisms which govern these processes are difficult to resolve simply through lineshape analysis.[4, 10, 11] Only on special occasions can some conclusions be drawn on the nature of ultrafast vibrational relaxations from these frequency domain measurements. Transient spectroscopic techniques which are capable of separately probing different transient processes are clearly desirable. For this purpose, Raman gain and transient infrared population saturation spectroscopies have been attempted.[12, 13] However, adequate sensitivity and surface specificity of these techniques to study adsorbates on well-defined single crystalline surfaces have not yet been demonstrated. From the viewpoint of versatility of an interface vibrational spectroscopic probe, many of these techniques involving scattering or emission of electrons or massive particles are extremely surface specific, but at the same time, are only applicable to vacuum-solid interfaces due to the limited mean free-paths of these particles. Others involving linear optical absorption and reflection or Raman scattering are generally lack of surface specificity; therefore, elaborate background discrimination schemes have to be used to extract surface spectroscopic information. One of the successful examples is Fourier Transform Infrared Spectroscopy (FTIR) which has been developed into a standard surface vibrational spectroscopic probe with adequate sensitivity and unsurpassed frequency resolution.[6]

We have developed a new technique using infrared-visible sum-frequency generation from a surface.[14] As a second-order nonlinear optical process, this technique is intrinsically surface specific.[15] Being optical, it can probe any interfaces accessible by light. Most importantly, it has the capability to separately probe vibrational transients on a

surface. In the past few years, coherent optical second-harmonic generation (SHG) have been demonstrated and applied as an effective surface probe.[15] As we have discussed in the general introduction, its effectiveness is derived from the intrinsic surface specificity of a coherent second-order nonlinear optical process. The capability of SHG for studies of ultrafast dynamics on surfaces have also been demonstrated elegantly.[16] Presumably, resonant SHG pumped with coherent infrared light sources should allow us to study vibrational spectroscopy on a surface.[17] However, even with the state-of-the-art infrared detectors commercially available today, the detection quantum efficiencies ($\leq 10^{-5}$) in the infrared frequency range suitable for surface vibrational excitations are two to three orders of magnitude lower than those in the visible or near ultra-violet frequency range.[9, 18] Since the SHG signals are generally expected in the range of 10^2 to 10^5 photons/sec, SHG in the infrared frequency range is not adequate for studies of surface vibrations.[15] On the other hand, one can extend SHG to sum-frequency generation. If one of the optical waves is in the infrared in resonance with a vibrational resonance and the other in the visible, then the resonance enhancement in the output of the sum-frequency wave-mixing will enable us to probe the vibrational resonance.[14, 19, 20] In this way, the vibrational excitation is up-converted to the visible or near UV frequency range over which well-developed photon-counting detection schemes with quantum efficiencies as high as 10^{-2} can be used. In this chapter, we describe the principle of the technique and its intimate relation with more familiar linear absorption spectroscopy and Raman scattering spectroscopy. We then present the first vibrational spectrum of a monolayer of adsorbates, coumarin 504 dye molecules on fused silica using optical sum-frequency generation (SFG) pumped with a tunable infrared laser beam and a visible laser beam.[14] The results compare well with the theoretical prediction. As an optical probe, coherent sum-frequency generation (SFG) intrinsically has high frequency and time resolutions. Being a second-order optical process as opposed to coherent Raman scattering which is a third-order optical wave mixing process, we expect a much larger SFG response from a surface layer without special

enhancement mechanisms.[15, 21] Moreover, SFG can be readily extended to transient spectroscopy for studies of dynamics of vibrational relaxation processes on surfaces.[20] Our results indicate clearly such possibility and practicality. Extensions to studies of molecular orientation and selective monitoring of transient reactions are discussed. Applications to investigation of ultrafast vibrational relaxations on surfaces are also explored. More detailed exploration will be presented in the next chapter.

B. Theoretical description

1. *Molecular nonlinear susceptibility at sum-frequency*

Although the following description applies to all forms of surface resonances including vibrational resonances, we will focus our discussion on vibrational excitations of adsorbates on surfaces. Due to the asymmetry of the atomic arrangement and the resultant forces at an interface adjoining two different media, adsorbed molecules often form a noncentrosymmetric layer. In the presence of two optical fields, $\mathbf{E}(\omega_1, t) = \mathbf{E}(\omega_1) \exp(-i\omega_1 t) + \mathbf{E}^*(\omega_1) \exp(i\omega_1 t)$ and $\mathbf{E}(\omega_2, t) = \mathbf{E}(\omega_2) \exp(-i\omega_2 t) + \mathbf{E}^*(\omega_2) \exp(i\omega_2 t)$, an electric-dipole polarization which oscillates at the sum-frequency $\omega_3 = \omega_1 + \omega_2$ can be generated within the layer [15]

$$\mathbf{P}(\omega_3) = \overleftrightarrow{\chi}^{(2)}(\omega_3) : \mathbf{E}(\omega_1)\, \mathbf{E}(\omega_2)\, \delta(z) , \qquad (1)$$

where $\chi^{(2)}(\omega_3)$ is the surface susceptibility tensor at sum-frequency ω_3, and we define the plane of the surface as $z = 0$. Since the nonlinear dipole layer is confined in z-direction with a thickness much smaller than the excitation wavelengths, for the optical sum-frequency generation, we can treat the density distribution of the nonlinear dipole moment

in the z-direction by a delta function $\delta(z)$. There should also be an induced polarization which oscillates at the difference frequency $\omega_3' = \omega_1 - \omega_2$

$$\mathbf{P}(\omega_3') = \overleftrightarrow{\chi}(\omega_3') : \mathbf{E}(\omega_1)\, \mathbf{E}^*(\omega_2)\, \delta(z)\,, \tag{2}$$

Eq. (1) and (2) are the radiation source terms for the sum-frequency generation (SFG) and difference frequency generation (DFG) from the adsorbate layer. In general, the nonlinear response from the bulk of the substrate is also expected to contribute to SFG. For centrosymmetric or isotropic media, the bulk contribution is derived from the electric quadruple and magnetic dipole responses of the material to the driving electromagnetic fields. Due to lack of resonance, they are generally comparable or small compared to the signal from the surface layer. In our case for example, the fused silica substrate generates little SFG compared to that from a monolayer of coumarin 504 dye molecules. We focus our discussion on the dipole response of the surface molecular layer.

A surface nonlinear susceptibility tensor of a molecular adsorbate layer at sum-frequency is defined as the sum of the molecular polarizability tensor per unit area [15]

$$\overleftrightarrow{\chi}^{(2)}(\omega_3) = N_s < \overleftrightarrow{\alpha}^{(2)}(\omega_3) >\,, \tag{3}$$

where N_s is the average surface density of the molecular adsorbates. The average is also performed over the distribution of the molecular orientation.[23] From Eq.(3), we conclude that one of the necessary conditions for a nonvanishing sum-frequency susceptibility is to require individual adsorbed molecules to have a nonvanishing molecular dipole polarizability, $\alpha^{(2)}(\omega_3)$. Another condition is to require the molecular layer as a whole to be noncentrosymmetric.

From the quantum mechanical perturbation theory, when the infrared frequency ω_2 is close to a vibrational resonance frequency of an adsorbed molecule, the nonlinear polarizability tensor can be separated into a resonant term and a nonresonant term

$$\alpha^{(2)}_{ijk}(\omega_3) = \alpha^{Res}_{ijk}(\omega_3) + \alpha^{Nonres}_{ijk}(\omega_3) , \tag{4}$$

and the resonant term is given by

$$\alpha^{Res}_{ijk}(\omega_3) = -\sum_s \frac{4\pi^2}{h^2}\left[\frac{(er_i)_{gs}(er_j)_{sf}}{\omega_3 - \omega_{sg} + i\,\Gamma_{sg}} - \frac{(er_j)_{gs}(er_i)_{sf}}{\omega_3 - \omega_{fs} + i\,\Gamma_{fg}}\right]\frac{(er_k)_{fg}}{\omega_2 - \omega_{fg} + i\,\Gamma_{fg}} , \tag{5}$$

where $(er_i)_{gs}$ etc, are the transition dipole matrix elements, ω_{fg} is a vibrational frequency of the molecule. The nonresonant term usually has essentially a flat response over the region where $\omega_2 \approx \omega_{fg}$. We now discuss some general features of SFG.

2. *Infrared activity and Raman activity*

First, we note that vibrational modes of an adsorbed molecule which can be observed as a vibrational structure in a sum-frequency spectrum must be both Raman and IR active. Qualitatively, this is derived from the requirement that the molecule does not have inversion symmetry. It is well-known that the vibrational modes of a molecule without centrosymmetry are necessarily both Raman and IR active. For a centrosymmetric molecule whose nonlinear susceptibility at sum-frequency is expected to be zero, the vibrational modes are either Raman active or IR active but not both. This suggests that there should be a quantitative correlation between the magnitude of the sum-frequency susceptibility of a vibrational mode and its IR and Raman activities. In fact, from quantum mechanics theory, we can show that there indeed exists such a stringent and quantitative

relation. Consider these three optical processes. In a linear resonant excitation with an infrared optical field $\mathbf{E}(\omega_{IR})$, the induced dipole moment at ω_{IR} and the corresponding linear polarizability are given by [15]

$$\mathbf{p}_k(\omega_{IR}) = \alpha_{kk}^{Res}(\omega_{IR})\, \mathbf{E}_k(\omega_{IR}) , \tag{6}$$

$$\alpha_{kk}^{Res}(\omega_{IR}) = -\frac{2\pi}{h} \frac{(er_k)_{gf}\,(er_k)_{fg}}{\omega_{IR} - \omega_{fg} + i\,\Gamma_{fg}} , \tag{7}$$

where the polarizability is the quantitative measure of the IR activity of the resonance. For an infrared-visible sum-frequency generation in the presence of a visible optical field $\mathbf{E}(\omega_{vis})$ and an infrared optical field $\mathbf{E}(\omega_{IR})$, the induced nonlinear molecular dipole moment and the corresponding polarizability at the sum-frequency are given by

$$\mathbf{p}_i(\omega_3) = \alpha_{ijk}^{Res}(\omega_3 = \omega_{vis} + \omega_{IR})\, \mathbf{E}_j(\omega_{vis})\, \mathbf{E}_k(\omega_{IR}) , \tag{8}$$

and Eq. (5) with $\omega_2 = \omega_{IR}$ and $\omega_1 = \omega_{vis}$. Finally, we consider a coherent stimulated Raman scattering process with a pump field $\mathbf{E}(\omega_3)$ and the Stokes field $\mathbf{E}(\omega_{vis})$. The induced Raman or third-order nonlinear dipole moment and the Raman polarizability are found as

$$\mathbf{p}_{i,\,Raman}(\omega_{vis}) = \alpha_{ijji}^{Res}(\omega_{vis})\, \mathbf{E}_j(\omega_3)\, \mathbf{E}_j^*(\omega_3)\, \mathbf{E}_i(\omega_{vis}) , \tag{9}$$

$$\left(\alpha_{ijji}^{Res}\right)^* = \left| \sum_s \frac{2\pi}{h} \left[\frac{(er_i)_{gs}\,(er_j)_{sf}}{\omega_3 - \omega_{sg} + i\,\Gamma_{sg}} - \frac{(er_j)_{gs}\,(er_i)_{sf}}{\omega_3 - \omega_{fs} + i\,\Gamma_{fs}} \right] \right|^2 \frac{2\pi}{h} \frac{1}{\omega_{IR} - \omega_{fg} + i\,\Gamma_{fg}} , \tag{10}$$

From Eq. (5), (7) and (10), we find that for a vibrational resonance ω_{fg}, the sum-frequency polarizability is quantitatively related to the corresponding IR polarizability and the Raman polarizability by

$$\left| \alpha_{ijk}^{Res}(\omega_3) \right|^2_{SFG} = \left| \alpha_{ijji}^{Res}(\omega_{vis}) \right|_{Raman} \times \left| \alpha_{kk}^{Res}(\omega_{IR}) \right|_{IR} . \tag{11}$$

This microscopic equation quantitatively confirms the requirement that only those modes which are both IR and Raman active should appear in SFG spectra as prominent structures. Furthermore, from absolute cross sections of IR absorption and Raman scattering of a vibrational mode, one can deduce the strength of the corresponding feature in the SFG using Eq. (11). For example, the infrared absorption cross section is proportional to the square of the direct transition dipole moment, $(er_k)_{fg}(er_k)_{gf}$. If we denote the Raman cross section as $d\sigma^R/d\Omega$,[15] we find from Eq. (11) that when $\omega_{IR} = \omega_{fg} = \omega_3 - \omega_{vis}$,

$$\left| \alpha_{ijk}^{Res}(\omega_3) \right|^2_{SFG} = \frac{c^4 \, \varepsilon_a(\omega_{vis})}{\omega_3 \, \omega_{vis}^3 \sqrt{\varepsilon_a(\omega_3)}} \left(\frac{2\pi}{h}\right)^2 \frac{(er_k)_{gf}(er_k)_{fg}}{\Gamma^2} \left(\frac{d\sigma^R}{d\Omega}\right) , \tag{12}$$

where ε_a's are the effective dielectric constants of the molecular adsorbate layer, and Γ is the spectral width of the vibrational mode. There exist extensively published literature and documents of experimentally determined Raman cross sections and IR absorption cross sections for a large number of molecules, and they are readily available from the literature or standard measurements.[24] These results can be directly used to calculate the strength of vibrational resonances in SFG spectra. Typically, the magnitudes of linear infrared polarizabilities α_{kk} are 10^{-23} to 10^{-24} esu, and Raman polarizabilities α_{ijji} are 10^{-34} esu.[25] From these values, we expect sum-frequency susceptibilities are on the order of

$$\alpha_{ijk}^{Res} \sim 10^{-29} \text{ esu} . \tag{13}$$

With typical surface densities of adsorbates, $N_s \sim 10^{15} / cm^2$, we anticipate typical surface SFG susceptibilities to be

$$\chi^{(2)}(\omega_3) \sim N_s \, \alpha_{ijk}^{Res}(\omega_3) \sim 10^{-14} \text{ esu} . \tag{14}$$

Therefore, vibrationally resonant SFG should be readily observable as a surface nonlinear susceptibility of $\chi^{(2)} \sim 10^{-15}$ esu is easily measurable in SHG.[15]

3. *Electronic resonance enhancement*

It is well-known that Raman scattering can be enhanced when optical pumping frequencies are close to the electronic resonances of the molecules. Such an effect is routinely used to study electronic excitations of molecules and even solid materials such semiconductors. It is also used to selectively enhance the optical response of some of the material properties which are otherwise overwhelmed by the large background or simply too weak to be observed. As vibrationally resonantly enhanced SFG or DFG is also a Raman active process, we expect the same electronic resonant enhancement in the sum-frequency generation when ω_3 ($= \omega_{vis} + \omega_{IR}$) is close to an vibronic resonance ω_{sg}, given in Eq. (5). These electronic resonances can be used to further increase the vibrational SFG signals from the surface layer against the residual bulk contribution. In addition, the electronic resonance enhancement can be also applied to studies of electronic excitations at the surface which we will not pursue further here.[17]

4. *The lineshape of SFG spectra*

Like any other coherent spectroscopy such as reflectance and coherent Raman spectroscopies, the overall spectral lineshape of a typical SFG vibrational spectrum is not simply a sum of Lorentzian curves with different center frequencies as opposed to infrared absorption or incoherent Raman scattering spectra.[26] If we include all the resonant terms and the nonresonant term in the Eq. (4), we can write down the complete expression for the sum-frequency polarizability,

$$\alpha_{ijk} = \alpha_{ijk}^{Nonres} + \sum_{\delta} \frac{A_{ijk}^{\delta}}{\omega_{IR} - \omega_{\delta} + i\ \Gamma_{\delta}}\ , \tag{15}$$

where A_{ijk}'s include other factors in Eq. (5). For large molecules, important contributions to the non-resonant term can come from off-resonant vibrational modes which are large in number and strong in IR and Raman activities and are also usually not too far off from the frequency range of an experiment. Since the SFG intensity is measured in the experiment and it is proportional to the square of α_{ijk}, if we neglect the effects of the molecular orientation distribution and the possibly different adsorption sites, the overall lineshape of a vibrational SFG spectrum is given by

$$|\alpha_{ijk}|^2 = \left| \alpha_{ijk}^{Nonres} + \sum_{\delta} \frac{A_{ijk}^{\delta}}{\omega_{IR} - \omega_{\delta} + i\,\Gamma_{\delta}} \right|^2 , \tag{16}$$

which has a typical dispersive lineshape near resonances. Only when the transition frequencies are far apart compared to the linewidths Γ_{δ}, and the nonresonant contribution α^{Nonres} is negligible, the SFG spectral shape $S(\omega_{IR}) \sim |\alpha_{ijk}|^2$ can be approximated by a sum of a number of Lorentzian curves

$$S(\omega_{IR}) \sim \sum_{\delta} \frac{|A^{\delta}_{ijk}|^2}{(\omega_{IR} - \omega_{\delta})^2 + \Gamma_{\delta}^2} . \tag{17}$$

5. *Intensity of sum-frequency generation*

Given the nonlinear polarization in Eq. (1) as the source term, we can solve Maxwell Equations with appropriate boundary conditions to obtain the electric field of reflected and transmitted SFG radiation. The general results have been derived by Pershan and Bloembergen in their early classic paper and Heinz in his unpublished thesis.[27, 15] For example, with a s-polarized visible laser beam and p-polarized infrared beam to excite molecular vibrational resonances, we find that for a monolayer of molecular adsorbates which is isotropic in the surface plane, the intensity of the s-polarized SFG in reflection direction from the adsorbate layer is given as

$$S(\omega_3) = \frac{c}{8\pi} \left| \frac{4\pi\,[\,k(\omega_3)\,]^2}{k_z^R(\omega_3) - k_z^T(\omega_3)} \right|^2 \left| \chi^{(2)}_{yzy}(\omega_3)\, E_z(\omega_{IR})\, E_s(\omega_{vis}) \right|^2 A\,\tau , \tag{18}$$

where k^R and k^T are wave vectors in reflection and transmission, respectively; $k(\omega_3)$ is the wave vector in vacuum; the surface plane coincides with the x-y plane with the x-axis in the plane of incidence; the z-axis is along the surface normal pointing into the medium of transmission. A is the area over which the IR beam overlaps with the visible beam; τ is the temporal overlap of the two beams; $\chi_{yzy}(\omega_3)$ is given by Eq. (3). If there is anisotropy within the layer, we expect additional contributions to the right hand side of Eq.(18) from other components of the surface susceptibility tensor $\chi^{(2)}$.

From Eq. (3), (16) and (18), we point out that averaging over the distribution of the molecular orientation can alter the relative strengths of different vibrational resonances and

the non-resonant term in a SFG spectrum. In cases that the resonant features are well separated and the nonresonant term is negligible, by choosing different combinations of input and output polarizations, one can deduce more information on the distribution of the molecular orientation on the surface.

To have an estimate of a typical SFG signal strength, for example, we assume that infrared and visible pump beams have the same pulsewidths $\tau_p = 10$ ns and same single-pulse energies $E = 10$ mJ. They are focused to a same beam size of 1 mm^2 on a sample which is assumed to have a $\chi^{(2)}(\omega_3) = 10^{-14}$ esu. If we neglect the macroscopic Fresnel factor, from Eq. (18), we arrive at a sum-frequency signal strength of 10^2 to 10^3 photons per pulse. This is easily detected with photon counting techniques.

C. Experimental procedure

To demonstrate the principle, we studied the infrared-visible vibrational SFG spectrum of a monolayer of coumarin 504 molecules (Exciton Chemical Co., Inc.) spin-coated on a substrate of fused silica. The structure of a coumarin 504 molecule is shown in Fig. 1, and it clearly does not have centrosymmetry. The double-bonded oxygen on the coumarin 504 molecule is likely to attach to residual hydroxides on the fused silica substrate through hydrogen-bonding. This presumably provides the principal mechanism responsible for the asymmetric distribution of the molecular orientation and leads to the breakdown of inversion symmetry of the adsorbed coumarin 504 layer. The molecule has rich vibrational resonances which are both Raman and IR active in solutions or in solid phase. This enabled us to obtain the first molecular vibrational spectrum with infrared-visible SFG technique by using a narrowly a discretely tunable CO_2 laser to excite the vibrational resonances.

The fused silica substrate was treated with a standard cleaning procedure which is commonly used for preparing a SiO_2-covered silicon wafer surface in microelectronics processing. First, the substrate was cleaned with detergents and rinsed in a running tap water. It was then submerged in acetone for 3 to 5 minutes to remove organic contaminants before rinsed with distilled water a few times. Afterwards, the substrate was placed in Piranha solution (60% H_2O_2 and 40% H_2SO_4) for 10 minutes to remove residual organic contaminants. Finally, it was rinsed 4 to 5 times with distilled water to remove the residual acid and then dried with gentle blow of dry nitrogen. The cleanliness was checked with "water-breaking" test. For a fused silica surface free of organic contaminants which are the major impurity constituents, water wets the surface completely without breaking into patches. For the deposition of a monolayer of coumarin 504 molecules with the spin-coating technique,[28] we prepared a coumarin 504 solution with a molar concentration of 3×10^{-7} mole/ml. The resultant surface coverage was calculated to be 2 to 3×10^{14} /cm^2 after the spin-coating. The prepared sample was kept in the ambient of dry nitrogen to prevent oxidation during the experiment.

The optical arrangement is shown in Fig. 2. For infrared excitation, we used a discretely tunable CO_2 TEA (transversely excited atmospheric pressure) laser which could excite vibrational resonances in the frequency range between 920 cm^{-1} to 1100 cm^{-1}. Within the tuning range, there are three frequency regions of 10 cm^{-1} to 30 cm^{-1} wide over which the CO_2 laser ceases to lase and therefore we were not able to probe the vibrational resonances in these regions either. The line-to-line tuning has spacings of 1 cm^{-1} to 2 cm^{-1}. The CO_2 laser was operated at 0.5 Hz and the output was parallel-polarized. For the visible beam, we used the frequency-doubled output of a Nd:YAG laser operating at 0.532 μm. It was s-polarized and operated synchronously with the CO_2 laser.

Unlike optical second-harmonic generation in which harmonic frequencies are far apart from the corresponding pumping frequencies so that spectral filtering is often sufficient to separate the harmonics from the fundamentals, the sum-frequency is only a

few hundred angstroms (in our case, 300Å) apart from the visible pumping frequency. Therefore, we had to use a spatial filtering scheme by adopting an optical arrangement in which the two excitation beams were brought onto the sample from different angles. In this way, the reflected coherent SFG came out at a sufficiently different angle from that of the reflected visible pumping beam so that it could be detected after a relatively modest spectral filtering. The angle at which SFG is radiated out of the surface is determined by the phase-match condition at the sum-frequency, [15]

$$k_x^R(\omega_3) = k_x^I(\omega_{vis}) + k_x^I(\omega_{IR}) , \tag{19}$$

$$\theta^R(\omega_3) = \sin^{-1}\left(\frac{\omega_{vis}\sin(\theta^I(\omega_{vis})) - \omega_{IR}\sin(\theta^I(\omega_{IR}))}{\omega_{vis} + \omega_{IR}} \right) , \tag{20}$$

where k^I 's are the wave vectors of the incident excitation beams, θ^I 's are the incident angles with respect to the surface normal. For different frequency generation, the reflected angle is similarly determined by

$$k_x^R(\omega_3') = k_x^I(\omega_{vis}) - k_x^I(\omega_{IR}) . \tag{21}$$

$$\theta^R(\omega_3') = \sin^{-1}\left(\frac{\omega_{vis}\sin(\theta^I(\omega_{vis})) + \omega_{IR}\sin(\theta^I(\omega_{IR}))}{\omega_{vis} - \omega_{IR}} \right) . \tag{22}$$

In our experiment, we have chosen $\theta^I(\omega_{vis}) = \theta^I(\omega_{IR}) = 45°$. The intensity of the CO_2 laser changes with time and even from shot to shot. A single crystal GaAs(100) was used in a symmetrically arranged reference arm for normalization. The beam energies of the excitation lasers incident on the sample over a 7-mm^2 spot were 5 mJ / 7ns at 0.532 μm and 2 mJ / 140 ns at the infrared wavelength, respectively. Photon-counting detection

systems were used to record the SFG signals with efficiencies of 0.86%. Typically, the signal strength from a monolayer of adsorbed coumarin 504 molecules was ~ 500 photons/pulse.

D. Results and data analysis

In order to anticipate what we should expect to observe in the SFG spectrum, we first measured the infrared absorption and Raman scattering spectra of solid coumarin 504, and the visible absorption spectrum of coumarin 504 in ethanol. In Fig. 3, 4(a) and 4(b), we display portions of these spectra. The vibrational modes with center frequencies at 922 cm^{-1}, 948 cm^{-1}, 1050 cm^{-1}, 1078 cm^{-1} and 1090 cm^{-1} are in the frequency range of the CO_2 laser. As we can see, they are both Raman and infrared active. From the earlier discussion, we expect to observe these vibrational resonances in the SFG spectrum. As we can see from the visible absorption spectrum, the sum-frequency is close to the first electronic transition of coumarin 504 molecules so that we expect a partial electronic resonance enhancement in SFG. In contrast to SFG, we notice that the difference frequency however is already near the tail end of the absorption spectrum, and we should then anticipate a much reduced resonance enhancement in DFG. We measured the surface SFG and DFG signals as functions of the CO_2 laser frequency ω_{IR}. The fused silica substrate generated little signal compared to that from the monolayer of coumarin 504 molecules. Knowing the detection efficiency, we have determined the absolute SFG intensity which allowed us to evaluate the surface susceptibility tensor component from Eq. (18). In Fig. 5, we depict the square of the measured SFG susceptibility tensor component, $|\chi_{yzy}(\omega_3 = \omega_{vis} + \omega_{IR})|^2 = |\mathbf{e}_y \cdot \chi^{(2)}(\omega_3) : \mathbf{e}_z\mathbf{e}_y|^2$ deduced from the absolute SFG intensity measurement. To correlate the SFG spectrum with the Raman and IR

spectra, we must keep in mind that, a) interference between χ^{Nonres} and χ^{Res} and between different terms in χ^{Res} can change the spectral lineshapes; b) the frequencies of various vibrational resonances are different for adsorbed molecules and for molecules in a solid; c) the strengths of individual peaks depend on the distribution of the molecular orientation. Two resonant structures are clearly resolved in the SFG spectrum. They can be identified with the infrared and Raman peaks around 950 cm^{-1} and 1050 cm^{-1}, respectively. The resonant features at 920 cm^{-1} and 1090 cm^{-1} in the IR and Raman were not resolved. They seemed to have shifted out of the spectral range which we could probe. As we mentioned earlier, the other infrared and Raman peaks at 986, 1016 and 1028 cm^{-1} also are out of the spectral tuning range. We note that the magnitude of the measured surface susceptibility is of the order of 10^{-29} esu which is close to what we should expect for a typical noncentrosymmetric molecule. The difference frequency generation (DFG) spectrum was essentially the same except the absolute intensity was 10 times weaker. This is clearly indicative of an electronic resonant enhancement for the sum-frequency generation (SFG) and a strong frequency dispersion from the SFG to the DFG as we have expected from the visible absorption spectrum. The error bars primarily came from the photon-statistics as well as the residual effect of the shot-to-shot fluctuation of the CO_2 laser output.

To analyze the observed SFG spectrum, we recall that the surface susceptibility tensor component $\chi_{yzy}(\omega_3)$ can be expressed as

$$\chi^{(2)}_{yzy}(\omega_3) = N_s < \mathbf{e}_y \cdot \overleftrightarrow{\alpha}^{(2)} : \mathbf{e}_z\, \mathbf{e}_y > . \tag{23}$$

The average is performed over the distribution of the molecular orientation including the azimuthal angle in the surface plane. Usually, we also expect contributions from more than one component of the molecular polarizability tensor, $\alpha^{(2)}(\omega_3)$. This is due to the fact that the symmetry operation for coumarin 504 molecules is a mirror plane coinciding with the

plane of the molecule. For each resonance, there can be a number of non-zero molecular polarizability tensor components. Their relative contributions to the measured susceptibility component χ_{yzy} depend on the input polarizations (s-polarization for the visible beam, p-polarization for the infrared beam) and the output polarization, and the distribution of the molecular orientation. As the surface of a fused silica substrate is isotropic, we expect the adsorbate layer to be isotropic with respect to the azimuthal angle. This should lead to a s-polarized SFG output which was what we observed. Generally speaking, the average indicated in Eq. (23) can change the relative intensities of the observed modes whose strengths should otherwise directly correlate with the Raman activity and IR activity as given in Eq. (11). We can still write down the effective susceptibility component after the average as

$$\chi_{yzy}(\omega_3) = \chi_{yzy}^{Nonres} + \sum_{\delta} \frac{A_\delta}{\omega_{IR} - \omega_\delta + i\,\Gamma_\delta} \quad , \tag{24}$$

where we have factored out the Lorentzian functions of the vibrational resonances, and incorporated all other factors into A_δ's. We assume that inhomogeneous broadening is negligible compared to the homogeneous spectral widths, Γ_δ's. This is reasonable as the intra-molecular coupling for large molecules like coumarin 504 is usually large compared to the inter-molecular coupling, and we do not expect significant differences between adsorption sites on an otherwise amorphous surface of fused silica. The summation is carried over those modes which are within the CO_2 laser tuning range. In general, χ^{Nonres} and A_δ's are complex numbers. In cases that spin-orbital interactions have negligible effect on the electronic resonances involved in the sum-frequency generation, one can show that χ^{Nonres} and A_δ's are real numbers. With χ^{Nonres} and A_δ and ω_δ as adjustable parameters and Γ_δ assumed to have the same values as the IR and Raman halfwidths in Fig. 4(a) and 4(b), we fitted the experimental data using Eq. (24). The result is shown in the solid curve

in Fig. 5. In Table I, we list the values of the parameters from the fitting and the assignment of the vibrational modes that appeared in the SFG spectrum.

With the surface coverage $N_s = (2.5 \pm 0.5) \times 10^{14}$ /cm^2, we calculated the effective molecular polarizability of the observed modes which are defined as $\alpha_\delta = A_\delta/\Gamma_\delta$. They are listed in the last column in Table I. While those values obtained for the partially observed resonances in Fig. 5 are not necessarily accurate, the ones obtained for the two well-defined features are reasonably certain. The resonance frequencies are clearly shifted from the solid phase values. This is attributed the interaction of the molecule with the surface of the fused silica substrate. The magnitudes of both the nonresonant term and the resonant term are comparable and fairly large. We will discuss the detail account of these results in the discussion section.

E. Discussion

From Fig. 3, 4(a), 4(b), 5 and Table I, we can conclude that the *relative* intensities of the two well-defined vibrational modes roughly correspond to the products of the infrared absorption and Raman scattering intensities. The exact ratio between these modes depend on the orientation of the coumarin 504 molecules on fused silica, the input and output polarization combination and the interactions with substrate atoms. In this section, we explore the quantitative relation of the measured molecular SFG nonlinear susceptibility tensor element with the infrared and Raman activities of the observed modes. In Table I, we have listed the measured polarizabilities for each observed vibrational resonances. In order to compare these results with the Raman and IR activities more quantitatively , we need to determine the absolute IR absorption cross sections and Raman scattering cross sections of the corresponding modes.

There do not exist detailed infrared and Raman spectroscopic data which we can use for calculation. In principle, these data can be obtained from an absolute IR absorption and a Raman scattering measurement. We chose to perform a set of relative measurements using a reference molecule with well-documented spectroscopic data. The molecule which we used is pyridine. Pyridine is one of the most studied polyatomic molecules. The infrared absorption cross section and the Raman cross section of pyridine in gas and liquid phase are well-documented in the literature.[29] We can conveniently use these information and properly conduct relative measurements for our purpose. In the relative infrared absorption measurement, we dissolved coumarin 504 and pyridine separately in CCl_3H solvent, and separate absorption spectra were taken under identical conditions and with the same number of coumarin 504 and pyridine molecules in the solutions so that we could directly compare the intensities. In Fig. 6, we display the measured spectra after subtraction of the background absorption of CCl_3H. We focus on the well-resolved resonance at 1050 cm^{-1} for coumarin 504 molecule. The ratio of the peak absorbances of the 1050 cm^{-1} mode to the 992 cm^{-1} mode of pyridine is close to $\gamma^{IR} = 0.5$. From the literature,[29] we find that the infrared transition dipole moment, $(\mathbf{er})_{fg}$, of the 992 cm^{-1} mode of pyridine has a magnitude of 0.02 $ea_B = 5.1 \times 10^{-20}$ esu. The halfwidth of the 992 cm^{-1} mode of liquid pyridine is 1.7 cm^{-1} or 3.2×10^{11} sec^{-1}. We then calculated the infrared polarizability using Eq. (7) for the 992 cm-1 mode of pyridine, $\alpha^{(1)}(\omega_{IR}) = 7.6 \times 10^{-24}$ esu. From this result and γ^{IR}, the infrared polarizability for 1050 cm^{-1} mode of coumarin 504 is determined as

$$\alpha_{IR}^{Res}(\omega_{IR} = 1050\ cm^{-1}) = 3.8 \times 10^{-24}\ esu\ . \tag{25}$$

In the relative Raman scattering measurement, pyridine was used as the solvent for coumarin 504 molecules. In this case, 40 mg of coumarin 504 was dissolved in 330 mg of

pyridine. In Fig. 7, we show a portion of the measured Raman spectrum. With the pump beam at 6764 Å, we find that the ratio of Raman peak intensities of the 1050 cm^{-1} mode to the 992 cm^{-1} mode is about $\gamma^{Raman} = 0.30$ after normalized against the molecular densities. Again from the literature,[17] we know that the 992 cm^{-1} mode has a differential Raman cross section $d\sigma^R/d\Omega = 1.5 \times 10^{-29}$ cm^2 $ster^{-1}$ when pumped at this wavelength. Using Eq. (12), we calculated the vibrationally resonant Raman polarizability for the 992 cm^{-1} mode using $\Gamma = 3.2 \times 10^{11}$ sec^{-1}, and $\varepsilon_a(\omega_3) \sim \varepsilon_a(\omega_{vis}) \sim 2$ for liquid pyridine

$$\alpha^{Res}_{Ramen}(\omega_{vis}) = \frac{2\pi\, c^4\, \varepsilon_a(\omega_{vis})}{\omega_3\, \omega^3_{vis} \sqrt{\varepsilon_a(\omega_3)}\; h\, \Gamma} \frac{d\sigma^R}{d\Omega} = 1 \times 10^{-33} \text{ esu} \cdot \tag{26}$$

From Eq. (26) and $\gamma^{Raman} = 0.3$, the Raman polarizability for the 1050 cm^{-1} mode of coumarin 504 was deduced as

$$\left| \alpha^{Res}_{Raman}(\omega_{vis}) \right|_{coumarin\,504} = 3 \times 10^{-34} \text{ esu} . \tag{27}$$

The magnitude of the SFG polarizability for the 1050 cm^{-1} mode was then calculated from Eq. (11), (25) and (27)

$$\left| \alpha^{Res}_{SFG}(\lambda_3 = 6764 \text{ Å}) \right|_{coumarin\,504} = \sqrt{\left| \alpha^{Res}_{Raman}(\omega_{vis}) \right| . \left| \alpha^{Res}_{IR}(\omega_{IR} = 1050 \text{ cm}^{-1}) \right|} , \tag{28}$$

$$\left| \alpha^{Res}_{SFG}(\lambda_3 = 6764 \text{ Å}) \right|_{coumarin\,504} = 3.4 \times 10^{-29} \text{ esu} . \tag{29}$$

In our SFG measurement however, the equivalent Raman excitation wavelength is that of the SFG, $\lambda_{SFG} = 5050$ Å. There is an electronic resonant enhancement as indicated by the

visible absorption spectrum. In Fig. 3, we observed a substantial drop in absorbance from the sum-frequency at 5051 Å passing the visible pump frequency at 5320 Å to the difference frequency at 5635 Å. This is responsible for the drastic decrease (a factor of 10) in the signal strength from SFG to DFG for the same vibrational resonance. To find out the exact resonance enhancement, we need to evaluate the electronic resonance factor. It is easily seen that the ratio of the vibrationally resonant sum-frequency polarizability to the difference frequency polarizability is expressed as

$$\frac{\left| \alpha_{DFG}^{Res}(\omega_3') \right|}{\left| \alpha_{SFG}^{Res}(\omega_3) \right|} = \frac{\omega_{sg} - \omega_3'}{\omega_{sg} - \omega_3} = \frac{(\omega_{sg} - \omega_3) + (\omega_3 - \omega_3')}{\omega_{sg} - \omega_3} , \tag{30}$$

where ω_{sg} is the angular frequency associated with the first electronic resonance, ω_3 is the sum-frequency, and ω_3' is the difference frequency. Since both the SFG and DFG are close to the electronic resonance, we expect that the dominating part of the non-resonant terms α^{Nonres} has the same electronic resonance factor as the vibrationally resonant term. This arises from the fact that the nonresonant contribution mainly comes from those vibrational modes which appear outside of the frequency range of our experiment, and hence they should experience the same electronic resonance enhancement,

$$\alpha_{SFG}^{Nonres}(\omega_3) \approx \frac{1}{\omega_{sg} - \omega_3} \sum_{\delta'} \frac{B_{\delta'}}{\omega_{IR} - \omega_{\delta'}} , \tag{31}$$

$$\alpha_{DFG}^{Nonres}(\omega_3') \approx \frac{1}{\omega_{sg} - \omega_3'} \sum_{\delta'} \frac{B_{\delta'}}{\omega_{IR} - \omega_{\delta'}} , \tag{32}$$

where $B_{\delta'}$ include transition matrix elements and other common factors and constants. Therefore, Eq. (30) is valid for the overall SFG and DFG polarizability in the present case.

From the experimental results, we have found that the SFG intensity is 10 times as strong as the of the DFG. From Eq. (30), this leads to

$$\frac{\omega_{sg} - \omega_3 + (\omega_3 - \omega_3')}{\omega_{sg} - \omega_3} \approx 3.3 \,. \tag{33}$$

Since $\omega_3 - \omega_3' = 2\,\omega_\delta = 3.96 \times 10^{14}$ /sec, from Eq. (33), we could deduce the resonant frequency factor for SFG as

$$\omega_{sg} - \omega_3 = 1.7 \times 10^{14} \text{ /sec}, \tag{34}$$

and with the SFG frequency $\omega_3 = 3.7 \times 10^{15}$ /sec or $\lambda_3 = 5051$ Å, we found

$$\omega_{sg} = 3.9 \times 10^{15} \text{ /sec}. \tag{35}$$

Finally, the electronic resonance enhancement factor for the SFG polarizability corresponding to 1050 cm^{-1} mode of coumarin 504 molecules with the effective pump beam wavelength changing from 6764 Å to 5050 Å was calculated as

$$\frac{\omega_{sg} - \omega_3(6764\text{ Å})}{\omega_{sg} - \omega_3(5320\text{ Å})} = 6.5 \,, \tag{36}$$

and the resultant SFG polarizability for the 1050 cm^{-1} mode was

$$\left| \alpha_{SFG}^{Res}(\lambda_3 = 5051\text{ Å}) \right| = 2.2 \times 10^{-28} \text{ esu} \,. \tag{37}$$

Comparing with the result of the direct SFG measurement for the same mode, α_{SFG} = $(0.89 \pm 0.1) \times 10^{-28}$ esu, the agreement is remarkably good. The average over the molecular orientation on the surface is most likely to be responsible for the difference between the calculation based on the IR and Raman scattering measurements and the SFG measurement. This result confirmed the qualitative and quantitative relation of the SFG from an molecular adsorbate layer with the existing molecular spectroscopic data. The sensitivity of SFG and DFG to electronic resonances at the surface was also clearly demonstrated here. It should be very useful in studies of electronic resonances at surfaces and interfaces.

We can also explain the large non-resonant contribution observed in the SFG spectrum using a similar analysis. In the vicinity of CO_2 tuning range, there are about 10 to 15 modes which are only 100 cm^{-1} to 600 cm^{-1} away from 1100 cm^{-1}. They are both highly Raman and IR active. Their averaged Raman intensities are 10 to 13 times as strong as that of 1050 cm^{-1} and their averaged IR peak absorbances are 4 to 5 times as strong as that of 1050 cm^{-1} mode. But on the average, they are about 300 cm^{-1} out of resonance. Compared to the resonant term such as that of 1050 cm^{-1} mode, the overall non-resonant term can be estimated from Eq. (29), and we find that it is about a factor of 2 to 4 times as large. Compared with the measured nonresonant term given in Table I where we have $\alpha^{Nonres}/\alpha^{Res} \approx 1.3$, and considering the effect of the molecular orientation on the effective contribution of these outside modes, the agreement between the calculation and the measurement is remarkably well.

We point out that our data has showed good agreement with our general theoretical description. These results form a useful and consolidated base for future applications of vibrational as well as electronic SFG spectroscopy to studies of surfaces and interfaces.

One of the most important and natural applications of the vibrational SFG in surface science is to study transient processes on surfaces. Resonantly enhanced SFG pumped with short pulsed lasers should enable us to selectively monitor the transient species on a

surface with time resolution as short as subpicosecond.[16, 20] Free electron lasers operating in the infrared frequency range can now provide the desired brightness, broad tuning range and pulses as short as a few picoseconds. Many table-top laser systems can now generate ultrashort laser pulses in the visible and near infrared. With adequate spectral brightness together with the ultrashort pulse duration, ultrafast dynamics of surface vibrational resonances can be studied by transient SFG, which we will discuss in the next chapter Direct pump-and-probe experiments to study the vibrational relaxation in a Langmuir-Blodgett film with picosecond resolution have been reported following this work.[20]

Another important application of infrared-visible sum frequency generation spectroscopy is to obtain information on the orientation of the adsorbates. This is particularly effective when the sum-frequency is also in resonance with an electronic transition. As in the case of SHG, the ratios between various tensor components of $\chi^{(2)}(\omega_3)$ are functions of the orientational distribution of the adsorbates and can be measured by using proper input-output polarization combinations in SFG. In principle, we can select the two pump frequencies in resonance simultaneously with a particular electronic resonance and a vibrational resonance. This will help to define the molecular axis more reliable and more selective so that one can deduce the molecular orientation distribution simpler and more effective. Although there have been no reports of molecular orientation studies using both the vibrational and electronic resonances, we have witnessed a number of elegant experiments in which SFG was used as a bond- or mode-selective probe to monitor the change of the bond-orientation of the adsorbates on surfaces.[19]

It is important to extend the current work to surfaces or interfaces of other more interesting materials such as metals and semi-conductors. We found that metal and semi-conductor substrates normally yield substantially large SFG and DFG signals. Using the same experimental set-up, we have measured the effective surface SFG susceptibilities for a number of metals and semiconductors relative to that of the coumarin 504 molecule. It is more relevant to speak about susceptibilities instead of polarizabilities for intrinsic surfaces.

For convenience, the "effective surface susceptibility" of an intrinsic surface of a substrate is defined here by treating the surface as a thin layer placed on fused silica with a unit dielectric constant. In Table II, we list the measured effective SFG susceptibilities for a number of semi-conductors and metals in the air. We used λ_{vis} = 5320 Å with s-polarization and λ_{IR} = 9.57 μm with p-polarization. There are no observable dispersion from DFG to SFG measurements from these substrates. The magnitudes are of the order of 10^{-14} esu which are comparable to that of pyridine, $\chi^{(2)} = 1.2 \times 10^{-14}$ esu (assuming a surface density of 2×10^{14} /cm^2). Since these surfaces in air are usually covered with contaminants and metallic compounds or oxides, we expect the SFG responses will be stronger from the clean surfaces under ultrahigh vacuum as has been the case in SHG. The intrinsically high nonlinearity and strong electronic resonance enhancement of SFG from metal and semiconductor surfaces can be used to study surface and interface electronic as well as vibrational spectroscopy. This is particularly interesting when localized surface states are involved and high spectral resolution is desired. As a special case of application of SFG to surface electronic spectroscopy, resonant SHG has been successfully used to identify a gap state at the interface of Si(111) and CaF_2 by a IBM research group recently.[17] This will certainly not be the last and most interesting example.

F. Conclusion

We have shown that infrared-visible sum-frequency generation from surfaces can be used for surface and interface vibrational spectroscopy. We have demonstrated the general features of this new spectroscopic technique and the correlation with the more familiar infrared absorption and Raman scattering spectroscopies. With the potentially ultrahigh time and spectral resolutions and capability of accessing various types of interfaces,

resonantly enhanced SFG will find wide application in studies of spectroscopy and ultrafast dynamics and transient phenomena at surfaces and interfaces.

References:

1. See, for example, *Vibrational Spectroscopy of Adsorbates*, edited by R. F. Willis, Springer Series in Chemical Physics, Vol. 15 (Springer, Berlin, 1980); *Surface Studies with Lasers*, edited by F. R. Auessenegg, A. Leitner, and M. E. Lippitsch. Springer Series in Chemical Physics, Vol. 33 (Springer, Berlin, 1983);
2. H. Ibach and D. L. Mills, *Electron energy Loss Spectroscopy and Surface Vibrations* (Academic, New York, 1982).
3. W. Daum, C. Stuhlmann, and H. Ibach, Phys. Rev. Lett. 60, 2741 (1988); W. Daum, J. Electron. Spectrosc. Rel. Phen. 44, 271 (1987); W. Daum, S. Lehwald and H. Ibach, Surf. Sci. 178, 528 (1986).
4. J. C. Tully, Y. J. Chabal, Krishnan Raghavachari, J. M. Bowman, and R. R. Lucchese, Phys. Rev. B 31, 1184 (1984).
5. G. A. Somorjai, Chemistry in Two Dimensions: Surfaces (Cornell University Press, Ithaca, NY, 1981), p.360.
6. Y. J. Chabal, Phys. Rev. Lett. 55, 845 (1985); Y. J. Chabal, G. D. Higashi, and S. B. Christman, Phys. Rev. B 28, 4472 (1983).
7. F. Träger, H. Coufal, and T. J. Chuang, Phys. Rev. Lett. 49, 1720 (1982).
8. T. J. Chuang, J. Electron Spectrosc. Relat. Phenom. 29, 125 (1983).
9. S. Chiang, R. G. Tobin, P. L. Richards, and P. A. Thiel, Phys. Rev. Lett. 52, 648 (1984).
10. B. N. J. Persson and M. Persson, Solid State Commun. 36, 175 (1980); B. N. J. Persson and M. Persson, Surf. Sci. 97, 609 (1980); B. N. J. Persson and R. Ryberg, Phys. Rev. B 24, 6954 (1981); B. N. Persson and R. Ryberg, Phys. Rev. Lett. 48, 549 (1982); R. Ryberg, Surf. Sci. 114, 627 (1982); Hiromu Ueba and Shoji Ichimura, J. Phys. Soc. Japan. 50, 3996 (1981);

M. Persson, B. Hellsing, and B. I. Lundqvist, Journal of Electron Spectroscopy and Related phenomena, 29, 119 (1983);

B. N. J. Persson and R. Ryberg, Phys. Rev. Lett. 54, 2119 (1985);

B. N. J. Persson and R. Ryberg, Phys. Rev. B 32, 3586 (1985).

11. J. W. Gadzuk and A. C. Luntz, Surf. Sci. 144, 429 (1984).

12. J. P. Heritage and D. L. Allara, Chem. Phys. Lett. 74, 507 (1980).

13. E. J. Heilweil, M. P. Casassa. R. R. Cavanagh, and J. C. Stephenson, J. Vac. Sci. Technol. B 3 (5), 1471 (1985);

M. P. Casassa, E. J. Heilweil, J. C. Stephenson, and R. R. Cavanagh, J. Vac. Sci. Technol. A 3 (3), 1655 (1985);

E. J. Heilweil, M. P. Casassa, R. R. Cavanagh, and J. C. Stephenson, Chem. Phys. Lett. 117, 185 (1985);

E. J. Heilweil, M. P. Casassa, R. R. Cavanagh, J. C. Stephenson, J. Chem. Phys. 82, 5216 (1985).

14. An initial attempt of such an experiment was reported by H. W. K. Tom, Ph. D. thesis, University of California, Berkeley, 1984 (unpublished);

X. D. Zhu, H.Suhr, and Y.R. Shen, Phys. Rev. B 35, 3047 (1987).

15. See, for example, Y. R. Shen, *The Principles of Nonlinear Optics* (Wiley, New York, 1984), Chap. 25;

Y. R. Shen, J. Vac. Sci. Technol. B 3, 1464 (1985), and references therein;

Y. R. Shen, Nature, 337, 519 (1989).

16. H. W. K. Tom, G. D. Aumiller, C. H. Brito-Cruz, Phys. Rev. Lett. 60, 1438 (1988);

C. V. Shank, R. Yen, and C. Hirlimann, Phys. Rev. Lett. 51, 900 (1983).

17. T. F. Heinz, C. K. Chen, D. Ricard, and Y. R. Shen, Phys. Rev. Lett. 48, 478 (1982);

J. M. Hicks, L. E. Urbach, E. W. Plummer, and Hai-Lung Dai, Phys. Rev. Lett. 61, 2588 (1988);

T. F. Heinz, F. J. Himpsel, and E. Palange, to be published.

18. S. Chiang, Ph. D. thesis, University of California, Berkeley, 1983 (unpublished)
R. G. Tobin, Ph. D. thesis, University of California, Berkeley, 1985 (unpublished).

19. J. H. Hunt, P. Guyot-Sionnest, and Y. R. Shen, Chem. Phys. Lett. 133, 189 (1987);
P. Guyot-Sionnest, J. H. Hunt, and Y. R. Shen, Phys. Rev. Lett. 59, 1597 (1987);
P. Guyot-Sionnest, R. Superfine, and J. H. Hunt, Chem. Phys. Lett. 144, 1 (1988);
A. L. Harris, C. E. Chidsey, N. J. Levinos, and D. N. Loiacono, Chem. Phys. Lett. 141, 350 (1987).

20. A. L. Harris and N. J. Levinos, J. Chem. Phys. 90, 3878 (1989).

21. *Surface Enhanced Raman Scattering*, edited by R. K. Chang and T. E. Furtak (Plenum, New York, 1981);
M. Mosskovits, Rev. Mod. Phys. 57, 783 (1985).

22. J. A. Armstrong, N. Bloembergen, J. Ducuing, and P. S. Pershan, Phys. Rev. 127, 1918 (1962).

23. T. F. Heinz, H. W. K. Tom, and Y. R. Shen, Phys. Rev. A 28, 1883 (1983).

24. See, for example, G. Herzberg, Spectra of Diatomic Molecules, 2nd edition (D. Van Nostrand Company, Toronto, 1950);
G. Herzberg, Infrared and Raman Spectra of Polyatomic Molecules (Van Nostrand Reinhold Company, New York, 1945);
L. M. Sverdlov, M. A.Kovner, and E. P. Krainov, Vibrational Spectra of Polyatomic Molecules (John Wiley & Sons, New York, 1974);
Raman Spectroscopy of Gases and Liquids, edited by A. Weber (Spring Verlag, Berlin, 1979).

25. See, for example, Y. R. Shen, Ref. 9, Chaps 2 and 10. We use the following representative values: infrared dipole moment ~ 5×10^{-19} esu, Raman scattering cross section ~ 1×10^{-29} $sr^{-1}cm^{-1}$, and vibrational linewidth on a surface $\Gamma \sim 5$ cm^{-1}.

26. D. K. Lambert, Phys. Rev. Lett. 50, 2106 (1983);
M. D. Levenson, IEEE J. Quant. Electron. QE-10, 110 (1974).

27. N. Bloembergen and P. S. Pershan, Phys. Rev. 128, 606 (1962);
T. F. Heinz, Ph. D. thesis, University of California, Berkeley (1982).

28. For liquid deposition techniques, see, for example, P. K. Hansma and R. V. Coleman, Science 184, 1369 (1974);
P. K. Hansma, Phys. Rep. 30, 145 (1977);
J. P. Heritage and D. L. Allara, Chem. Phys. Lett. 74, 507 (1980);
J. T. Hall and P. K. Hansma, Surf. Sci. 71, 1 (1978).

29. K. B. Widers, V. A. Walters, K. N. Wang, and S. D. Colson, J. Phys. Chem. 88, 6067 (1984);
A. Campion and D. R. Mullins, in *Surface Studies with lasers*, edited by F. R. Aussenegg, A. Leitner, and M. E. Lippitsch (Springer, Berlin, 1983), p. 36.

30. A. Gaupp, Free Electron Laser, CERN [Rep.], CERN 89-01, Proc, - CAS, CERN Accel. Sch. Adv. Accel. Phys. Course, 2nd, 207 (1987);
D. D. Dlott and M. D. Fayer, J. Opt. Soc. Am. B: *Opt. Phys.* 6, 977 (1989);
J. Ristein, B. Hooper, and P. C. Taylor, J. Opt. Soc. Am. B: Opt. Phys. 6, 1003 (1989);
N. J. Tro, D. A. Arthur, and S. M. George, J. Opt. Soc. Am. B: *Opt. Phys.* 6, 995 (1989);
W. S. Fann, S. Benson, J. M. J. Madey, S. Etemad, G. L. Baker, and F. Kajzar, Phys. Rev. Lett. 62, 1492 (1989).

Table I. Fitting parameters characterizing the observed vibrational resonances of coumarin 504 molecules on fused silica substrate in the optical infrared-visible sum-frequency generation spectrum. ($N_s = 2.0 \times 10^{14}$ /cm^2)

Mode frequency $\omega_{\delta 0}$ (cm^{-1}) (solid)	Halfwidth Γ_δ (cm^{-1}) (solid)	Mode frequency ω_δ (cm^{-1}) (surface)	Resonant nonlinear polarizability $\alpha_\delta^{(2)} = A_\delta/\Gamma_\delta$ (10^{-29} esu)	Resonant surface susceptibility $\chi_\delta^{(2)} = N_s\alpha_\delta^{(2)}$ (10^{-14} esu)
922	6	(918)*	(7.0 ± 1.0)*	(1.4 ± 0.2)*
948	6	951	3.0 ± 0.5	0.6 ± 0.1
1050	4	1039	8.9 ± 1.0	1.8 ± 0.2
1078	5	(1074)*	(5.1 ± 2.0)*	(1.0 ± 0.4)*
1090	5	(1087)*	(10.2 ± 3.0)*	(2.0 ± 0.6)*
nonresonant	background	------	11.6 ± 1.0	2.3 ± 0.2

* The numbers in the parentheses are less accurate since they were deduced from resonance peaks appearing outside the laser tuning range.

Table II. Effective surface nonlinear susceptibilities of a few materials at the sum-frequency ω_3 with two pump beams at 0.532 μm and 9.57 μm:

Materials (in air)	$\chi_{yzy,\,eff}(\omega_3)$ (10^{-14} esu)
coumarin 504	1.8
pyridine	0.36
Ge(100)	77
Si(111)	6.3
Ni(100)	≤ 0.7
Cu(100)	1.0
Gold mirror	≤ 0.77

Figure captions:

Fig. 1 Molecular structure of a coumarin 504 molecule and the energy diagram of the first electronic transition.

Fig. 2 Schematic diagram of the experimental set-up for surface infrared-visible sum-frequency and difference frequency generation. The sample is a monolayer of coumarin 504 dye
molecules which is spin-coated on a fused silica substrate.

Fig. 3 Visible absorption spectrum of coumarin 504 molecules in ethanol.

Fig. 4(a) Infrared absorption spectrum of solid coumarin 504.

Fig. 4(b) Raman scattering spectrum of solid coumarin 504. The wavelength of the pump beam is at 6471 Å.

Fig. 5 Sum-frequency vibrational spectrum of a monolayer of coumarin 504 molecules on fused silica. The square of the measured molecular sum-frequency polarizability is plotted against the wavenumber of the infrared laser frequency.

Fig. 6 Normalized infrared absorption spectra of coumarin 504 (solid line) and pyridine (dashed line) in CCl_3H.

Fig. 7 Normalized Raman scattering spectra of coumarin 504 (solid line) and pyridine (dashed line). The absolute magnitude of Raman intensity for pyridine is magnified by a factor of 10 as indicated in the figure.

Coumarin 504

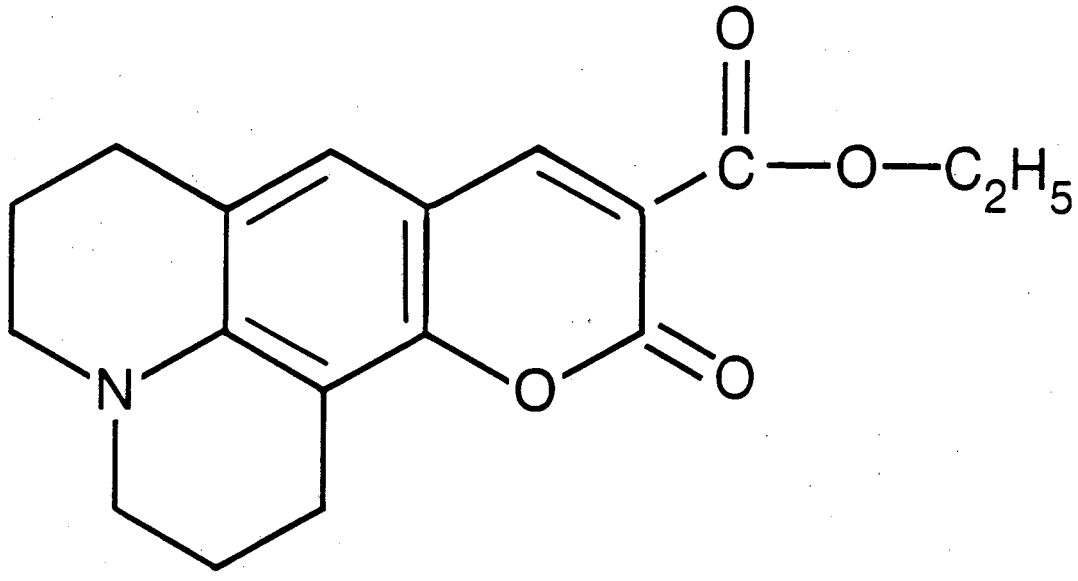

XBL 895-5118

Fig. 1

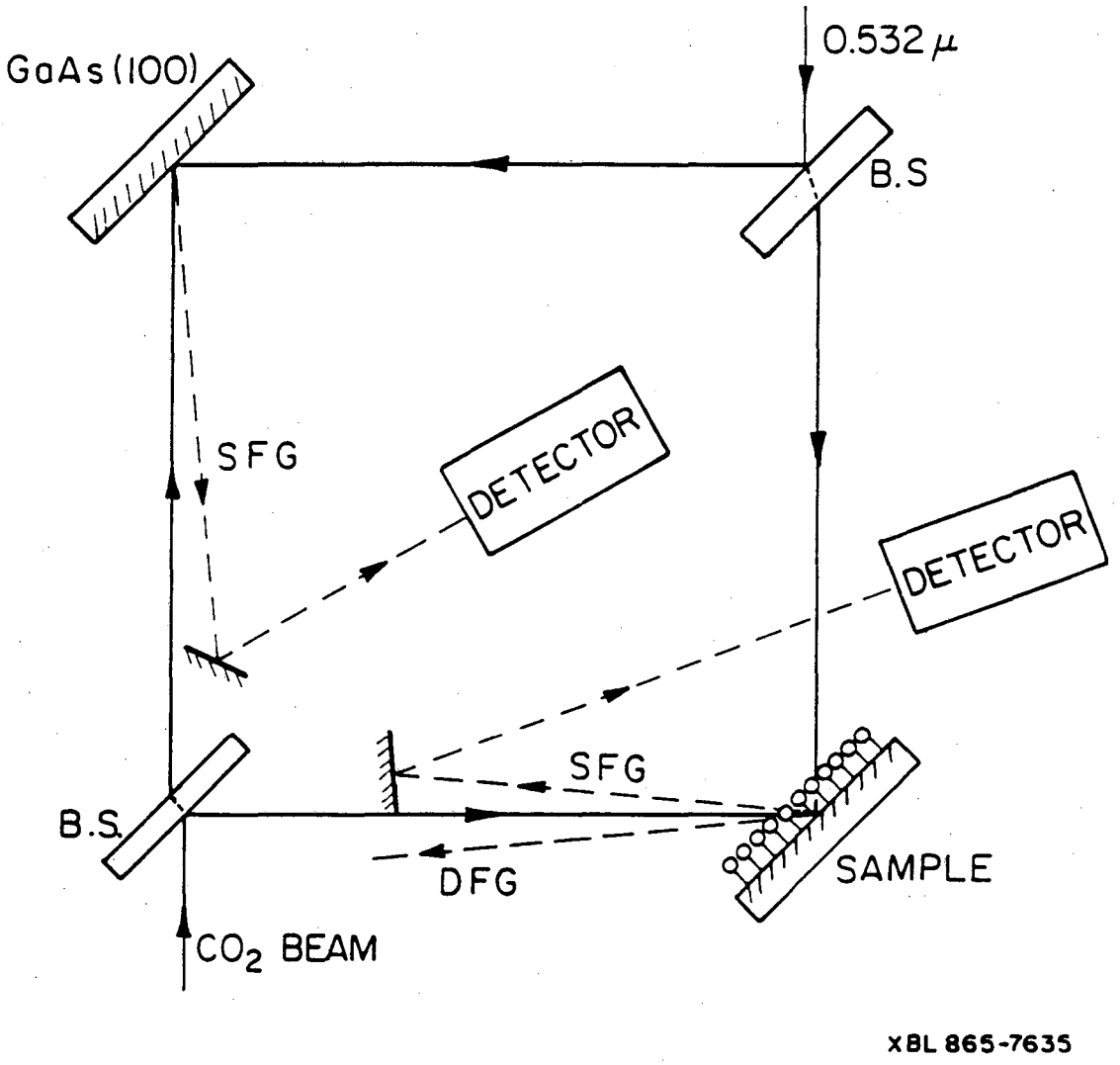
GaAs (100)
0.532 μ
B.S
SFG
DETECTOR
DETECTOR
SFG
B.S.
DFG
SAMPLE
CO2 BEAM
XBL 865-7635

Fig. 2

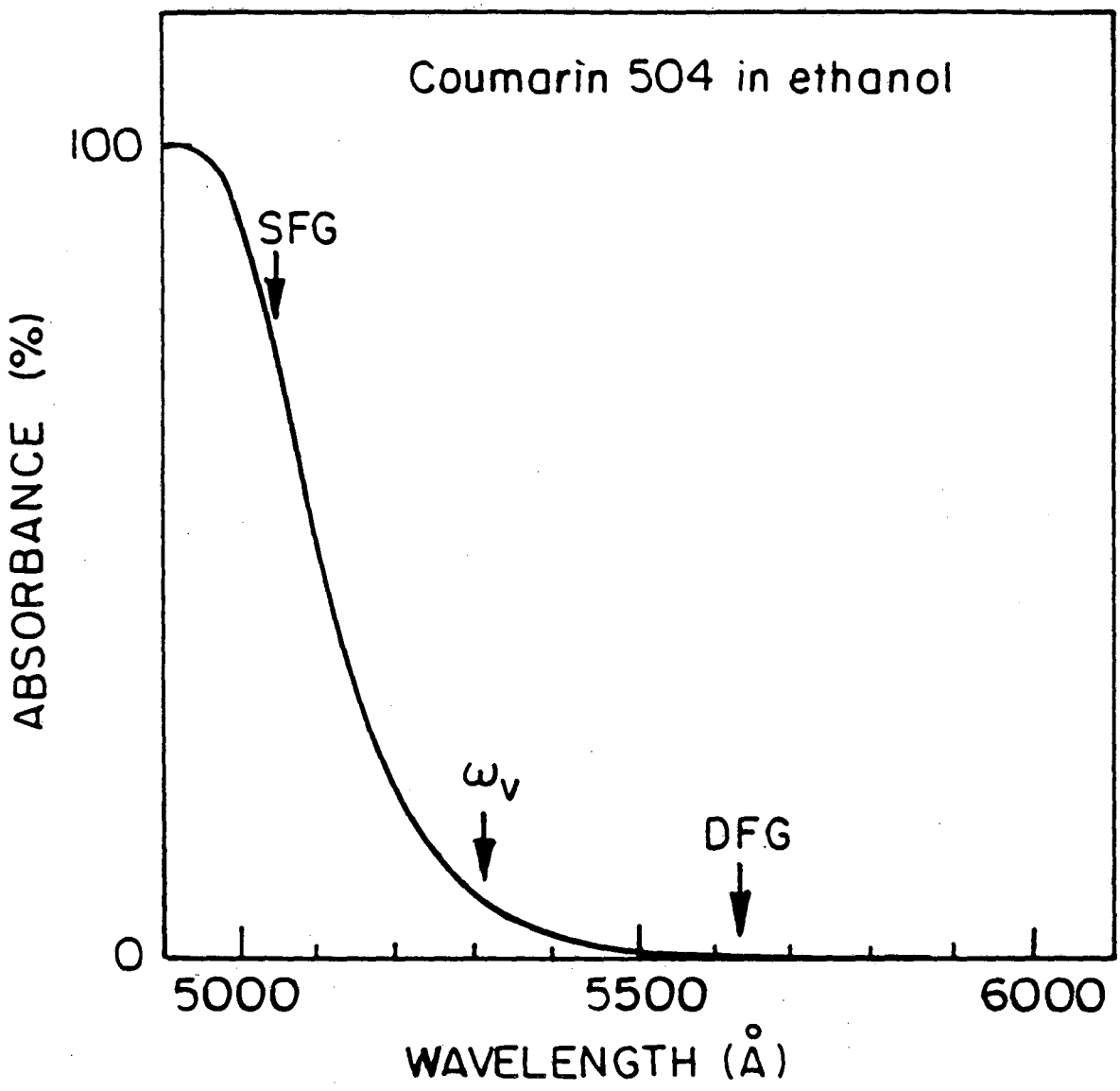

XBL 865-7638

Fig. 3

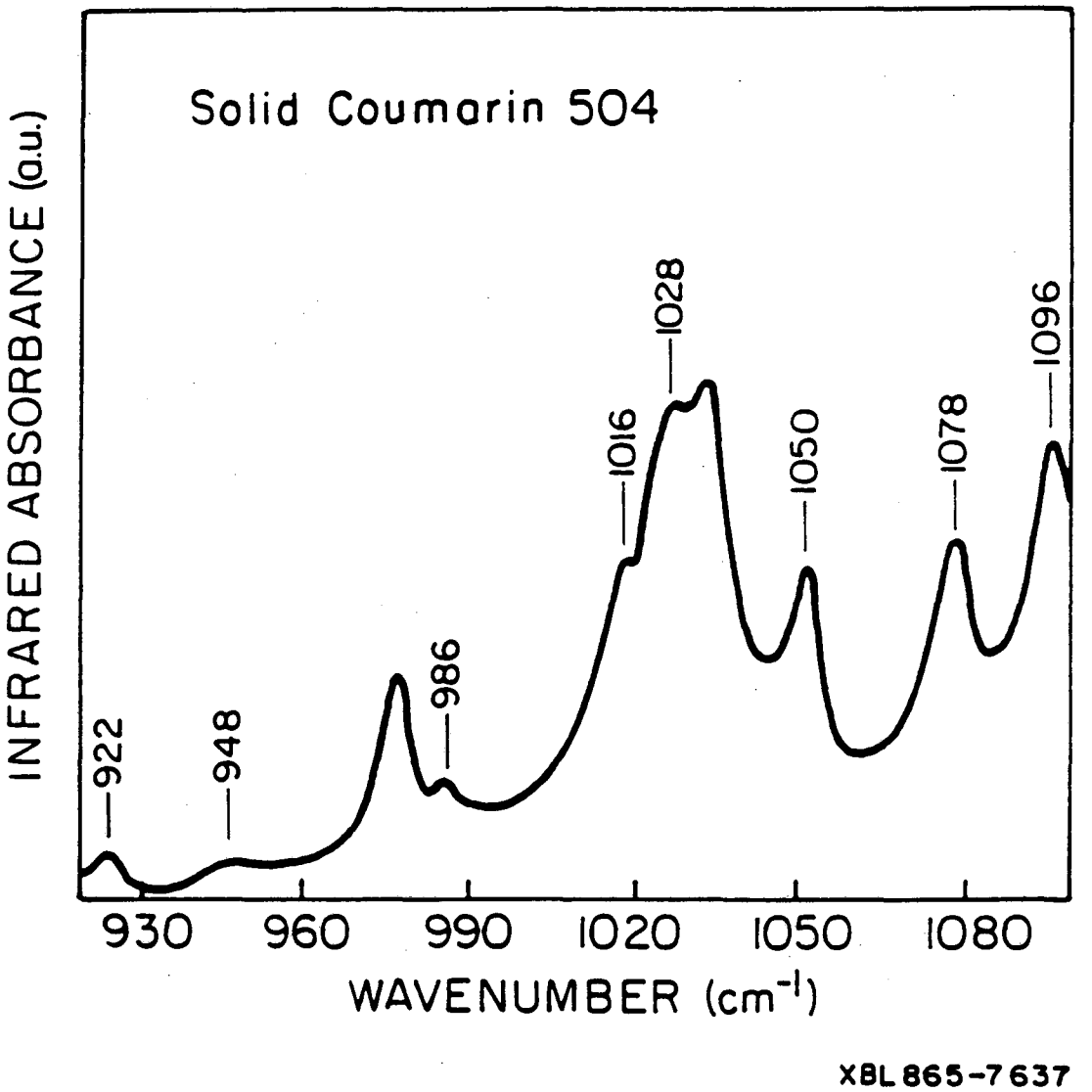
Solid Coumarin 504
INFRARED ABSORBANCE (a.u.)
922
948
986
1016
1028
1050
1078
1096
930
960
990
1020
1050
1080
WAVENUMBER (cm⁻¹)
XBL 865-7637

Fig. 4(a)

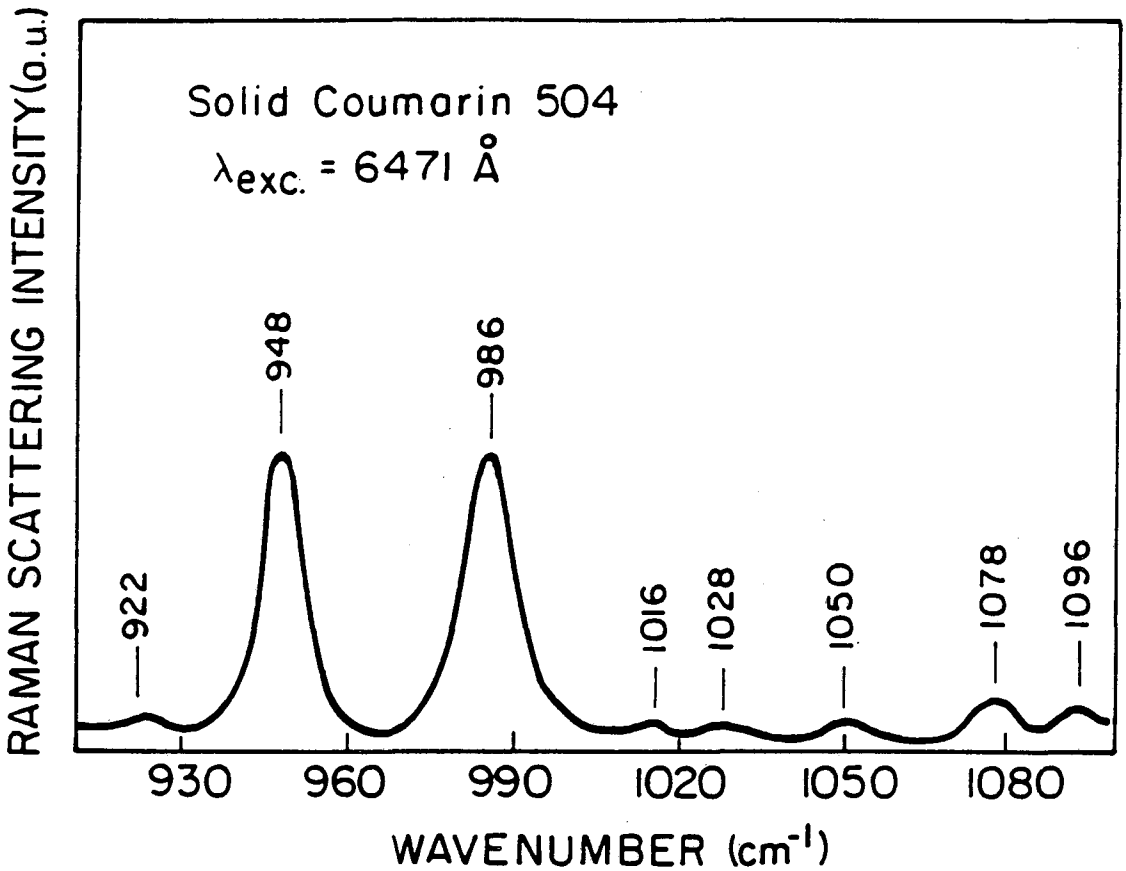

XBL 865-7636

Fig. 4(b)

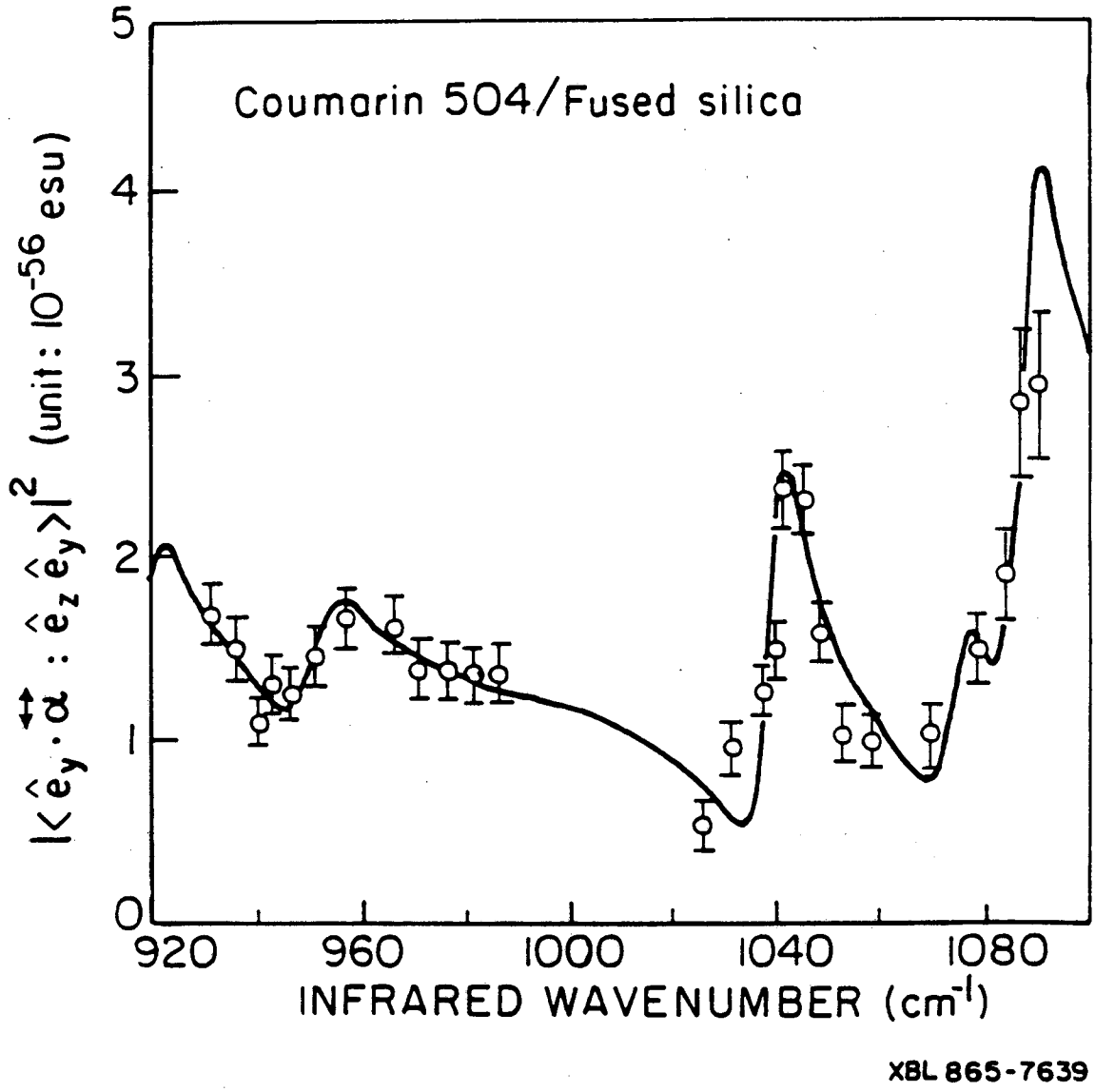
Coumarin 504/Fused silica
$|\langle \hat{e}_y \cdot \overleftrightarrow{\alpha} : \hat{e}_z \hat{e}_y \rangle|^2$ (unit: 10^{-56} esu)
0
1
2
3
4
5
920
960
1000
1040
1080
INFRARED WAVENUMBER (cm^{-1})
XBL 865-7639

Fig. 5

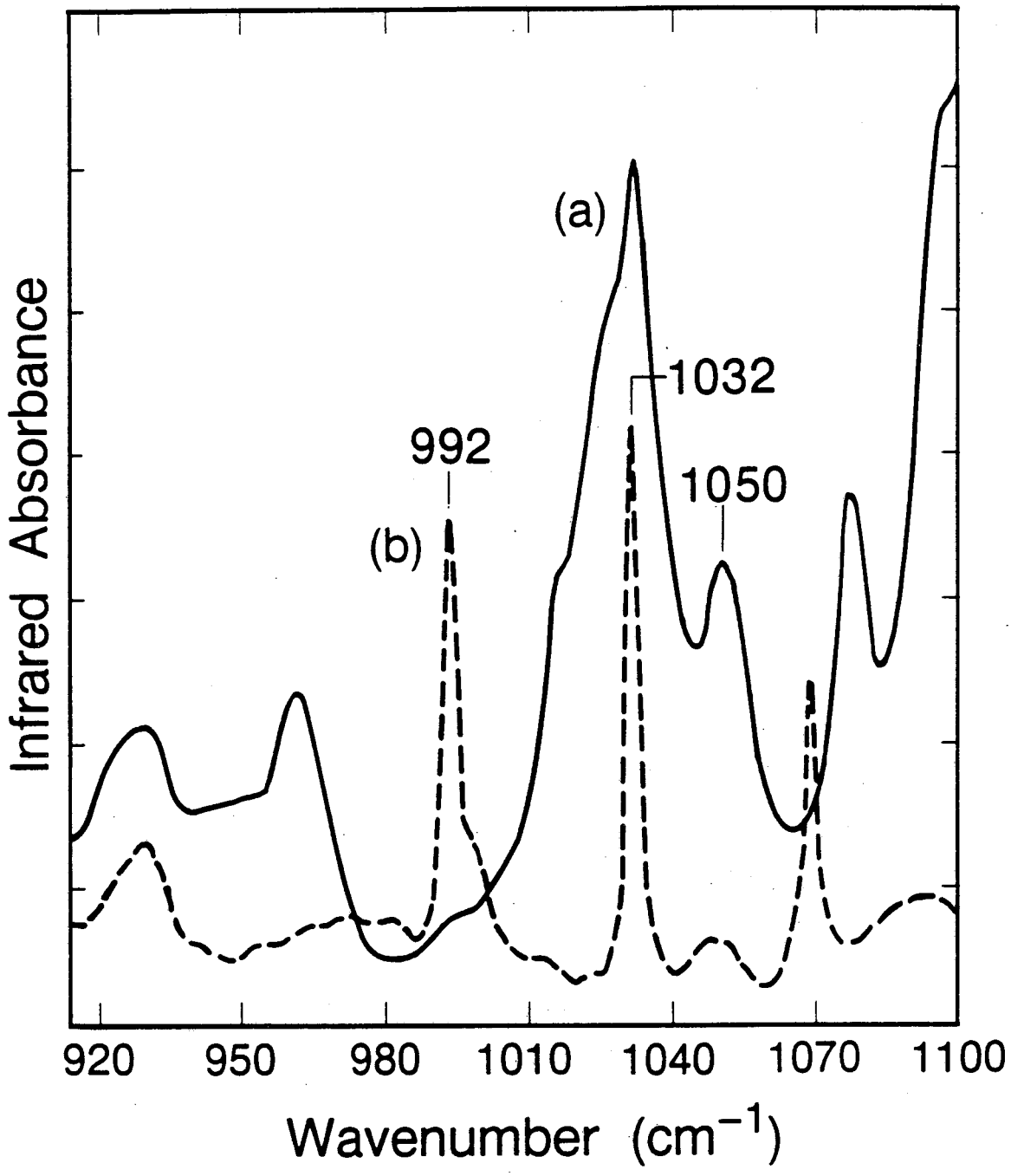

XBL 895-5120

Fig. 6

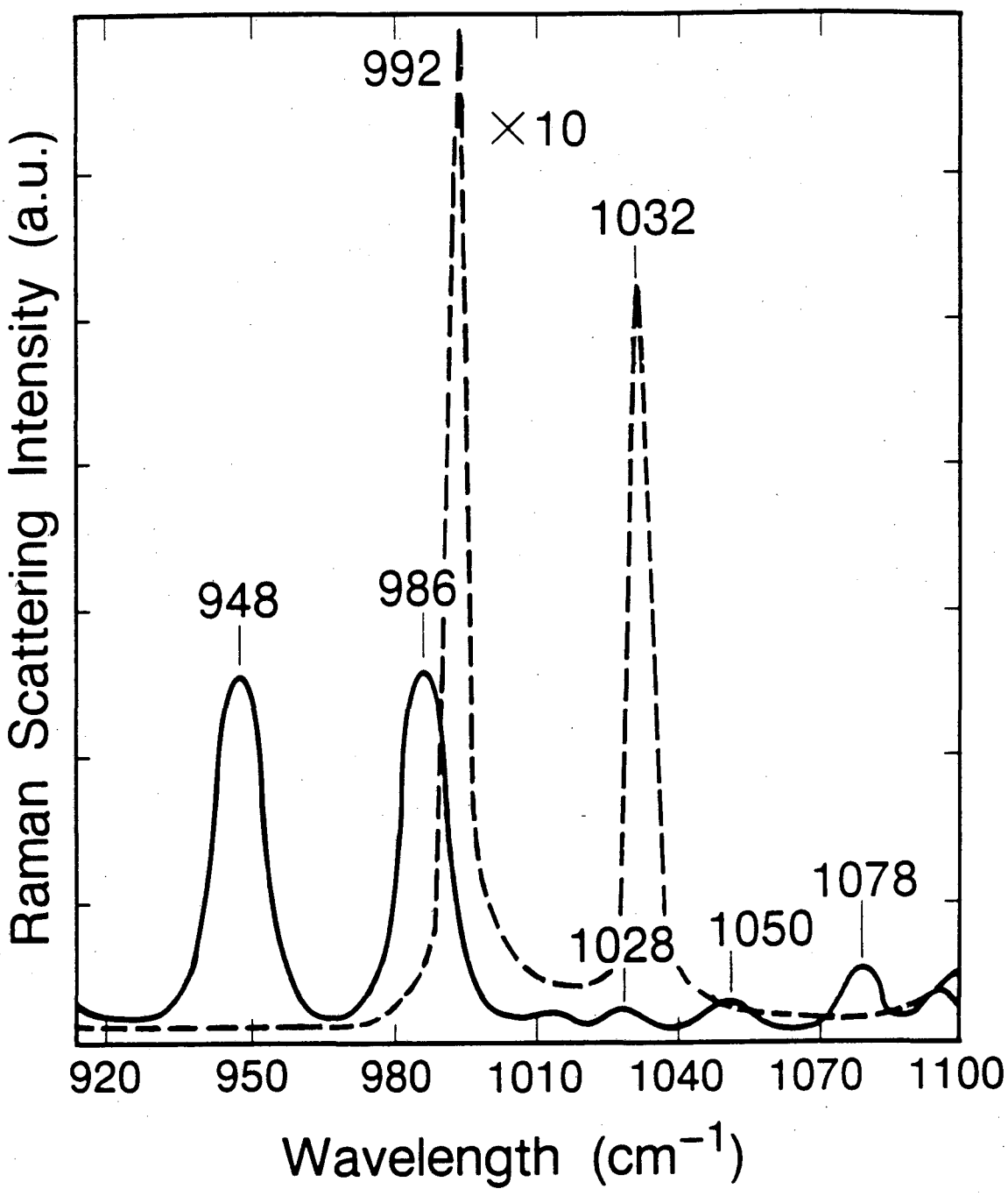

XBL 895-5122

Fig. 7

IV. Transient Surface Vibrational Excitations and Their Detection

A. Introduction

In this chapter, we explore the possibility of exciting and detecting coherent transients of vibrational resonances at surfaces. Relaxations of various excitations on surfaces are important subjects in surface science. The rates and pathways of energy exchange and coherent phase relaxations at surfaces play crucial roles in almost every surface dynamic processes.[1, 2] Particularly, dynamics of transient surface vibrational excitations have drawn considerable research effort over the past two decades.[3 - 14] These efforts are understandably accompanied by the technological progress and sophistication of experimental techniques in this area. A number of spectroscopic techniques using quasi-monochromatic electrons, massive particles, coherent and incoherent light sources are developed. The spectroscopic data enable one to learn much information on the chemical states of adsorbates and their dependence on substrates, the sites of adsorption and the presence of neighboring adsorbed particles. Conventional surface sensitive vibrational spectroscopy techniques such as high-resolution electron energy loss spectroscopy (HREELS), inelastic electron tunneling spectroscopy (IETS), infrared reflection-absorption spectroscopy (IRAS), Fourier transform infrared spectroscopy (FTIR),[6, 7] photo-acoustic spectroscopy (PAS) [8, 9] and infrared emission spectroscopy [10] are often restricted to measurements in the frequency domain. There are strong theoretical efforts to understand relaxation processes at surfaces. Some of them are devoted to correlate relaxation models to the experimentally measured spectral lineshapes.[5, 7, 13, 14] Due to the presence of inhomogeneous spectral broadening and the complexity of relaxation mechanisms, only on special occasions can some conclusions be drawn on the nature of vibrational relaxation

processes based on these frequency domain measurements and analysis. Furthermore, it is known that the relaxation of vibrational excitations on surfaces occur at a time scale of picoseconds to subpicosecond.[5, 7, 12, 13] As most of the frequency domain measurements are conducted over a time scale longer than milliseconds,[15, 16] information on the vibrational relaxation intermediates or transients are usually lost or difficult to extract.

Obviously, spectroscopic techniques capable of probing vibrational transients at surfaces in real time are desirable. In the past few years, a number of experiments have been reported in which pump-and-probe techniques with picosecond coherent infrared laser pulses were used to investigate the population relaxations of adsorbates.[12] In these experiments, the initial infrared pulse is used to populate the excited vibrational state, and the subsequent infrared pulse with much weaker power is applied at a delayed time to probe the recovery of the ground-state population due to population or energy relaxation of the excited state. If there are no bottleneck states to which the excitation energy can be transferred, such a ground-state recovery measurement can directly yield the rate of the energy relaxation of the excited vibrational state. In order to obtain adequate signal-to-background ratio, samples with high surface-to-bulk ratio were used. These sample preparation methods are adequate only under special circumstances due to their general lack of characterization. Naturally, one would like to apply the same pump-and-probe technique to well-defined single crystalline surfaces.[1] However, even under most favorable conditions such as by working with molecules with large dynamic dipole moments like carbon monoxide CO or nitrite NO and exploiting grazing-incidence geometry to cover large number of adsorbates, only a few percent of the reflected infrared light are absorbed by the adsorbates in a single pass.[3] The relaxation measurements then require infrared laser sources with ultrashort pulsewidths for the desired time resolution, high powers for the induction of sufficient ground-state population changes, and finally stable outputs to enable effective background subtraction and signal normalization. Optical damages may

also impose a limitation on the technique. So far, this technique has not yet been demonstrated on well-defined metal or semiconductor surfaces.

In principle, transient vibrational spectroscopy using infrared photon-echoes can offer an effective way to study vibrational relaxations on a surface in real time.[17 - 19] Although it has not been demonstrated experimentally on a surface, the technique has been widely applied to bulk samples. It has a number of attractive features: it can effectively separate the effects of population relaxations, dephasing, and inhomogeneous broadening. Typical relaxation times in metals or semiconductors are of the order of a few hundred femtoseconds which are short compared to the typical vibrational relaxation times of adsorbates on surfaces in the range of picoseconds.[20] Therefore, surface IR photon-echo measurement can be made free of the large background from the substrate bulk. If we use *in situ* infrared-visible sum-frequency generation to up-convert the infrared photon echoes, suppression of the background from the bulk can be achieved even more effectively from our discussion in the previous chapters.[21 - 24]

Since the pioneering work of Abella et al in 1966,[17] photon-echoes have been routinely used as an effective tool in the investigation of relaxations of vibrational and electronic resonances in bulk samples such as gases, liquids and solids. Generally speaking, they are particularly effective for separating homogeneous relaxation processes such as population relaxations and coherent phase decays from often overwhelming inhomogeneous broadening.

However, extending the photon-echo technique to studies of surface vibrational resonances is not as straightforward. This arises mainly from the fact that much reduced signal strengths are generally expected, and at the same time, available laser sources and detection schemes are limited. As the typical vibrational relaxation times at surfaces are on the order of picoseconds, picosecond and even subpicosecond coherent light sources are required. In addition, in order to induce substantial population or coherent phase changes,

peak laser power densities of a few GW/cm^2 are needed (see, for example, the discussion in Section B.4.). These requirements have been major limiting factors to the application of photon-echo spectroscopy to surfaces. Furthermore, because of the small number of adsorbates involved in the interaction with the radiation fields,[25] and the small portion of the stored energy in a vibrationally excited adsorbate is reemitted coherently as a result of the energy loss to the substrate,[26] very weak photon echo signals are expected, and elaborate detection systems are required.

In this chapter, we will present some of basic ideas and derivation of surface infrared photon-echoes generated in a monolayer of vibrationally excited adsorbates. Based on attainable laser technology and detection technology, we propose a few surface photo-echo detection schemes, and discuss their efficiencies and the practical considerations in their implementation.

B. Theoretical considerations

1. *General description of surface vibrational excitations and surface infrared photon echoes*

As pointed out in the previous section, we are interested in investigating population and coherent phase relaxations of vibrational excitations at surfaces. In principle, by selective excitation and probing, the transient vibrational spectroscopy using surface infrared photon echoes should enable us to study these processes separately in real time. The fundamental principle of photon echoes was elegantly founded in the early work of Kurnit et al and R. P. Feynman et al.[17, 27] More explicit and extensive discussions were presented later by Abella et al.[17] and for stimulated photon-echoes by Mossberg et al..[18] The idea is easily understood for an ensemble of two-level systems. The wavefunction for

a two-level system which is weakly coupled to the rest of the ensemble can be written

$$\psi(t) = a(t)\psi_a + b(t)\psi_b \,, \tag{1}$$

$$|\, a(t) \,|^2 + |\, b(t) \,|^2 = 1, \tag{2}$$

where ψ_a and ψ_b are the two eigenstates of the Hamiltonian for the two-level system corresponding to the upper level and lower level, respectively. As it suffices to specify a state of a two-level system with two independent parameters, for example, the population difference of the two levels, $|\, a(t) \,|^2 - |\, b(t) \,|^2$, and the relative phase angle, $\Delta\phi$, between a(t) and b(t), Feynman et al. [27] showed that the quantum mechanical state of the system can be equivalently described with a unit 3-vector, $\mathbf{r}(t) = r_1\mathbf{e}_1 + r_2\mathbf{e}_2 + r_3\mathbf{e}_3$. By defining the projection of the vector, r_3, on the z-axis to be the population difference of the two levels and the azimuthal angle in the x-y plane to be the relative phase angle, $\Delta\phi$, it is easily found that the Schrödinger's equation for $\psi(t)$ in Eq. (1) can be transformed into

$$\frac{d\mathbf{r}}{dt} = \omega \times \mathbf{r} \,, \tag{3}$$

where ω is also a 3-vector and defined as

$$\begin{aligned} \omega_x &= 2\,\pi\,(\,V_{ab} + V_{ba}\,)\,/\,h\,, \\ \omega_y &= 2\,\pi\,i\,\,(\,V_{ab} - V_{ba}\,)\,/\,h\,, \\ \omega_z &= 2\,\pi\,(\,E_a - E_b\,)\,/\,h\,. \end{aligned} \tag{4}$$

V_{ab} and V_{ba} are the matrix elements of the perturbation Hamiltonian. E_a and E_b are the eigenvalues of the unperturbed Hamiltonian for the two levels. The interactions of the two-

level system with its surroundings including other members of the ensemble can be included into Eq. (3) in forms of relaxation terms, after the ensemble average, [27, 17]

$$\frac{d\mathbf{r}}{dt} = \omega \times \mathbf{r} - \frac{r_1\,\mathbf{e}_1 + r_2\,\mathbf{e}_2}{T_2} - \frac{(1 + r_3)\,\mathbf{e}_3}{T_1} \,. \tag{5}$$

T_2 and T_1 are known as the apparent dephasing time and population relaxation time separately. In order to link the theoretical description to experimental observation, we commonly evaluate the induced electric dipole moment which is measurable experimentally,

$$\mathbf{p}(t) = \langle \psi(t) \mid e\,\mathbf{r} \mid \psi(t) \rangle = \langle \psi_a \mid e\,\mathbf{r} \mid \psi_b \rangle\, r_1(t) \,. \tag{6}$$

If the perturbation is caused by an optical field, the induced electric dipole moment is the material response which is responsible for absorption and reemission. The material relaxations are reflected in the temporal evolution of $\mathbf{p}(t)$ or $r_1(t)$.

The form of Eq. (3) and (5) are identical to that of a magnetic dipole with a spin of one-half in a magnetic field.[28] In the presence of time-varying perturbations, a two-level system should hence behave similarly as a magnetic dipole in time-varying magnetic field. This means that the dynamic behaviors and many concepts developed for a magnetic dipole in a magnetic field should have their counterparts in a two-level system. It is this analogy which led Abella and Hartmann to discover the photon echoes which correspond to the well-known spin echoes discovered in NMR and ESR experiments in early 1950's.[28] More recently, Ye and Shen have approached the photon echo phenomena from a more general consideration.[19] In their formulation, instead of using a 3-vector, the density matrix, $\rho(t)$, is followed in time under the influence of a perturbing field. They found that the photon echoes are simply special cases of more general transient four-wave mixing.

For example, a three-pulse photon echo process can be seen as a wave mixing of the three resonant input fields and the radiative echo field, while a two-pulse photon echo process can be treated as a special case of such a four-wave mixing with the second and the third waves coincide in time and in frequency. The four-wave mixing output is governed by the third-order nonlinear polarization which is related to the third-order density matrix $\rho^{(3)}(\omega)$ as

$$\mathbf{P}^{(3)}(\omega) = \mathrm{Tr}\left[-\mathbf{e}\,\mathbf{r}\,\rho^{(3)}(\omega) \right] . \tag{7}$$

For an ensemble of non-interacting two-level systems, we can understand the equivalency of the two descriptions of photon echo phenomena from the following simple argument. First of all, Eq. (7) is simplified as

$$\mathbf{P}^{(3)}(\omega) = -\sum_{\delta} < \psi_a^{\delta} \mid \mathbf{e}\,\mathbf{r} \mid \psi_b^{\delta} > \left[< \psi_a^{\delta} \mid \rho_{\delta}^{(3)}(\omega) \mid \psi_b^{\delta} > + < \psi_b^{\delta} \mid \rho_{\delta}^{(3)}(\omega) \mid \psi_a^{\delta} > \right] , \tag{8}$$

where for convenience, we have assumed that the matrix element of the dipole moment operator, **er**, is a real 3-vector. The summation is carried out over the entire ensemble. For a third-order process, three propagators are required to propagate the initial state ψ_b to the final state ψ_a or *vice versa*. Only one combination of these propagators for each term in Eq. (8) leads to the nonlinear polarization which is responsible for forward coherent stimulated photon echoes. For example, starting from the initial density matrix, $\mid \psi_b > \rho^{(0)}(0) < \psi_b \mid$, the three propagators are as follows: the first one corresponds to absorption of a photon at ω on the right side ($-\mathbf{k}_1$), then the resultant density matrix of the form $\mid \psi_b > < \psi_a \mid$ evolves from t_1 to t_2,

$$p_1 = |\psi_b\rangle \int (V_1^*)_{ba} dt \exp[+i(\omega_a - \omega_b)(t_2 - t_1) + i(-\mathbf{k}_1)\cdot \mathbf{x}] \langle\psi_a| ; \quad (9)$$

the second one corresponds to absorption of a photon at ω on the left side ($\mathbf{k}_2$), the resultant density matrix of the form $|\psi_a\rangle\langle\psi_a|$ evolves from t_2 to t_3,

$$p_2 = |\psi_a\rangle \int (V_2)_{ab} dt \exp[-i(\omega_a - \omega_a)(t_3 - t_2) + i\mathbf{k}_2\cdot \mathbf{x}] \langle\psi_b| ; \quad (10)$$

the third one corresponds to emission of a photon at ω on the right side ($\mathbf{k}_3$), then the density matrix of the form $|\psi_a\rangle\langle\psi_b|$ evolves from t_3 to t,

$$p_3 = |\psi_a\rangle \int (V_3)_{ab} dt \exp[-i(\omega_a - \omega_b)(t - t_3) + i\mathbf{k}_3\cdot \mathbf{x}] \langle\psi_b| . \quad (11)$$

t_n is the arrival time of the n-th excitation pulse. The third-order matrix element for the forward coherent stimulated photon echo is then given by

$$\langle\psi_a| p_2 |\psi_b\rangle \rho^{(0)}(0) \langle\psi_b| p_1 p_3 |\psi_b\rangle, \quad (12)$$

which is proportional to

$$\exp\{i(\mathbf{k}_3 + \mathbf{k}_2 - \mathbf{k}_1)\cdot \mathbf{x} - i\omega t - i[(\omega_a - \omega_b) - \omega][(t - t_3) - (t_2 - t_1)]\}. \quad (13)$$

When $t - t_3 = t_2 - t_1$, the time-dependent phase factor in Eq. (13) equals to $-i\omega t$ which is independent of $(\omega_a - \omega_b)$, and from Eq. (12) and (8), a rephased echo polarization is formed. The well-known two-pulse photon echoes are derived if the first half of the original second pulse is used as the $\mathbf{k}_2$-pulse and the second half as the $\mathbf{k}_3$-pulse. One of the most important developments made by Ye and Shen is that they generalize the concept

of photon echoes to other transient optical phenomena and extend them to systems which are no longer characterized by merely two levels.

These general results are applicable to coherent excitations of resonances at surfaces. For our purpose, we will focus our discussion on surface vibrational resonances. We first note that, due to the large anharmonicities of vibrational potential energy surfaces, it is usually a good approximation to treat each molecular vibrational mode as a two-level system. Secondly, as surface vibrational excitations are confined in a two-dimensional plane, the coherent radiation from these excitations are required to be phase-matched only for the in-plane components of the wave vectors.[29, 17] For example, for a two-pulse photon echoes generated at a surface, assuming that **n** is a unit vector along the surface normal and **k** is the wave vector of the output wave, the phase matching condition is written

$$\mathbf{n} \times (\mathbf{k} - 2\mathbf{k}_2 + \mathbf{k}_1) = 0. \tag{14}$$

Next, we briefly review the results of the theoretical calculation of surface vibrational excitations and the subsequent coherent reemission from the above general description. Then we discuss different detection schemes and related subjects in Section C. Since the 3-vector model for an ensemble of two-level systems is a convenient description for the physical understanding, we will follow that description.

2. *Surface vibrational excitations with no inhomogeneous broadening*

One of the examples of such a kind of systems can be an ensemble of adsorbed molecules which only occupy one type of surface sites on a surface of a single crystalline substrate. In these cases, one would like to separately determine the rates of the population

relaxation and the pure coherence dephasing of a vibrational resonance of adsorbates. Both processes contribute to the spectral linewidth, Γ, which is usually obtained in a frequency-domain measurement. It is well-known that the apparent dephasing rate, $\Gamma = 1 / T_2$, is related to these two relaxation processes by [13]

$$\Gamma = \frac{1}{T_2^*} + \frac{1}{2\,T_1} \; . \tag{15}$$

T_2^* is the pure dephasing time of the coherent excitation. The key advantage of conducting transient measurements is that one probes the system before it reaches the steady state so that different relaxation processes may be separately examined. A separate determination of the population relaxation can be achieved by a two-pulse pump-and-probe experiment (or, transient saturation spectroscopy), for example.[12] In this case, the first infrared pulse is applied to populate the excited vibrational state in a resonant optical pumping. Subsequently, the population of the excited state decays and the population difference of the two levels, $\beta(t)$, recovers back to the state of the thermal equilibrium at a rate, $1 / T_1$,

$$\beta(\tau) \propto \sin^2(\theta_{p1}/2) \exp(-\tau / T_1) \, , \tag{16}$$

where T_1 is known as the population relaxation time. θ_{p1} is the pulse-angle of the pump pulse,and is defined as [17]

$$\theta_p = \frac{2\,\pi\,\mu_{ab}}{h} \int_{-\infty}^{+\infty} E_{ab}^{I}(\omega_{IR}, t)\, dt \; . \tag{17}$$

The integrand is the projection of the electric field $\mathbf{E}^I(\omega_{IR}, t)$ of the pump pulse along the

direction of the induced dipole moment, $< \psi_a | \mathbf{er} | \psi_b >$, and $\mu_{ab} = | < \psi_a | \mathbf{er} | \psi_b > |$. $\beta(t)$ can be probed by measuring the absorption of a second pulse propagating in a different direction at a delayed time τ. Thus, by monitoring $\beta(\tau)$ as a function of delay time τ, one can deduce the population relaxation time T_1. The pure dephasing rate can then be obtained from Eq. (15). Such an experiment has been first attempted recently by Harris et al. in which they studied the population relaxation of the CH_3 stretching vibration in a monolayer Langmuir-Blodgett film.[30]

3. *Surface vibrational excitations with inhomogeneous broadening*

Majority of vibrational excitations at surfaces are subject to inhomogeneously broadening. This is mainly attributed to the chemical shifts in frequencies of the vibrational resonances of adsorbed molecules seating at different surface sites.[1, 31] The contribution of inhomogeneous broadening to a vibrational spectral linewidth obtained in a steady-state or frequency-domain measurement is not easily resolved. It is important to point out that the deduction of population relaxation rates from the pump-and-probe measurements is not affected by the presence of inhomogeneous broadening. Hence one can obtain T_1 without any additional experimental rearrangement. If we are to study the pure dephasing rate, $1/T_2^*$, however, the effect of inhomogeneous broadening has to be eliminated or at least determined. This can be achieved for example, by using the two-pulse photon echo technique which are frequently used in the studies of relaxations of material excitations in bulk samples.[17, 18]

Following the description of the 3-vector model and the analogy to the generation of a two-pulse magnetic spin echo, we know that the first coherent infrared pulse resonantly excites a selected vibrational mode of an ensemble of adsorbates and rotates the 3-vectors of the ensemble into the $\mathbf{e}_1$ - $\mathbf{e}_2$ plane. The amplitude of the excitation is measured by the

projection of the 3-vector in the plane and hence is proportional to $\sin\theta_{p1}$. Subsequently, the phase angle $\Delta\phi$ of the coherent excitation for each adsorbate or equivalently, the azimuthal angle of the corresponding 3-vector in the $\mathbf{e}_2$ - $\mathbf{e}_2$ plane evolves at its own characteristic resonance frequency which can be different from other members of the ensemble, and as a result, the projections of the 3-vectors of the ensemble become out of phase with each other. In addition, $\Delta\phi$ is also subject to random changes caused by the residual time-dependent interactions which lead to the homogeneous spectral linewidth Γ. The differences in the resonance frequencies among the adsorbates, also known as the inhomogeneous broadening, contribute to the apparent dephasing rate or apparent spectral linewidth of the vibrational resonance after the ensemble average. After a delayed time τ, the second pulse is applied to rotate the dephased 3-vectors in the $\mathbf{e}_2$ - $\mathbf{e}_2$ plane by 180°. This is achieved by rotating the vectors by 90° into $\mathbf{e}_3$ with a front portion of the pulse, and then by another 90° into the $\mathbf{e}_2$ - $\mathbf{e}_2$ plane with the rest part of the pulse. Since the overall amplitude is proportional to the product of sines of the pulse-angles of the two steps, it should choose the optimum case, $\sin(\theta_{p2}/2)\sin(\theta_{p2}/2) = \sin^2(\theta_{p2}/2)$. Afterward, the rotated 3-vectors in the $\mathbf{e}_2$ - $\mathbf{e}_2$ plane continue to evolve at their individual characteristic frequencies but now with additional "initial" phases. As a result of a 180° rotation, the additional phase, $\Delta\phi_0 = \omega_{ab}\,\tau$, is positive in sign, and equal to the phase lag, $-\,\omega_{ab}\,\tau$, of the excitation between the two pump pulses. Therefore, at the time τ after the second pulse, these 3-vectors overlap again in the $\mathbf{e}_2$ - $\mathbf{e}_2$ plane and form a rephased echo, except for those of the excited adsorbates which have experienced random phase changes or population decay. The latter contribute to a homogeneous decay of the rephased echo. From the above analysis, the rephased excitation of the ensemble should have an amplitude

$$r_1(t) = \frac{1}{2}\sin\theta_{p1}\,\sin^2(\theta_{p2}/2)\exp[\,i\,(2k_{2x} - k_{1x})\cdot x - i\,\omega_{IR}\cdot t\,]\exp(-2\Gamma\cdot\tau)\,. \tag{18}$$

The decay of $r_1(t)$ with the pulse separation τ is only determined by the effect of the random phase changes and population relaxation after the ensemble average and is equal to the homogeneous linewidth 2Γ. We will discuss the detection of the rephased echo in Section B.4. and Section C.

It is also possible to obtain population relaxation rates by using three-pulse stimulated photon-echo techniques. In this case, the second pump pulse only rotates the dephased 3-vectors in the $\mathbf{e}_2$ - $\mathbf{e}_2$ plane initially induced by the first pump pulse into $\mathbf{e}_3$. The amplitude is then proportional to $\sin(\theta_{p1})\sin(\theta_{p2})\exp(-\Gamma\tau)$, where τ is the separation of the first two pulses. At a delayed time τ_{23} after the second pulse, a third pulse is applied to rotate these vectors by another 90° into the $\mathbf{e}_2$ - $\mathbf{e}_2$ plane. At a time τ after the third pulse, the dephased vectors are rephased and form a three-pulse stimulated photon echo. The amplitude of the echo is given as

$$r_1(t) = \frac{1}{2}\sin\theta_{p1}\sin\theta_{p2}\sin\theta_{p3}\exp[\,i\,(k_{3x}+k_{2x}-k_{1x})\cdot x - i\,\omega_{IR}\cdot t\,]\exp[-\frac{\tau_{23}}{T_1} - 2\Gamma\cdot\tau\,]. \tag{19}$$

It is reduced by an additional factor, $\exp(-\tau_{23}/T_1)$ due to the population decay when the dephased vectors are along $\mathbf{e}_3$, according to Eq. (5). Keeping the time separation of the first two pulses constant, one can measure the population decay time T_1 by monitoring the stimulated echo signal as a function of the delay time between the second and the third pulses, τ_{23}. The direction of the infrared radiation is determined by

$$k_{x,\,echo} = k_{3x} + k_{2x} - k_{1x}. \tag{20}$$

Compared to the direct pump-and-probe experiments which we discussed earlier, the stimulated photon echo signals decay to zero with a rate directly equal to that of the population relaxation. This can be significant for relatively weak optical pumping. In

those cases, the contribution from the ground-state molecules can overwhelm that from the molecules in excited states.

So far, we have discussed the coherent infrared excitation schemes which can, in principle, be used to create population changes and phase coherence in a monolayer of vibrationally excited adsorbates or other vibrational resonances on a surface. These vibrational excitations can be probed either by detecting the coherent infrared reemission from the surface layer in forms of photon echoes or by *in situ* optical wave-mixing technique, both of which we will discuss in Section C. Next, we evaluate the strengths of the coherently reemitted infrared signals and the related practical considerations.

4. *Coherent infrared reemission from a monolayer of vibrationally excited adsorbates*

With the rapid development of high power, ultrashort pulsed laser technology as well as nonlinear optical materials for frequency mixing in recent years, coherent laser sources in a number of infrared frequency ranges have been becoming available.[32, 33, 34, 30] In particular, free-electron lasers (FEL) have become the most promising infrared laser sources which can have a tuning range practically covering all infrared frequencies.[34] They can also deliver ultrashort pulses (10^{-12} s) and sufficient spectral brightness for optical pumping in the infrared frequency range. However, as FEL systems require substantially large initial set-up and large operating expenses, they are so far only available in a handful of laboratories. On the other hand, many table-top infrared lasers are increasingly attainable with the rapid progresses of ultrashort pulse laser technology. In addition, the development of nonlinear optical materials have expanded the frequency range of coherent infrared light sources through optical parametric processes or different frequency generation.[32, 33, 35] Many of these lasers already have sufficiently high power densities (up to GW/cm^2) and adequate pulse durations ($\leq 10^{-12}$ s) to be used to excite and probe

surface vibrations in real time.

We start with a monolayer of adsorbates with one of the vibrational resonances being coherently excited. The substrate can be an insulator or a metal or a semiconductor. To calculate the signal strength of the coherent reemission from the vibrationally excited adsorbate layer, we need to evaluate the induced surface polarization $\mathbf{P}(\omega_{IR}, t)$ which is related to the induced electric dipole moment $\mathbf{p}(\omega_{IR}, t)$ in Eq. (6) by

$$\mathbf{P}(\omega_{IR}, t) = N_s < \mathbf{p}(\omega_{IR}, t) >_{average}. \tag{21}$$

N_s is the density of the adsorbates. The ensemble average is performed over the distributions of the molecular orientation and the sites of adsorption. It is important to point out that $\mathbf{P}(\omega_{IR}, t)$ does not vanish when the adsorbate layer has inversion symmetry. In fact, this is true for all the even-wave mixing including linear optical processes (which are two-wave mixing processes). However, the result of the average in Eq. (21) depends on the polarization combination of the infrared pump beams and the substrate.[17] On a metal surface, for example, if the infrared pump beams are parallel polarized, the resultant electric fields for optical pumping at the surface seen by adsorbates are essentially along the surface normal **n**. In this case, we expect

$$< p_x(\omega_{IR}, t) >_{average} = 0 , \tag{22}$$

$$< p_y(\omega_{IR}, t) >_{average} = 0 , \tag{23}$$

$$\mathbf{P}(\omega_{IR}, t) = N_s < p_z(\omega_{IR}, t) >_{average} \mathbf{n} . \tag{24}$$

x, y and z are coordinates in the laboratory frame. x and y axes are chosen in the plane of

the surface with x also in the plane of incidence. The positive z axis is chosen along the surface normal **n** which points outwards from the surface. If we define θ_m to be the angle made by the induced dipole moment $\mathbf{p}(\omega_{IR}, t)$ from the positive z-axis, using the result of Eq. (6), the surface infrared polarization is expressed

$$\mathbf{P}(\omega_{IR}, t) = P(\omega_{IR}, t)\,\mathbf{n} = N_s\,\mu_{ab}\,r_1(t) < \cos\theta_m >_{average}\,\mathbf{n}\,. \tag{25}$$

Normally, reemitted infrared radiation from the surface layer in reflection direction are detected. This is mostly determined by the fact that the infrared radiation in transmission direction can not propagate without substantial absorption in many substrates. By solving Maxwell equations at ω_{IR} with $\mathbf{P}(\omega_{IR}, t)$ as the source term, we can obtain the intensity or the energy of the infrared reemission from the adsorbate layer. With a source polarization $\mathbf{P}(\omega_{IR}, t)$ given by Eq. (26), it is easy to show that the electric field of the reemitted radiation in reflection direction is also parallel-polarized, and its amplitude is expressed as [35 - 37]

$$E^R(\omega_{IR}, t) = \frac{4\pi i\, k_o^R(\omega_{IR})}{\varepsilon^R k_z^T(\omega_{IR}) - \varepsilon^T k_z^R(\omega_{IR})}\,\frac{\varepsilon^T k_x^R(\omega_{IR})}{\varepsilon_a}\,P(\omega_{IR}, t)\,, \tag{26}$$

where superscripts R and T are indicative of the media of reflection and transmission, respectively. ε^T and ε^R are the dielectric constants of the media. ε_a is the dielectric constant of the adsorbate layer. k_0 is the magnitude of the wave vector. From Eq. (26), we can calculate the total radiated energy from the vibrationally excited adsorbate layer

$$S(\omega_{IR}) = \frac{c}{8\pi}\,A\int_{-\infty}^{+\infty} |E^R(\omega_{IR}, t)|^2\,dt\,. \tag{27}$$

A is the beam cross-section of the reemitted infrared signal. If we denote the peak of the electric field as $E_{max}(\omega_{IR})$, the total radiated signal can be written as

$$S(\omega_{IR}) \sim \frac{c}{8\pi} \left| E_{max}(\omega_{IR}) \right|^2 A\,T. \tag{28}$$

T is the apparent decay time of the coherent radiation. It is determined by the overall spectral linewidth which is contributed by both the inhomogeneous broadening and the homogeneous linewidth Γ. To understand the physical constituents contained in the total radiation energy given by Eq.(27) or (28), we can rewrite Eq. (28) using the result of Eq. (26)

$$S(\omega_{IR}) \sim \left\{ \frac{\omega_{IR}^4}{8\pi c^3} \left[P_{max}(\omega_{IR},t)\, A \frac{k_0^R}{k_z^R} \right]^2 \left(\frac{k_x^R}{k_0^R} \right)^2 \right\} \times \left(\frac{\lambda_{IR}^2}{A} \right) \times T \times \left| \frac{2\,k_z^R}{\varepsilon^R k_z^T - \varepsilon^T k_z^R} \times \frac{\varepsilon^T}{\varepsilon_a} \right|^2 . \tag{29}$$

According to Ref. 17 and Ref. 38, we recognize that the first term is the radiation rate, $dS(\omega_{IR})/(dt\, d\Omega)$, of a joint dipole into a unit solid angle in the reflection direction determined by the phase-matching condition, $k_x^R = 2k_{2x} - k_{1x}$. The amplitude of the joint dipole is the sum of the rephased dipole moments of the vibrationally excited adsorbates. The second term is the solid angle $\Delta\Omega = (\lambda_{IR})^2/A$ within which the reemitted radiation from the excited adsorbate layer is confined.[17, 38] T is the overall decay time of coherence which determines the temporal width of the reemitted coherent radiation. The last term is the efficiency factor of the macroscopic electromagnetic radiation, often known as Fresnel factor.

From the viewpoint of the experiment, one would like to have as large a joint dipole moment as possible in order to optimize the signal strengths. Given the total number of the

excited adsorbates, this can be achieved by making pulse angles, θ_{p1} and θ_{p2}, close to unity from the results of Eqs. (29) and (18). We can estimate the single-pulse fluence (joules / cm^2) of a pump beam required to induce unity pulse angles. If we can take a typical pump pulse duration $\tau_p = 5 \times 10^{-12}$ s, a typical dynamic dipole moment for a molecular vibration $\mu_{ab} = 0.04 \times$ electron charge $\times$ Bohr radius $\sim 10^{-19}$ esu, from the requirement that

$$\theta_p \sim \frac{2\pi \mu_{ab} E^{I}_{ab}(\omega_{IR}) \tau_p}{h} \sim 1 , \tag{30}$$

we find that one would need a single-pulse fluence close to

$$\int_{-\infty}^{+\infty} I(\omega_{IR}, t)\, dt \sim \frac{c}{8\pi}\left[E^{I}_{ab}(\omega_{IR})\right]^2 \tau_p \sim \frac{c\, h^2}{8\pi \mu_{ab}^2 (2\pi)^2 \tau_p} \sim 3 \times 10^4 \text{ esu} \sim 3 \text{ mJ / cm}^2 . \tag{31}$$

This corresponds to power densities close to one GW/cm^2. Currently, there are a number of pulsed lasers operating in the infrared ranges which can provide the required single pulse fluences.[32 - 34] Besides the Free-electron lasers, the most commonly used table-top picosecond coherent infrared beams are generated in an optical parametric oscillation (OPO) and amplification (OPA) process with a pair of $LiNbO_3$ crystals. The generated infrared pulses have a tuning range from 2.8 μm to 4.4 μm, single pulse energies of a few hundreds of micro-joules and temporal widths which are presently limited by that of the parent pulses at 1.0 μm. By using other nonlinear crystals, it is possible to extend the infrared tuning range to 12 μm.[39] Recently, Mourou et al. have succeeded in generating table-top subpicosecond laser pulses at 1.053 μm with single-pulse energy close to one joules by using optical frequency chirping and prism compression techniques.[40] It should

be possible to use these types of lasers to generate subpicosecond tunable infrared beams with single-pulse energy in the range of milli-joules.

As laser power densities of MW/cm^2 to GW/cm^2 are close to or over the thresholds of optical damage for many materials, the achievable pulse angles can be limited practically by optical damage. Most of metals are highly reflective at infrared frequencies. If the laser-induced damage is due to melting or other mechanisms which have sharp on-sets with the surface temperature, the lowest on-set determines the maximum allowed temperature rise which in turn determines the threshold energy density ($joules/cm^3$). As the optical absorption depths at infrared frequencies in metals are short compared to the thermal diffusion lengths even for picosecond pulses, the laser-heated volumes are proportional to the thermal diffusion lengths, $\sim (\kappa \tau_p)^{1/2}$. In these cases, the maximum allowed pump power densities (in unit of J/cm^2 sec) are inversely proportional to the square roots of pump laser pulse durations, τ_p, and the maximum achievable pulse angles vary with τ_p as [see, Eq. (17)]

$$\theta_{p,\,max} \propto (\text{ Threshold laser energy density }) \times \tau_p^{\frac{3}{4}} \ . \tag{32}$$

If the optical field breakdown is the dominant mechanism for the laser-induced damage, the maximum allowed electric field of a pump laser beam is then limited by the threshold field for the optical breakdown, and we should expect

$$\theta_{p,\,max} \propto \tau_p \ . \tag{33}$$

Threshold energy densities for thermally induced optical damages of metals may be estimated from the material constants such as the melting points and other thermal and

optical constants of the materials. They are generally on the order of GW/cm^2 for picosecond pulses.

Many of semiconductors are transparent to near infrared radiation even though $\varepsilon^T(\omega_{IR}) >> 1$. The maximum pulse angles for these materials are only limited by the thresholds for optical field breakdowns, which are normally very high. Most of insulators are also transparent to near infrared radiation. Therefore, within the limits of optical damage, pump laser power densities as high as GW/cm^2 (which are usually required for inducing large pulse angles) should be applicable to surfaces of most of insulators and semiconductors, and even to surfaces of many metals.

We can now put in typical numerical parameters for an estimate of the signal strength of the coherent infrared reemission from an excited adsorbate layer. Although one must examine the validity in each individual case, we will assume that the pulse angles can be made close to unity. Consider, for example, the reemission of a two-pulse photon echo described by Eq. (18). If we take the following as the representatives of experimentally achievable parameters,

$$\begin{aligned}
&\sin^2(\theta_{p1}) = 1 , \\
&\sin^4(\theta_{p2}/2) = 1 , \\
&A = 1\ mm^2 = 0.01\ cm^2 , \\
&N_s = 4 \times 10^{14}\ /cm^2 , \\
&\lambda_{IR} = 2\pi\, c / \omega_{IR} = 3\ \mu m = 3 \times 10^{-4}\ cm , \\
&\mu_{ab} = 10^{-19}\ esu , \\
&T = 10^{-12}\ s ,
\end{aligned} \tag{34}$$

we find that from Eq. (29),

the radiation rate of the joint dipole per unit solid angle $\sim 3.3 \times 10^{7}$ joules/s.sr,

the solid angle of the coherent radiation $\Delta\Omega \sim 9 \times 10^{-6}$ sr ,

overall coherent radiation time $T \sim 10^{-12}$ s ,

Fresnel factor ≥ 1 (35)

Hence, a typical energy of a two-pulse induced infrared photon echo reemitted from a monolayer of vibrationally excited adsorbates is

$$S(\omega_{IR}) \sim 3 \times 10^{-11} \text{ joules / pulse} \sim 5 \times 10^{8} \text{ photons / pulse} . \qquad (36)$$

Similar calculations can be performed for other cases discussed in section B.

As we have already stated at the beginning, the detection of the rephased coherent vibrational excitations in real time is expectedly more difficult due to exceedingly small number of adsorbates involved in the interaction with the radiation fields (small joint dipole) and very rapid nonradiative relaxation at surfaces (short coherent radiation time, $T = 1/\Gamma$). Next, we will discuss a number of possible optical detection schemes which may be used to detect these weak excitations or the reemitted infrared radiation signals from the adsorbate layer given in Eq. (36).

C. Detection of Coherent Surface Vibrational Excitations

The technology for detection of radiation in the infrared especially near infrared frequency range has advanced rapidly with the development of semiconductor materials over the past two decades.[42] Sensitive near-infrared detection schemes have been reported

or at least tested in a number of research laboratories. So far, as we have discussed in the previous chapter, only optical SFG has been quantitatively demonstrated to be capable of detecting transient vibrational excitations at well-defined surfaces. In this section, we discuss and compare three techniques for detection of transient surface vibrational excitations and examine their efficiencies and practical concerns in an experimental implementation. These detection schemes are, a) a direct measurement of the reemitted infrared photon echoes from surface vibrational excitations using highly sensitive infrared detectors; b) up-conversion of the infrared photon echoes into signals in visible range in a nonlinear crystal with a ultrahigh time resolution and a high detection quantum efficiency; c) *in situ* up-conversion of the coherent vibrational excitations with the surface infrared-visible sum-frequency generation.

1. *Direct measurement of the reemitted surface infrared photon echoes*

Presently, there are a number of commercially available infrared detectors such as liquid-nitrogen-cooled HgCdTe detectors or liquid-helium-cooled Si:Sb detectors which are highly sensitive.[42] Their noise equivalent powers are of the order of 10^{-11} to 10^{-16} Watt $(Hz)^{-1/2}$. Their response times, τ_r, are usually long, in the range of 10^{-4} s. As most of the high power infrared lasers suitable for exciting surface vibrational transients typically operate at low repetition rates from 1 to 10^3 Hz, one usually uses the AC-coupled Box-car gated integration technique for detection. The optimum gate width for a single pulse should be close to the response times of the detectors τ_r. With a collection efficiency of $\gamma = 5\%$ and an energy of a reemitted photon echo given by Eq. (36), $S(\omega_{IR}) \sim 3 \times 10^{-11}$ joules/pulse, we expect the signal power averaged over one gate to be

$$W(\omega_{IR}) = \frac{S(\omega_{IR})\,\gamma}{\tau_r} \approx 10^{-8}\ \text{Watts}\,. \tag{37}$$

As the detection bandwidth, Δf, is equal to $1/\tau_r = 10^4$ Hz, from the noise-equivalent-powers of the detectors, we can estimate the noise equivalent energy to be 10^{-13} to 10^{-18} joules or the noise-equivalent-power to be 10^{-9} to 10^{-14} Watts, after averaging over one integration gate. By averaging over a reasonably large number of pulses, the detector noises can be brought well below the signal levels as the noise power decreases inversely with the square root of the number of pulses. However, other noise sources such as thermal noise in output coupling resistors and in the Box-car electronics may increase the number of pulses needed for sufficient signal-to-noise ratios. By cooling both detectors and load resistors (10^9 to 10^{10} Ohms) to liquid helium temperatures, and preamplifier to 90 Kelvins, it has been demonstrated experimentally that the noises in load resistors and preamplifiers can be reduced to a few hundred micro-volts with detection bandwidths $\Delta f = 10^4$ Hz.[42] Using Si:Sb detectors with a load resistor of 10^9 Ohms, for an input signal power of 10^{-8} Watts, the signal voltages at the output of preamplifier before box-car gated integration can be as large as a few volts. Therefore, one should be able to detect the reemitted infrared photon echoes from an adsorbate monolayer with a signal-to-noise ratio only limited by shot-to-shot fluctuations. Proper thermal shield may be necessary to reduce the background from the black-body radiation.

Despite of the adequate detection efficiencies and low noise figures, the detection time window ($\geq 10^{-4}$ sec) is overwhelmingly large compared to the durations of the infrared signals which are typically of 10^{-12} sec. Therefore this method can not timely discriminate against the diffusive scattering from the strong pump beams which precede the signals. This is the most serious drawback of this technique. From Eq. (31), a typical single-pulse energy of a pump beam is in the range of a few hundred micro-joules over a beam cross

section of a few square millimeters, corresponding to 10^{15} to 10^{16} photons. One might consider spatially separating the pumping pulses from the signal by properly choosing the optical arrangement for excitation . However, it is known that surfaces of most substrates always have some degree of roughness at the scale of optical wavelengths. Typically, the diffuse scattering of the pump pulses are almost isotropic from these surfaces. The strengths of these diffusively scattered radiation within the same detection solid angle for the photon echo signals are typically over 10^{-7} times as strong as those of the specularly reflected beams. This means that one should still expect 10^{8} to 10^{9} photons from the preceding pump pulses being scattered into the detector within the same time gate. The real signals are at most of 10^{8} to 10^{9} photons and easily drop down to 10^{6} to 10^{7} photons or less in typical time-resolved relaxation measurements. As the diffusive scattering is at the same frequency, one can not use spectral discrimination methods. Therefore, the slow response times of these highly sensitive infrared detectors prevent this technique from effectively suppressing the large background from the pump pulses in real time. For surfaces of semiconductors, one may achieve better surface smoothness. Even in these cases, one must exert extreme care to properly terminate the scattered and reflected pump pulses from other parts of the entire experimental system. It may be possible to subtract the large diffusive scattering background. The effectiveness of such a subtraction can be largely limited by the pulse-to-pulse fluctuations of the infrared laser sources which are typically 5% to 10% presently.

Apparently, it is much more desirable to use detection schemes which can make measurements selectively in time so that the interference from the diffusive scattering of the pump pulses can be effectively discriminated against. So long as the detection efficiencies do not suffer gravely, they should enable us to observe the photon echo signals with high signal-to-background ratios . Next, we will discuss two of such kind of optically gated detection schemes by using optical three-wave mixing or up-conversion techniques. They

are also known as optical sum-frequency generation processes, part of which has been discussed in the last chapter.

2. *Optical up-conversion of the reemitted surface infrared photon echoes in a nonlinear optical crystal*

Optical sum-frequency generation and difference-frequency generation processes in nonlinear optical media have been used to detect and characterize optical signals with high time resolutions.[21 - 24] Typically, an optical signal to be detected is overlapped with a strong laser pulse both spatially and timely in a nonlinear optical medium. The output at the sum frequency (usually in the visible range) is monitored. Due to the electronic nature of optical wave mixing processes in nonlinear optical media, the response times in these media are expected to be less than 10^{-14} seconds. As a result, the sum-frequency output is generated only when the up-converting pulse coincides with the signal. Thus an up-conversion process can be used as an optical gated detection method with a time-resolution only limited by the temporal duration of the converting puls, the latter now can be as short as a fraction of a picosecond. Furthermore, an up-conversion of an optical signal can be as efficient as a few percent.[21] With a typical detection quantum efficiency of 1% in visible range, this technique can be most promising.

In principle, we should be able to use this technique to resolve the surface infrared radiation signals from the preceding diffusive scattering. The scattered infrared radiation of the pump pulses may be effectively reduced or even eliminated so long as the up-conversion is performed long enough after the arrivals of the pump pulses. We now discuss a few important aspects of the technique and practical considerations for experimental implementation. Following the notation of Hartmann and Laubereau, when an infrared signal at ω_1 overlaps with a visible laser pulse at ω_2 in a nonlinear crystal, the

sum-frequency output at $\omega_3 = \omega_1 + \omega_2$ resulting from the nonlinear three-wave mixing process under the phase-match condition is given by [21]

$$N_{signal}(\omega_3) = \frac{128\,\pi^2\,\omega_3\,\omega_1}{c^3\sqrt{\varepsilon(\omega_3)\,\varepsilon(\omega_2)\,\varepsilon(\omega_1)}}\,d_{eff}^2(\omega_3 = \omega_1 + \omega_2)\,l_{eff}^2\,I(\omega_2)\,N_{signal}(\omega_1)\,. \tag{38}$$

$N_{signal}(\omega_3)$ is the number of the sum-frequency photons. $N_{signal}(\omega_1)$ is the photon number of the infrared signal which overlaps with the up-converting visible pulse. $d_{eff}(\omega_3)$ is the effective second-order nonlinear optical coefficient. l_{eff} is the effective interaction length of the signal beam and the up-converting beam whose the intensity is $I(\omega_2)$. The up-conversion efficiency can then be defined as

$$\eta = \frac{N_{signal}(\omega_3)}{N_{signal}(\omega_1)} = \frac{128\,\pi^2\,\omega_3\,\omega_1}{c^3\sqrt{\varepsilon(\omega_3)\,\varepsilon(\omega_2)\,\varepsilon(\omega_1)}}\,d_{eff}^2(\omega_3 = \omega_1 + \omega_2)\,l_{eff}^2\,I(\omega_2)\,. \tag{39}$$

Using a nonlinear crystal $LiNbO_3$ with $d_{eff} = 2.1 \times 10^{-8}$ esu and a typical crystal length $l_{eff} = 2$ mm, an pump beam intensity $I(\omega_2) = 30$ MW/cm^2 at 1.064 μm is sufficient to convert a weak infrared signal at wavelength $\lambda = 3.4$ μm into a visible signal with an efficiency as high as 10% before detection.[43, 21] For a up-converting pulse with $\tau_p = 15$ picoseconds and a beam area $A = 0.01$ cm^2, only a few micro-joules in a single pulse is required to achieve such a pumping intensity. This requirement is relatively modest nowadays.[32, 33, 34] The high conversion efficiencies from infrared signals to visible signals (a few percent or higher) achievable with currently available short-pulse visible lasers are rather encouraging, as we anticipate the infrared signal strengths from a monolayer of adsorbates in the range of 10^8 photons per pulse.

Before we can determine the overall efficiency of the method, it is important to

discuss a number of practical aspects which may crucially affect the up-conversion. First of all, from Eq. (39), we notice that the up-conversion efficiency η is proportional to the square of the effective interaction length l_{eff}. It can be limited by a number of factors under phase-matching condition, especially in the limit of ultrashort pulses. We first assume that both the infrared signal beam and the visible up-converting beam propagate collinearly in the crystal. Since the group velocities for the two beams are different, the interaction time between the two beams is limited by the time over which they become apart by the mean of their pulse durations. Therefore the product of the difference of their group velocities and the mean value of their pulse durations sets an *upper limit* for the effective interaction length l_{eff}. This can become most important for picosecond and especially subpicosecond pulses. It is easy to find that the upper limit of the effective interaction length due to group velocity dispersion is given as

$$l_{g.v.} = \frac{c\,\tau_p}{\sqrt{\varepsilon(\omega_2)}\left[\sqrt{\varepsilon(\omega_2)} - \sqrt{\varepsilon(\omega_1)}\right]} \,. \tag{40}$$

For $LiNbO_3$ crystal, if we choose $\omega_1 = 2\pi c/\lambda_1$ with $\lambda_1 = 3.3\ \mu m$, and $\omega_2 = 2\pi c/\lambda_2$ with $\lambda_2 = 0.532\ \mu m$,

$$\sqrt{\varepsilon(\omega_2)} \approx 2.0 \,, \tag{41}$$

$$\sqrt{\varepsilon(\omega_1)} \approx 1.83 \,,$$

assuming that both the signal and the pump pulse have the same duration, $\tau_p = 1\times 10^{-12}$ s, we would arrive at $l_{g.v.} \approx 0.9$ mm. This is already a factor of two shorter than the value (2 mm) which we quoted from Ref. 21

Another limiting factor on the effective interaction length is the phase-matching bandwidth. Typically, spectral bandwidths of picosecond or subpicosecond optical pulses are of a few wavenumbers or a few tens of wavenumbers, even for Fourier transform-limited pulses from mode-lock lasers. The phase-matching along the direction of propagation is only perfect for a fraction of the overall frequency composition of the two mixing pulses, the rest of the Fourier frequency components will experience imperfect phase-matching. This leads to an effective reduction of the up-conversion efficiency. It is known that the effective phase-match bandwidth is inversely proportional to the crystal length.[21] For a signal bandwidth of 10 to 30 cm^{-1} which is typical for a picosecond or subpicosecond infrared signal pulse, using the analysis of Ref. 21, we find that the length of a $LiNbO_3$ crystal for up-conversion should not be longer than a few millimeters.

In some cases, up-converting beams may have to be focused in the nonlinear crystal in order to achieve the desired pump intensity levels. Infrared signal beams may also come into the nonlinear crystal with some degree of divergence or convergence. It is well-known that for a given pair of infrared and visible frequencies, the phase matching is only perfect along one direction. The large angular spreads of the pump beam wave vector and the signal beam wave vector can lead to imperfect phase matching and therefore to less efficient conversion. The tolerable angular spread of the wave vectors of the two beams, $\delta\Omega$, varies with the crystal length l as $l^{-3/2}$.[21] In an example given in Ref. 21, from the calculation for a 2 mm-long $LiNbO_3$ crystal, Laubereau et al. found that, to maintain an nearly constant phase-matching condition over a bandwidth of 10 to 30 cm^{-1}, one either has to restrict the beam divergence $\leq 10^{-3}$ sr, or to reduce the length of the nonlinear crystal further down to a fraction of a millimeter.

Another concerning factor has to do with the detection of the generated sum-frequency signal. As it is accompanied by the strong visible up-converting beam, the spectral screening in the collinear geometry which we have assumed so far is often not

sufficient. In these cases, one must use noncollinear (off-axis) up-conversion geometry in which the infrared signal beam and the visible pump beam are brought to the nonlinear crystal at different angles. This will further reduce the effective interaction length and the tolerable angular spreads of the two mixing beams.[21]

Generally speaking, if one uses a $LiNbO_3$ crystal to convert picosecond infrared signals, the crystal length should be in the range of a millimeter or less. To compensate for the reduced crystal length and maintain an up-conversion efficiency of a few percent or even higher, one has to use visible pump laser beams with intensities close to GW/cm^2. Other types of nonlinear optical crystals can also be used. The nonlinear optical coefficients of these materials are generally comparable to that of $LiNbO_3$.[39] Besides the optical nonlinearity, the selection of a nonlinear crystal depends also on the frequency range of the infrared signal and the resistance of the crystal to optical damages with pump beam intensities as high as a few GW/cm^2. At any rate, up-conversion efficiencies of 5% to 10% should be achievable under most circumstances.

With the strength of the infrared photon echo from the surface layer of 10^8 photons per pulse given in Eq. (36), 10% up-conversion efficiency, and 1% photon detection quantum efficiency at the sum-frequency, we should expect to observe 10^5 photon counts per pulse. With such high overall signal levels, it is possible to probe surface vibrational excitations which are more weakly pumped so that infrared lasers with lower peak intensities may be used. In some cases, this may be necessary either from the consideration of optical damage or improvement of shot-to-shot repeatability in order to increase the overall signal-to-noise ratio of the measurement. Furthermore, with such large signals and high efficiencies of photon counting detection techniques, one can achieve a dynamic range of detection of over 4 orders of magnitudes. This will enable one to even monitor free-induction decays of vibrational excitations on surfaces in real time and to detect photon-echo signals with $t \gg T_2$ so that the coherent diffusive scattering background

can be totally eliminated. The latter is derived from the fact that temporal profiles of pump pulses are usually of Gaussian type which has a trailing edge dropping much faster than the decay of homogeneously broadened excitations.

It is obvious that this technique is most promising for detections of weak infrared radiation from surfaces. It is much superior over the direct measurement in infrared as we discussed previously. We should expect this method to play an important and effective role in the studies of surface vibrational resonances and relaxation dynamics. Next, we discuss a different up-conversion scheme which is not as sensitive as the current one, but is attractive for its simpler experimental implementation.

3. *In situ up-conversion of the coherent vibrational excitations by surface visible-infrared sum-frequency generation*

In the last chapter, we discussed and demonstrated the working principle of using the *in-situ* infrared-visible sum-frequency generation to study vibrational excitations on a surface.[23, 24] We now examine the feasibility of using this technique to detect transient surface vibrational excitations such as photon-echoes or even free-induction decay.

There are a few technical advantages to use the *in situ* up-conversion technique over the previously described method. First of all, the conversion efficiency is not sensitively subject to the geometry with which the infrared pump beams and the visible up-converting beam are brought together on the surface. The wave vector of the coherent vibrational excitation $k_{x,\,echo}(\omega_{IR})$ is in the surface plane given by for examples, Eq. (14) or Eq. (20). The phase-match condition along the surface plane for the *in situ* infrared-visible sum-frequency generation, $k_{x,\,SFG} = k_{x,\,visible} + k_{x,\,echo}(\omega_{IR})$, is always satisfied as long as $|k_{x,echo}(\omega_{IR}) + k_{x,\,visible}| < k_{0,\,SFG}$ in the medium of reflection. In these cases, the phase-matching condition is merely to determine the direction of radiation of the sum-frequency

output.[35] Since the coherent vibrational excitations are up-converted *in situ*, there is no group velocity mismatch problem. Furthermore, the spectral bandwidths and the wave vector spreads of the pump beams and the coherent vibrational excitations do not affect the efficiency of the up-conversion. For the same reason, spatial discrimination using off-axis geometry does not impose any restriction on the up-conversion efficiency either. As both spectral discrimination and spatial discrimination can now be used simultaneously to extract up-converted signals at sum-frequency in addition to the optical gating, the *in situ* up-converted sum-frequency signal is intrinsically background-free. Finally, the experimental implementation is generally simpler compared to the previous up-conversion scheme as the additional nonlinear optical wave mixing is not needed.

There are also a few potential disadvantages. Except for some of insulators which are optically transparent in visible frequency range, most of the substrates such as metals and semiconductors and many insulators are opaque to visible light. Optical damages due to strong absorption in these materials place stringent limits on the power densities of visible up-converting beam, $I(\omega_2)$. In contrast to the infrared radiation, the optical penetration depth of a visible light into a metal or a semiconductor is usually large compared to the thermal diffusion length which is less than 100 Å for a picosecond or subpicosecond pulse. If the material melting determines the optical damage threshold, the upper limit for the peak intensity of the visible up-converting pulse would vary inversely with the pulse duration,

$$I_{max}(\omega_2) = \frac{\text{constant}}{\tau_p} . \tag{42}$$

The constant may vary largely from substrate to substrate. If we use nickel single crystal as an example, for a 10 ns laser pulse at wavelength 0.532 μm with parallel-polarization and an incident angle of 45°, the damage threshold power density is found to be 24 MW / cm^2. By reducing the pulsewidth to 10^{-12} s, this threshold power density will rise up at

least over 2.4 GW /cm^2. Generally speaking, we expect the applicable intensities of visible pump beams to be in the range of a few hundred MW/cm^2 or higher for metal substates. They are comparable to the levels which one would need to up-convert infrared signals with an efficiency of a few percent in a 1 mm $LiNbO_3$ crystal. For semiconductors and insulators, the upper limits of applicable visible power densities are expected to be comparable. Hence depending on the specific system, optical damage may or may not pose as a major experimental problem.

The major setback of this method is the *effectively* short interaction length compared to an up-conversion in a nonlinear crystal. In an *in situ* optical sum-frequency generation, the *monolayer* of vibrationally excited molecules itself acts as the nonlinear medium for up-conversion, instead of a bulk nonlinear crystal of a millimeter thick. However, the conversion efficiency is partly compensated by the relatively large strength of the *effective* infrared signal as we will see shortly. Since there is no actual infrared signal in the form of radiation in an *in situ* up-conversion, we need to introduce an *effective* infrared radiation field in order to compare the present technique with the previous up-conversion scheme.

In the presence of a visible pump beam $\mathbf{E}(\omega_{vis})$, we can write down the nonlinear polarization at sum-frequency $\omega_3 = \omega_{vis} + \omega_{IR}$, using the notations of Shen and those in the earlier sections of this chapter and the last chapter,[37]

$$\mathbf{P}^{(2)}(\omega_3) = \frac{2\pi N_s}{h} \sum_s \left[\frac{(\mathbf{er})_{bs}\,(\mathbf{er}\cdot \mathbf{E}(\omega_{vis}))_{sa}}{\omega_3 - \omega_{sb} + i\,\Gamma_{sb}} - \frac{(\mathbf{er}\cdot \mathbf{E}(\omega_{vis}))_{bs}(\mathbf{er})_{sa}}{\omega_3 - \omega_{as} + i\,\Gamma_{as}} \right] r_1(\omega_{IR}, t)\,. \tag{43}$$

$r_1(\omega_{IR}, t)$ is defined by Eq. (6), corresponding to the ensemble average of the vibrational excitation of the adsorbates. It is important to note that unlike the polarization for the photon echo reemission given by Eq. (21), $\mathbf{P}^{(2)}(\omega_3)$ vanishes for an adsorbate layer with inversion symmetry, as the present up-conversion process is an odd wave mixing process

which, in the electric dipole approximation, is forbidden in such a medium. In most cases, we expect such an inversion symmetry is broken in the adsorbate layer as we have pointed out in the last chapter. The subscripts "a" and "b" denote the vibrational excited state and the ground state, respectively in the electronic ground state of the adsorbate. We have formally separated out the resonant contribution due to the vibrational excitation $r_1(\omega_{IR}, t)$ in Eq. (43). In the steady state, the corresponding surface susceptibility of the adsorbate monolayer [with $r_1 = 2\pi(\mathbf{er}\cdot\mathbf{E}(\omega_{IR}))_{ab} / h\Gamma_{ab}$] is given by

$$\chi^{(2)}_{ijk}(\omega_3) \sim \frac{2\pi N_s}{h} \sum_s \left[\frac{(er_i)_{bs}\,(er_j)_{sa}}{\omega_3 - \omega_{sb} + i\,\Gamma_{sb}} - \frac{(er_j)_{bs}\,(er_i)_{sa}}{\omega_3 - \omega_{as} + i\,\Gamma_{as}} \right] \times \frac{2\pi\,(er_k)_{ab}}{\Gamma_{ab}\,h} \,. \tag{44}$$

Here $(\mathbf{er})_{ab} = \mu_{ab} = \langle \psi_a | e\,\mathbf{r} | \psi_b \rangle$, as defined in Eq. (6). Formally, $\chi^{(2)}(\omega_3)$ given by Eq. (44) plays the same role in an *in situ* up-conversion as $d_{eff} \times l_{eff}$ in the up-conversion in a nonlinear crystal. We can write the total number of photons of the *in-situ* surface sum-frequency generation output in the same form as Eq. (38) [37]

$$N^{\text{in situ}}_{\text{signal}}(\omega_3) = \frac{128\,\pi^2\,\omega_3\,\omega_{IR}}{c^3} \left| \chi^{(2)}(\omega_3) \right|^2 I(\omega_{vis})\, N'_{\text{signal}}(\omega_{IR}) \,, \tag{45}$$

where the *effective* infrared radiation photon number, $N'_{\text{signal}}(\omega_{IR})$ is defined as

$$N'_{\text{signal}}(\omega_{IR}) = \frac{c}{8\pi} \left| \frac{h\,\Gamma_{ab}}{2\pi\,\mu_{ab}} \right|^2 \left| \text{Fresnel factor}\,(\omega_3) \right|^2 A\,T \left| \left[r_1(\omega_{IR}, t) \right]_{max} \right|^2 \left(\frac{2\pi}{h\,\omega_{IR}} \right).$$

or

$$S'_{signal}(\omega_{IR}) = \frac{c}{8\pi} \left| \frac{h\,\Gamma_{ab}}{2\pi\,\mu_{ab}} \times [r_1(\omega_{IR}, t)]_{max} \right|^2 \left| \text{Fresnel factor } (\omega_3) \right|^2 A\,T\,. \tag{46}$$

Here the duration of the visible up-converting pulse, $\tau_p(\omega_{vis})$, is assumed to be the same as the overall coherence relaxation time T. It is interesting to compare this result with the infrared radiation signal strength, $S(\omega_{IR})$, given by Eq. (28). If we neglect the minor difference of Fresnel factors at infrared and visible frequencies, $S'_{signal}(\omega_{IR})$ equals to the energy of an infrared pulse whose electric field strength is given by

$$E_{eff}(\omega_{IR}) = \frac{h\,\Gamma_{ab}}{2\pi\,\mu_{ab}}\,, \tag{47}$$

the latter corresponds to the electric field which would induce a pulse-angle of unity in a time duration $\Delta t = 1/\Gamma_{ab}$ in a pulsed infrared excitation or to the saturation electric field in a steady state excitation. If we assume that $T = 1/\Gamma_{ab}$, and use the same parameters listed in Eq. (34), the photon number of the *effective* infrared radiation is found to be,

$$N'_{signal}(\omega_{IR}) = 2 \times 10^{15} \text{ photons / pulse}\,. \tag{48}$$

Compared to $N_{signal}(\omega_{IR}) = 5 \times 10^{8}$ photons / pulse given in Eq. (36), the *effective* infrared signal to be *in situ* up-converted is 4×10^{6} times larger. We can now compare the overall up-conversion efficiency of the two up-conversion techniques by combining the results of Eq. (38) and (45)

$$\frac{N^{in\ situ}_{signal}(\omega_3)}{N_{signal}(\omega_3)} \sim \frac{|\chi^{(2)}(\omega_3)|^2}{[\,d_{eff} \cdot l_{eff}\,]^2} \times \frac{N'_{signal}(\omega_{IR})}{N_{signal}(\omega_{IR})}\,. \tag{49}$$

Using a typical value of molecular polarizabilities, $\alpha^{(2)}(\omega_3) = 10^{-29}$ esu,[44] surface molecular densities $N_s = 4 \times 10^{14}$ / cm^2, we obtain $\chi^{(2)}(\omega_3) = N_s\, \alpha^{(2)}(\omega_3) = 4 \times 10^{-15}$ esu. For $LiNbO_3$ crystal, $d_{eff} = 2 \times 10^{-8}$ esu, and if we use the effective interaction length $l_{eff} = 0.05$ cm, $d_{eff} \times l_{eff} = 1 \times 10^{-9}$ esu. This leads to

$$\frac{N^{in\ situ}_{signal}(\omega_3)}{N_{signal}(\omega_3)} \sim 10^{-5} \text{ to } 10^{-4} . \tag{50}$$

As $N_{signal}(\omega_3)$ is expected in the range of 10^7 photons per pulse, using the *in situ* up-conversion scheme, an overall sum-frequency signal strength is expected to be

$$N^{in\ situ}_{signal}(\omega_3) \sim 10^2 \text{ to } 10^3 \text{ photons / pulse} . \tag{51}$$

With a detection efficiency of 1%, we can expect a detected signal of a few photon counts per pulse. In some cases, within the limit of surface optical damages, one may be able to increase the power densities of the visible pump laser by a factor as high as 10 so that the overall signal may be improved by another factor of 10. Even with the estimate given by Eq. (51), the signal levels are still high enough for detecting transient surface vibrational excitations and the relaxation dynamics. Together with the inherent advantages, the method merits serious considerations as an alternative experimental approach.

D. Conclusion

We have shown that with available infrared and visible lasers and photon-detection

techniques, it is feasible to excite and probe transients of short-lived vibrational resonances of adsorbates on surfaces in real time. For detection of these vibrational transients, optical up-conversion schemes using the infrared-visible sum-frequency generation technique are highly effective for their intrinsic high time resolution which is only limited by the pulse duration of the visible pump beam, high conversion efficiency from infrared to visible, and high quantum efficiency of detection in visible frequency range. They are clearly superior over the experimental method using highly sensitive infrared detectors to directly detect the reemitted infrared photon echoes . These detectors have an inadequate time resolution (10^{-4} s) to discriminate against the interference of the large diffusive scattering from the preceding infrared pump pulses. The *In situ* sum-frequency generation technique, although not nearly as efficient as the up-conversion of the reemitted infrared photon echoes in a nonlinear crystal, can also be attractive for its simplicity in experimental implementation.

E. Appendix: local field corrections

For the convenience and continuity of the discussion, we have postponed the discussion of the effect of molecular local-fields on the efficiencies of optical pumping and radiation rrom surfaces at both infrared and visible frequencies.[38] The effect may be significant as the average distance between adsorbates at coverages close to a monolayer is almost the same as the spacings of atoms or molecules in condensed phase.[45] Furthermore, linear molecular polarizabilities are largely enhanced at the infrared frequencies which are tuned to the vibrational resonances during the optical pumping and reemission. It should not be surprising if one finds it necessary to correct the macroscopic field due to resonantly enhanced molecular fields.[38] In this appendix, we will explore this

issue in detail. As the macroscopic local field effect is already included in the calculation of reflection and transmission, we concentrate our discussion on the microscopic molecular local field effect.[46]

It is helpful to consider the effect on optical pumping and reemission processes separately. In optical pumping either with a near-resonant infrared laser beam or with a usually off-resonant visible beam, molecules on a surface see the local electric fields instead of the averaged macroscopic fields which are obtained from the usually calculation of reflection and transmission.[46, 47] With given incident pump laser beams, the efficiency of the optical excitation or optical pumping should then be subject to the local-field correction. As an example, consider molecular adsorbates on a metal surface. For a parallel polarized input laser beam, we only have to consider the z-component of the electric field $E_z(\omega)$. From Eq. (17), in order to determine the optical pumping efficiency, we need to determine the correction factor to $E_z(\omega)$ as the result of the microscopic molecular dipole fields from surrounding adsorbates.

Coherent reemission at infrared frequency from the rephased vibrational excitations or from the induced oscillating dipole layer at sum-frequency can be affected through the macroscopic dielectric constant $\varepsilon_a(\omega)$ of the adsorbate layer which appears explicitly in the radiation process [see, Eq. (26)]. It is known that $\varepsilon_a(\omega)$ is closely related to the dipole response of the adsorbate which should self-consistently include the local field correction.[45, 47]

Recently, these classical local-field corrections to the macroscopic electromagnetic fields in a monolayer adsorbates have been studied theoretically. They are mostly stimulated by the observation of abnormal features in surface optical absorption-reflectance measurements of adsorbates on metal surfaces.[45] Here, we use the results of Ref. 46 to analyze the size of such an effect on the generation and detection of surface vibrational photon echoes. For convenience, we also use a (100) surface of a single crystalline metal

as an example, which is assumed to have a lattice constant **a**. We also assume that at a monolayer coverage θ_s, each lattice site on the surface is occupied by a molecular adsorbate seating at a distance z_0 from the surface.[45] The lattice constant **a** is used here only as a measure of the average proximity or the density of the adsorbates. Due to the large dielectric constants of metals, the resultant electromagnetic field at the surface is mostly polarized along the surface normal. Therefore, we only need to consider the local field correction to the macroscopic field along z-axis. Following the notation of Ref. 45, if we define

$$\gamma_z(\omega) = \frac{\alpha_z^{(1)}(\omega)}{\mathbf{a}^3} , \tag{52}$$

with $\alpha^{(1)}(\omega)$ being the linear molecular polarizability, the local electric field $E_{z,\,local}(\omega)$ felt by an adsorbate is found equal to the macroscopic electric field $E_{z0}(\omega)$ in the absence of the adsorbate layer with a correction factor determined by the molecular dipole response of neighboring adsorbates and their images,[45]

$$E_{z,\,local}(\omega) = \frac{E_{z0}(\omega)}{1 - \gamma_z(\omega)\left(\xi_0 + \frac{\varepsilon^T - 1}{\varepsilon^T + 1}\,\xi_I\right)} . \tag{53}$$

ε^T is the dielectric of the substrate. Apart from $\gamma_z(\omega)$, ξ_0 results from the contributions of the adsorbate layer alone. After summing up the molecular fields from dipoles at all the lattice points on the surface except for the one under consideration, ξ_0 is found equal to −9.0336 for a square surface lattice. It is expected to be only slightly at variance for different two-dimensional lattices. ξ_I is contributed from the image dipole layer and is given as

$$\xi_I = 16\pi^2 \sum_{i,j=0}^{\infty} \sqrt{i^2+j^2}\, \exp\left(-\frac{4\pi z_0}{a} \sqrt{i^2+j^2} \right) . \tag{54}$$

From Eq. (54), as the adsorbed layer become sufficiently apart from the surface, z_0 becomes large compared to **a**, the contribution from the image dipole diminishes. At low adsorbate coverages, we can let **a** go to infinity. As ξ_I varies as a^2, an from Eq. (52), we find $E_{z,\,local}(\omega)$ approaches $E_{z0}(\omega)$ as we should expect for an isolated adsorbate on an open metal surface. According to Ref. 45, if one defines the volume density of molecular dipoles of the adsorbed layer as $\alpha^{(1)}(\omega)/a^2d$ where d ($\approx 2z_0$) is the effective thickness of the adsorbed layer, the z-component of the macroscopic dielectric constant of the adsorbate layer can be found through Maxwell equation as

$$\frac{1}{\varepsilon_{a,\,z}} = \frac{1-\gamma_z(\omega)\left(\frac{4\pi a}{d} + \xi_0 + \frac{\varepsilon^T-1}{\varepsilon^T+1}\xi_I \right)}{1-\gamma_z(\omega)\left(\xi_0 + \frac{\varepsilon^T-1}{\varepsilon^T+1}\xi_I \right)} . \tag{55}$$

To have an estimate of the local field correction to the results which we have discussed in the previous chapter, we assume a square lattice constant, **a**, equal to 5 Å which corresponds to a surface coverage of adsorbates, $N_s = 4 \times 10^{14}$ /cm^2, and take z_0 = 2Å. From Eq. (8-53), we obtain $\xi_I \approx 2.24$. We first examine the local field effect on the resonant optical pumping and reemission at infrared frequencies. As the resonantly enhanced part of the linear molecular polarizability is expected to be large compared to the nonresonant contribution, we can consider only the singly resonant term in $\alpha^{(1)}(\omega)$. If we choose a typical homogeneous spectral linewidth of the resonantly excited vibrational mode, $\Gamma_{ab} = 1 \times 10^{12}$ /sec (or 5 cm^{-1}) and a transition dipole moment $\mu_{ab} = 10^{-19}$ esu, we find that for both insulating substrates ($\varepsilon^T \geq 1$ to 2) and metal or semiconductor substrates

$(|\varepsilon^T| >> 1)$,

$$\gamma_z(\omega_{IR}) = \frac{2\pi\mu_{ab}^2}{h\Gamma_{ab}\mathbf{a}^3}(i) = 0.08\,i \tag{56}$$

$$E_{z,\,local}(\omega_{IR}) \approx E_{z0}(\omega_{IR}), \tag{57}$$

$$\left|\frac{1}{\varepsilon_{a,z}(\omega_{IR})}\right| \approx 1. \tag{58}$$

As we can see from Eq. (57), for most of adsorbate-substrate systems, local-field corrections at infrared frequencies to the macroscopic fields of the pump beams can be neglected. As the dielectric constants of the molecular monolayer $\varepsilon_{a,z}(\omega)$ are also in the range of unity, for all practical purposes, we can neglect their effects on the infrared radiation efficiencies.

As to the local field effects on the *in situ* sum-frequency generation and reemission processes, we can also offer a semi-quantitative analysis. We first note that the angular frequencies of the first allowed electronic transitions for many molecular adsorbates are in the ultraviolet range. As a consequence, the frequencies of neither up-converting beams nor the sum-frequency generation outputs are in resonance with the electronic resonances of the adsorbates in most cases. We can then estimate the nonresonant $\gamma_z(\omega)$ using bulk dielectric constants $\varepsilon(\omega)$ of the molecules in liquid or solid phase. The magnitudes of $\varepsilon(\omega)$ for most molecular liquids or solids in the visible frequency range values are close to 2. As the molecular densities n_m in liquid or solid phases are determined by their van der Waals radii, the volume occupied by each adsorbed molecule, $\mathbf{a}^2d$, should not be smaller than $1/n_m$. It is known that the molecular polarizability $\alpha^{(1)}(\omega)$ can be expressed in terms of the macroscopic dielectric constant in a condensed phase $\varepsilon(\omega)$,[47]

$$\alpha^{(1)}(\omega) = \frac{3}{4\pi n_m} \cdot \frac{\varepsilon(\omega) - 1}{\varepsilon(\omega) + 2} \ . \tag{59}$$

From Eq. (52) and the requirement that $n_m \geq (1/a^2 d)$, we find

$$\gamma_z(\omega_3) \approx \gamma_z(\omega_{vis}) = \frac{3}{4\pi} \cdot \frac{\varepsilon(\omega_{vis}) - 1}{\varepsilon(\omega_{vis}) + 2} \cdot \frac{1}{n_m a^3} \leq \frac{3}{4} \left(\frac{4\pi a}{d} \right)^{-1} , \tag{60}$$

and then we find

$$E_{z,\,local}(\omega_{vis}) \approx E_{z0}(\omega_{vis}) , \tag{61}$$

$$\frac{1}{\varepsilon_{a,\,z}(\omega_3)} \geq 0.4 \ , \text{ or } \ 1 \leq \varepsilon_{a,\,z}(\omega_3) \leq \varepsilon(\omega_3) \ . \tag{62}$$

The result of Eq. (60) is expected from the requirement $n_m \leq (a^2 d)^{-1}$. These results indicate that the efficiencies of optical pumping with visible laser beams and the *in situ* sum-frequency generation are not significantly affected by the local molecular field effect under most circumstances.

References:

1. G. A. Somorjai, Chemistry in Two Dimensions: Surfaces (Cornell University Press, Ithaca, NY, 1981), p.360.
2. M. A. Morris, M. Bowker, and D.A.King, Chemical Kinetics, ed. C. H. Bamford, Simple Processes at The Gas-Solid Interface, vol. 19, (Elsevier, 1984).
3. See, for example,*Vibrational Spectroscopy of Adsorbates*, edited by R. F. Willis, Springer Series in Chemical Physics, Vol. 15 (Springer, Berlin, 1980); *Surface Studies with Lasers*, edited by F. R. Auessenegg, A. Leitner, and M. E. Lippitsch. Springer Series in Chemical Physics, Vol. 33 (Springer, Berlin, 1983);
4. H. Ibach and D. L. Mills, *Electron energy Loss Spectroscopy and Surface Vibrations* (Academic, New York, 1982).
5. B. N. J. Persson and M. Persson, Solid State Commun. 36, 175 (1980);
   B. N. J. Persson and M. Persson, Surf. Sci. 97, 609 (1980);
   B. N. J. Persson and R. Ryberg, Phys. Rev. B 24, 6954 (1981);
   B. N. Persson and R. Ryberg, Phys. Rev. Lett. 48, 549 (1982);
   R. Ryberg, Surf. Sci. 114, 627 (1982);
   Hiromu Ueba and Shoji Ichimura, J. Phys. Soc. Japan 50, 3996 (1981);
   M. Persson, B. Hellsing, and B. I. Lundqvist, Journal of Electron Spectroscopy and Related phenomena, 29, 119 (1983);
   B. N. J. Persson and R. Ryberg, Phys. Rev. Lett. 54, 2119 (1985);
   B. N. J. Persson and R. Ryberg, Phys. Rev. B 32, 3586 (1985).
6. Y. J. Chabal, Phys. Rev. Lett. 55, 845 (1985);
   Y. J. Chabal, G. D. Higashi, and S. B. Christman, Phys. Rev. B 28, 4472 (1983);
7. J. C. Tully, Y. J. Chabal, Krishnan Raghavachari, J. M. Bowman, and R. R. Lucchese, Phys. Rev. B 31, 1184 (1984).

8. F. Träger, H. Coufal, and T. J. Chuang, Phys. Rev. Lett. 49, 1720 (1982).

9. T. J. Chuang, J. Electron Spectrosc. Relat. Phenom. 29, 125 (1983).

10. S. Chiang, R. G. Tobin, P. L. Richards, and P. A. Thiel, Phys. Rev. Lett. 52, 648 (1984).

11. J. P. Heritage and D. L. Allara, Chem. Phys. Lett. 74, 507 (1980).

12. E. J. Heilweil, M. P. Casassa. R. R. Cavanagh, and J. C. Stephenson, J. Vac. Sci. Technol. B 3(5), 1471 (1985);

M. P. Casassa, E. J. Heilweil, J. C. Stephenson, and R. R. Cavanagh, J. Vac. Sci. Technol. A 3(3), 1655 (1985);

E. J. Heilweil, M. P. Casassa, R. R. Cavanagh, and J. C. Stephenson, Chem. Phys. Lett. 117, 185 (1985);

E. J. Heilweil, M. P. Casassa, R. R. Cavanagh, J. C. Stephenson, J. Chem. Phys. 82, 5216 (1985).

13. J. W. Gadzuk and A. C. Luntz, Surf. Sci. 144, 429 (1984).

14. P. H. Berens and K. R. Wilson, J. Chem. Phys. 74, 4872 (1981);

D. W. Noid, M. L. Koszykowski, and R. A. Marcus, J. Chem. Phys. 67, 404 (1977).

15. J. E. Reutt-Robey, D. J. Doren, Y. J. Chabal, and S. B. Christman, Phys. Rev. Lett. 61, 2778 (1988).

16. H. Froitzheim, U. Kohler, and H. Lammering, Phys. Rev. B 34, 2125 (1986).

17. N. A. Kurnit, I. D. Abella, and S. R. Hartmann, Phys. Rev. Lett. 13, 567 (1964);

I. D. Abella, N. A. Kurnit, and S. R. Hartmann, Phys. Rev. 141, 391 (1966).

18. T. W. Mossberg, R. Kachru, S. R. Hartmann, and A. M. Flusberg, Phys. Rev. A 20, 1976 (1979);

T. Mossberg, A. Flusberg, R. Kuchru, and S. R. Hartmann, Phys. Rev. Lett. 42, 1665 (1979);

W. H. Heselink and D. A. Wiersma, Phys. Rev. Lett. 43, 1991 (1979);

S. Asaka, H. Nakatsuka, M. Fujiwara, and M. Matsuoka, Phys. Rev. A. 29, 2286 (1984);

P. C. Becker, R. L. Fork, C. H. Cruz, and C. V. Shank, Phys. Rev. Lett. 61, 1647 (1988).

19. P. Ye and Y. R. Shen, Phys. Rev. A 25, 2183 (1982);

T. K. Yee and T. K. Gustafson, Phys. Rev. A 18, 1597 (1978);

J. G. Fujimoto and T. K. Yee, IEEE J. Quant. Electron. QE-22, 1215 (1986);

K. Wynne, M. Müller, D. Brandt, and J. D. W. Van Voorst, Chem. Phys. 125, 211 (1988).

20. J. Fujimoto, J. Liu, E. Ippen, and N. Bloembergen, Phys. Rev. Lett. 53, 1837 (1984);

H. W. K. Tom, G. D. Aumiller, C. H. Brito-Cruz, Phys. Rev. Lett. 60, 1438 (1988);

C. V. Shank, R. Yen, and C. Hirlimann, Phys. Rev. Lett. 51, 900 (1983);

J. Kash and J. C. Tsang, Phys. Rev. Lett. 54, 2151 (1985).

21. D. A. Kleinman and G. D. Boyd, J. Appl. Phys. 40, 546 (1969);

H. J. Hartmann and A. Laubereau, Appl. Opt. 20, 4259 (81).

22. T. Daly and H. Mahr, Solid State Commun. 25, 323 (1978);

H. Mahr and M. D. Hirsch, Opt. Commun. 13, 96 (1975).

23. An initial attempt of such an experiment was reported by H. W. K. Tom, Ph. D. thesis, University of California, Berkeley, 1984 (unpublished);

X. D. Zhu, H.Suhr, and Y.R. Shen, Phys. Rev. B 35, 3047 (1987).

24. J. H. Hunt, P. Guyot-Sionnest, and Y. R. Shen, Chem. Phys. Lett. 133, 189 (1987);

P. Guyot-Sionnest, J. H. Hunt, and Y. R. Shen, Phys. Rev. Lett. 59, 1597 (1987);

P. Guyot-Sionnest, R. Superfine, and J. H. Hunt, Chem. Phys. Lett. 144, 1 (1988);

A. L. Harris, C. E. Chidsey, N. J. Levinos, and D. N. Loiacono, Chem. Phys. Lett. 141, 350 (1987).

25. In a typical optical experiment involving a bulk sample, the number of atoms or molecules which are involved in the interaction with optical radiation fields is at least in the range of 10^{17} to $10^{18}/cm^2$. In a typical surface experiment, this number is reduced to 10^{14} $/cm^2$. Since the efficiency of a coherent optical wave generation varies with the square of the total number of the optical scatters, we expect the efficiency of generate a photon echo on a surface to be lower by a factor of 10^6 to 10^8 than that in a bulk sample under same optical pumping conditions.
26. Unlike atoms in vapor phase with which many elegant photo echo experiments are performed, adsorbates interact with substrates strongly. As a result, they can dissipate their vibrational excitation energies nonradiatively and lose their coherent phases at much greater rates than their coherent radiative lifetimes (see for example, Ref. 38). Typical dephasing times T_2 on surfaces are in the range of 10^{-11} to 10^{-12} sec, while coherent radiative lifetimes of vibrational excitations of adsorbates at monolayer coverages($4 \times 10^{14}/cm^2$) are in the range of 10^{-8} sec to 10^{-9} sec. Therefore, for the same number of molecules and same level of coherent resonant excitation, the coherently radiated energy from molecules on a surface is expected 10^3 to 10^4 times less than that from the vapor phase molecules.
27. R. P. Feynman, F. L. Vernon, Jr., R. W. Hellwarth, J. Appl. Phys. 28, 49 (1957).
28. E. L. Hahn, Phys. Rev. 80, 580 (1950).
29. H. J. Eichler, P. Gunter, and D. W. Pohl, Laser-Induced Dynamic Gratings (Springer-Verlag, Berlin, Heidelberg, 1986).
30. A. L. Harris and N. J. Levinos, J. Chem. Phys. 90, 3878 (1989).
31. See, for example, Ref. 1.
32. A. Laubereau and W. Kaiser, Rev. Mod. Phys. 50, 607 (1978).

33. A. Seilmeier, K. Spanner, A. Laubereau, and W. Kaiser, Opt. Commun. 24, 237 (1978).

34. A. Gaupp, Free Electron Laser, CERN [Rep.], CERN 89-01, Proc, - CAS, CERN Accel. Sch. Adv. Accel. Phys. Course, 2nd, 207 (1987);
D. D. Dlott and M. D. Fayer, J. Opt. Soc. Am. B: *Opt. Phys.* 6, 977 (1989);
J. Ristein, B. Hooper, and P. C. Taylor, J. Opt. Soc. Am. B: *Opt. Phys.* 6, 1003 (1989);
N. J. Tro, D. A. Arthur, and S. M. George, J. Opt. Soc. Am. B: *Opt. Phys.* 6, 995 (1989);
W. S. Fann, S. Benson, J. M. J. Madey, S. Etemad, G. L. Baker, and F. Kajzar, Phys. Rev. Lett. 62, 1492 (1989).

35. N. Bloembergen and P. S. Pershan, Phys. Rev. 128, 606 (1962);

36. T. F. Heinz, Ph. D. thesis, University of California, Berkeley, 1982 (unpublished).

37. Y. R. Shen, *The Principles of Nonlinear Optics* (Wiley, New York, 1984), Chap. 25.

38. R. H. Dicke, Phys. Rev. 93, 99 (1954).

39. For $LiNbO_3$, see, for example, Ref. 21;
for $LiIO_3$, see, for example, L. S. Goldberg, Appl. Opt. 14, 653 (1975);
for $AgGaS_2$, see, for example, Y. X. Fan, R. C. Eckardt, R. L. Byer, R. K. Route, and R. S. Feigelson, Appl. Phys. Lett. 45, 313 (1984); T. Elsaesser, A. Seilmeier, W. Kaiser, P. Koidl, and G. Brandt, Appl. Phys. Lett. 44, 383 (1984);
for ADP, see, for example, F. Wondrazek, A. Seilmeier, and W. Kaiser, Appl. Phys. B 32, 1 (1983);
for AgGaSe2, see, for example, R. C. Eckardt, Y. X. Fan, R. L. Byer, C. L. Marquardt, M. E. Storm, and L. Esterowitz, Appl. Phys. Lett. 49, 608 (1986).

40. M. Pessot, P. Maine, and G. Mourou, Opt. Commun. 62, 419 (1987);
P. Maine and G. Mourou, Opt. Lett. 13, 467 (1988);

P. Maine, D. Strickland, P. Bado, M. Pessot, and G. Mourou, IEEE J. Quant. Electron. QE-24(2), 398 (1988).

41. J. H. Bechtel, J. Appl. Phys. 46, 1585 (1975).
42. S. Chiang, Ph. D. thesis, University of California, Berkeley, 1983 (unpublished) R. G. Tobin, Ph. D. thesis, University of California, Berkeley, 1985 (unpublished).
43. S. Singh, Non-linear Optical Materials, in Handbook of Lasers with Selected Data on Optical Technology, edited by R. J. Pressley (The Chemical Rubber Co., 1971), p. 489..
44. See, for example, Y. R. Shen, Ref. 9, Chaps 2 and 10. We use the following representative values: infrared dipole moment ~ 5×10^{-19} esu, Raman scattering cross section ~ 1×10^{-29} $sr^{-1}cm^{-1}$, and vibrational linewidth on a surface $\Gamma \sim 5$ cm^{-1}.
45. A. Bagchi, R. G. Barrera, and B. B. Dasgupta, Phys. Rev. Lett. 44, 1475 (1980); A. Bagchi, R. G. Barrera, and R. Fuchs, Phys. Rev. B 25, 7086 (1981).
46. See, for example, Ref. 36.
47. See, for example, J. D. Jackson, Classical Electrodynamics, 2nd edition (John Wiley & Sons, New York, 1975).

LAWRENCE BERKELEY LABORATORY
TECHNICAL INFORMATION DEPARTMENT
1 CYCLOTRON ROAD
BERKELEY, CALIFORNIA 94720